JOÃO PEDRO SENA

OPTIMAL-ROBUST DESIGN OF SMART STRUCTURES TO ENHANCE THE PERFORMANCES OF FATIGUE LIFE AND VIBRATION ENERGY HARVESTING

UNIVERSIDADE FEDERAL DE UBERLÂNDIA
FACULDADE DE ENGENHARIA MECÂNICA

2024

JOÃO PEDRO SENA

OPTIMAL-ROBUST DESIGN OF SMART STRUCTURES TO ENHANCE THE PERFORMANCES OF FATIGUE LIFE AND VIBRATION ENERGY HARVESTING

Tese apresentada ao Programa de Pós-graduação em Engenharia Mecânica da Universidade Federal de Uberlândia, como parte dos requisitos para a obtenção do título de **DOUTOR EM ENGENHARIA MECÂNICA**.

Área de Concentração: Mecânica dos Sólidos e Vibração.

Orientador: Prof. Dr. Antônio Marcos Gonçalves de Lima
Co-orientador: Prof. Dr. Noureddine Bouhaddi

UBERLÂNDIA - MG

2024

Ficha Catalográfica Online do Sistema de Bibliotecas da UFU
com dados informados pelo(a) próprio(a) autor(a).

S474 Sena, João Pedro, 1994-
2024 Optimal-robust design of smart structures to enhance the performances of fatigue life and vibration energy harvesting [recurso eletrônico] / João Pedro Sena. - 2024.

Orientador: Antônio Marcos Gonçalves de Lima.
Coorientador: Noureddine Bouhaddi.
Tese (Doutorado) - Universidade Federal de Uberlândia, Pós-graduação em Engenharia Mecânica.
Modo de acesso: Internet.
Disponível em: http://doi.org/10.14393/ufu.te.2024.540
Inclui bibliografia.

1. Engenharia mecânica. I. Lima, Antônio Marcos Gonçalves de,1975-, (Orient.). II. Bouhaddi, Noureddine, 1961-, (Coorient.). III. Universidade Federal de Uberlândia. Pós-graduação em Engenharia Mecânica. IV. Título.

CDU: 621

Bibliotecários responsáveis pela estrutura de acordo com o AACR2:

Gizele Cristine Nunes do Couto - CRB6/2091
Nelson Marcos Ferreira - CRB6/3074

UNIVERSIDADE FEDERAL DE UBERLÂNDIA
Coordenação do Programa de Pós-Graduação em Engenharia Mecânica
Av. João Naves de Ávila, nº 2121, Bloco 1M, Sala 212 - Bairro Santa Mônica, Uberlândia-MG, CEP 38400-902
Telefone: (34) 3239-4282 - www.posmecanicaufu.com.br - secposmec@mecanica.ufu.br

ATA DE DEFESA - PÓS-GRADUAÇÃO

Programa de Pós-Graduação em:	Engenharia Mecânica				
Defesa de:	Tese de Doutorado, nº 383, PPGEM				
Data:	19/07/2024	Hora de início:	09:00	Hora de encerramento:	12:20
Matrícula do Discente:	11923EMC013				
Nome do Discente:	João Pedro Sena				
Título do Trabalho:	Optimal-robust design of smart structures to enhance the performances of fatigue life and vibration energy harvesting				
Área de concentração:	Mecânica dos Sólidos e Vibrações				
Linha de pesquisa:	Dinâmica de Sistemas de Mecânica				
Projeto de Pesquisa de vinculação:	INCT-EIE				

Reuniu-se por videoconferência, a Banca Examinadora, designada pelo Colegiado do Programa de Pós-graduação em Engenharia Mecânica, assim composta: Prof. Dr. Roberto Mendes Finzi Neto - UFU; Prof. Dr. Rogério Sales Gonçalves - UFU; Prof. Dr. Edson Hideki Koroishi- UTFPR; Prof. Dr. Flavio Donizeti Marques - USP-São Carlos; Prof. Dr. Noureddine Bouhaddi-UBFC e Prof. Dr. Antônio Marcos Gonçalves de Lima - UFU, orientador do candidato.

Iniciando os trabalhos o presidente da mesa, Dr. Antônio Marcos Gonçalves de Lima, apresentou a Comissão Examinadora e o candidato, agradeceu a presença do público, e concedeu ao Discente a palavra para a exposição do seu trabalho. A duração da apresentação do Discente e o tempo de arguição e resposta foram conforme as normas do Programa.

A seguir o senhor presidente concedeu a palavra, pela ordem sucessivamente, aos examinadores, que passaram a arguir o candidato. Ultimada a arguição, que se desenvolveu dentro dos termos regimentais, a Banca, em sessão secreta, atribuiu o resultado final, considerando o candidato:

Aprovado.

Esta defesa faz parte dos requisitos necessários à obtenção do título de Doutor.

O competente diploma será expedido após cumprimento dos demais requisitos, conforme as normas do Programa, a legislação pertinente e a regulamentação interna da UFU.

Nada mais havendo a tratar foram encerrados os trabalhos. Foi lavrada a presente ata que após lida e achada conforme foi assinada pela Banca Examinadora.

Documento assinado eletronicamente por **Antonio Marcos Gonçalves de Lima**, **Professor(a) do Magistério Superior**, em 19/07/2024, às 12:28, conforme horário oficial de Brasília, com fundamento no art. 6º, § 1º, do Decreto nº 8.539, de 8 de outubro de 2015.

Documento assinado eletronicamente por **Roberto Mendes Finzi Neto**, **Professor(a) do Magistério Superior**, em 19/07/2024, às 12:29, conforme horário oficial de Brasília, com fundamento no art. 6º, § 1º, do Decreto nº 8.539, de 8 de outubro de 2015.

Documento assinado eletronicamente por **Rogerio Sales Gonçalves**, **Professor(a) do Magistério Superior**, em 19/07/2024, às 12:29, conforme horário oficial de Brasília, com fundamento no art. 6º, § 1º, do Decreto nº 8.539, de 8 de outubro de 2015.

Documento assinado eletronicamente por **Flávio Donizeti Marques**, **Usuário Externo**, em 22/07/2024, às 09:36, conforme horário oficial de Brasília, com fundamento no art. 6º, § 1º, do Decreto nº 8.539, de 8 de outubro de 2015.

Documento assinado eletronicamente por **Edson Hideki Koroishi**, **Usuário Externo**, em 22/07/2024, às 09:51, conforme horário oficial de Brasília, com fundamento no art. 6º, § 1º, do Decreto nº 8.539, de 8 de outubro de 2015.

Documento assinado eletronicamente por **Noureddine Bouhaddi**, **Usuário Externo**, em 30/07/2024, às 15:01, conforme horário oficial de Brasília, com fundamento no art. 6º, § 1º, do Decreto nº 8.539, de 8 de outubro de 2015.

A autenticidade deste documento pode ser conferida no site https://www.sei.ufu.br/sei/controlador_externo.php?acao=documento_conferir&id_orgao_acesso_externo=0, informando o código verificador **5531756** e o código CRC **D5EBFB76**.

Acknowledgements

I would like to express my sincere gratitude to everyone who contributed to the success of this work. First and foremost, I would like to thank my friends and colleagues who stood by my side throughout this academic journey. Your words of encouragement, support, and collaboration were invaluable and helped me overcome the challenges faced during my PhD.

To my beloved family, I express my profound gratitude for the constant love, support, and encouragement over the years. Your unwavering support has been a constant source of inspiration and motivation for me, and for that, I am eternally grateful.

To my dear wife, I express my deepest admiration and gratitude. Your love, patience, and understanding were fundamental in allowing me to dedicate myself fully to this work. Your words of encouragement and moral support were a true sustenance during the most challenging moments.

I thank God for granting me strength, wisdom, and guidance throughout this journey. His constant presence in my life has been the light that guided me through moments of uncertainty and difficulty.

To the Federal University of Uberlândia (UFU) and the LMEst Laboratory, I extend my gratitude for providing an environment conducive to the development of this work. The resources, facilities, and learning opportunities offered were crucial to the success of this research project.

To the University of Franche-Comté (FEMTO-ST), I express my gratitude for the opportunity to conduct part of this work in their facilities. The collaboration and exchange of knowledge with colleagues and professors were enriching and significantly contributed to the results achieved.

Finally, I would like to thank the Coordination for the Improvement of Higher Education Personnel (CAPES) for the financial support provided through a scholarship. This support was essential to enable my participation in this PhD program and the development of this work.

To everyone who in some way contributed to this journey, my most sincere thanks.

SENA, J. P. **Projeto ótimo-robusto de estruturas inteligentes para aumento de desempenho da vida em fadiga e *harvesting* de energia de vibração.** 2024. Tese de Doutorado, Universidade Federal de Uberlândia, Uberlândia.

Resumo

A análise de fadiga em estruturas submetidas a carregamentos aleatórios é mais eficiente no domínio da frequência devido ao menor custo computacional, levando em conta o ganho pela utilização de métodos como a base modal de Ritz e a metamodelagem com redes neurais. Dentre os métodos de controle de vibração, materiais inteligentes, especialmente os piezoelétricos, têm se destacado pela possibilidade de coleta de energia, graças à sua capacidade de funcionar como sensores e atuadores, além de serem leves e de fácil manuseio. A associação de circuitos *shunt* ao material PZT é realizada pela sintonização dos elementos do circuito, que requer um processo de otimização para obtenção dos parâmetros ótimos. Este trabalho propõe uma metodologia ótima-robusta para o projeto de sistemas dinâmicos que utilizam controle passivo visando reduzir a fadiga estrutural e aumentar a energia colhida. Foram analisados quatro casos principais: otimização do circuito com camada completa; otimização do circuito com tratamento parcial; otimização topológica por localização de *patches*; e otimização topológica por densidade de camada PZT. As técnicas de otimização empregadas, considerando incertezas nos parâmetros dos circuitos, mostraram-se eficazes na obtenção de melhores resultados em comparação aos métodos tradicionais.

Palavras-chave: Estruturas inteligentes, Harvesting, Fadiga, Circuito shunt, Otimização topológica

SENA, J. P. **Optimal-robust design of smart structures to enhance the performances of fatigue life and vibration energy harvesting.** 2024. PhD Thesis, Universidade Federal de Uberlândia, Uberlândia.

Abstract

Fatigue analysis in structures subjected to random loads is more efficient in the frequency domain due to lower computational cost, considering the gains from using methods such as the Ritz modal basis and neural network metamodeling. Among vibration control methods, smart materials, especially piezoelectrics, have stood out due to their energy harvesting capabilities, functioning as both sensors and actuators, and being lightweight and easy to handle. The association of shunt circuits with PZT material is achieved by tuning the circuit elements, which requires an optimization process to obtain the optimal parameters. This work proposes a robust-optimal methodology for designing dynamic systems using passive control to reduce structural fatigue and increase harvested energy. Four main cases were analyzed: full-layer circuit optimization; partial treatment circuit optimization; topological optimization by patch location; and topological optimization by PZT layer density. The optimization techniques employed, considering uncertainties in circuit parameters, proved effective in achieving better results compared to traditional methods.

Keywords: Smart structures, Harvesting, Fatigue, Shunt circuit, Topology optimization

List of Figures

List of Tables

Acronyms

CPU Central Processing Unit

VEH Vibration Energy Harvesting

PEMAP-P Piezoelectric Material with Penalty and Polarization

SIMP Solic Isotropic Material with Penalty

MMA Method of Moving Asymptotes

GA Genetic Algorithm

SLP Sequential Linear Programming

PZT Piezoelectric

CAPES Coordenação de Aperfeiçoamento de Pessoal de Nível Superior

FSDT First-order Shear Deformation Theory

FRF Frequency Response Function

DVA Dynamic Vibration Absorber

ODE Ordinary Differential Equation

NSGA Non-dominated Sorting Gnetic Algorithm

LHS Latin HyperCube Sampling

MROP Multi-objective Robust Optimization Problem

ANN Artificial Neural Network

CLT Classical Laminate Theory

PSD Power Spectral Density

ReLU Rectified Linear Unit

Symbols

$\boldsymbol{U}$ Displacement Field Vector

u, v, w Displacements

u_0, v_0, w_0 Translational degrees of freedom

$\psi_{\mathrm{x}}, \psi_{\mathrm{y}}$ Rotational degrees of freedom

$\boldsymbol{A}_{\mathrm{u}}, \boldsymbol{A}_0, \boldsymbol{A}_1, \bar{\boldsymbol{A}}^{(\bullet)}$ Relation matrices of displacements to the displacement field

$\boldsymbol{u}$ Vector of degrees of freedom

$\varepsilon_{\mathrm{xx}}, \varepsilon_{\mathrm{yy}}, \varepsilon_{\mathrm{zz}}$ Axial deformations

$\gamma_{\mathrm{yz}}, \gamma_{\mathrm{xz}}, \gamma_{\mathrm{xy}}$ Shear deformations

$\boldsymbol{\varepsilon}_{\mathrm{b}}$ Bending deformation vector

$\boldsymbol{\varepsilon}_{\mathrm{s}}$ Shear deformation vector

$\boldsymbol{D}_{\mathrm{b0}}, \boldsymbol{D}_{\mathrm{b1}}, \boldsymbol{D}_{\mathrm{s}}$ Derivation operator matrices

a, b Dimensions in natural coordinates

$\bar{a}, \bar{b}$ Dimensions in local coordinates

x, y Global axes

ξ, η Local axes

$\boldsymbol{J}$ Linear transformation Jacobian matrix

J Determinant value of the Jacobian

$N_{\bullet}$ Interpolation Functions

$\boldsymbol{N}$ Interpolation Matrix

$\boldsymbol{u}_{\mathrm{e}}$ Elementary displacement vector

$\boldsymbol{B}_{\mathrm{b0}}, \boldsymbol{B}_{\mathrm{b1}}$ Derivation matrices of bending interpolation

$\boldsymbol{B}_{\mathrm{s0}}$ Shear interpolation derivation matrices

E_{c} Kinetic energy

P_{e} Strain potential energy

ρ Material density

V_{e} Element volume

$\boldsymbol{M}$ Elementary mass matrix

$\boldsymbol{\sigma}$ Voltage vector

$\boldsymbol{\varepsilon}$ Strain vector

$\boldsymbol{C}$ Material Properties Matrix

$\boldsymbol{C}_{\mathrm{b}}$ Elementary bending property matrix

$\boldsymbol{C}_{\mathrm{s}}$ Elementary Shear Properties Matrix

$\boldsymbol{K}_{\mathrm{b}}$ Bending stiffness matrix

$\boldsymbol{K}_{\mathrm{s}}$ Shear stiffness matrix

$\boldsymbol{M}^{\mathrm{g}}$ Global mass matrix

$\boldsymbol{K}^{\mathrm{g}}$ Global stiffness matrix

$\boldsymbol{f}$ External loading vector

$\ddot{\boldsymbol{u}}$ Acceleration vector

L_d, L_u Cross-sectional interpolation functions

$\boldsymbol{\Phi}$ Electric potential vector

$\boldsymbol{N}_{\Phi}$ Matrix of electrical interpolation functions

$\boldsymbol{E}$ Electric field vector

$\boldsymbol{B}_{\Phi}$ Electrical interpolation derivation matrix

$\boldsymbol{D}$ Electrical displacement matrix

$\boldsymbol{e}_t$ Dielectric constant matrix

$\boldsymbol{\chi}_t$ Electrical permittivity matrix

$\boldsymbol{U}_{\mathrm{e}}$ Electrical strain energy matrix

$\boldsymbol{K}^e_{\mathrm{uu}}$ Elementary mechanical stiffness matrix

$\boldsymbol{K}^e_{\mathrm{u}\Phi}, \boldsymbol{K}^e_{\Phi\mathrm{u}}$ Elementary electromechanical stiffness matrices

$\boldsymbol{K}^e_{\Phi\Phi}$ Elementary Electrical Stiffness Matrix

$\boldsymbol{q}(t)$ Vector of global electrical charges

$\boldsymbol{u}_{\mathrm{r}}$ Reduced degrees of freedom vector

$\boldsymbol{T}$ Reduction base matrix

$\boldsymbol{N}_{\mathrm{m}}$ Truncated vibration mode matrix

$\boldsymbol{U}_{\mathrm{mod}}$ Nominal system modal response matrix

$\boldsymbol{U}_{\mathrm{s}}$ Enriched modal response matrix

$\boldsymbol{F}$ Unitary force matrix

$\boldsymbol{M}^{\mathrm{r}}_{\mathrm{uu}}, \boldsymbol{K}^{\mathrm{r}}_{\mathrm{uu}}, \boldsymbol{K}^{\mathrm{r}}_{\mathrm{u}\Phi}, \boldsymbol{K}^{\mathrm{r}}_{\Phi\mathrm{u}}$ Reduced version of elementary matrices

$\boldsymbol{C}_{\mathrm{eq}}$ Equivalent damping matrix

ω Frequency

$\boldsymbol{Q}$ Electric charge vector

q Electric charge

$\boldsymbol{H}_{\mathrm{u}}$ Mechanical Frequency Response Function Matrix

$\boldsymbol{H}_{\phi}$ Electrical Frequency Response Function Matrix

$R^{(\bullet)}_{\mathrm{opt}}$ Optimal Analytical Resistance

$L^{(\bullet)}_{\mathrm{opt}}$ Analytical Optimal Inductance

Z_{res} Resistor element impedance

Z_{ind} Inductor element impedance

Z_{R} Resistive circuit impedance

$Z^{(\bullet)}_{\mathrm{RL}}$ Resonant circuit impedance

P Power

V Voltage

I Current

$V_{\mathrm{R}}, V_{\mathrm{L}}$ Voltage of resistor and inductor elements

$\boldsymbol{\Upsilon}$ Power Frequency Response Function Matrix

$\boldsymbol{\phi}_f$ Power Spectral Density Matrix

R_f Autocorrelation function

$\boldsymbol{\phi}_u$ Spectral deformation matrix

R_u Displacement autocorrelation function

$\mathbb{E}\left[\bullet\right]$ Mathematical Expectation Operator

g Unit impulse response function

$\boldsymbol{G}$ Frequency Response Function

$\boldsymbol{\phi}_{\mathrm{s}}$ Spectral voltage matrix

$\lambda_{\bullet}$ Spectral moment m

T Period

N_{b} Number of passes through a level b

α_2 Bandwidth indication

N_{max} Number of maximums

N_f Fatigue life in cycles

S Stress range

$m_{f\bullet}$ Fatigue resistance exponent

$C_{f\bullet}$ Fatigue resistance coefficient

D Accumulated damage

T_f Fatigue analysis time

D_{sines} Sines accumulated damage

$J_{2,\text{a}}$ Second voltage invariant

α Voltage resistance coefficient

p_{h} Hydrostatic tension

$t\_{}_1, f\_{}_1$ Multiaxial fatigue resistance

S_{ut} Breaking limit voltage

$\boldsymbol{d}$ Voltage deviation tensioner

$\boldsymbol{D}_e$ Decomposition vector in Euclidean space

$D_\bullet$ Euclidean space coordinates

$R_\bullet$ Loading path axles

$\boldsymbol{P}_{\text{D}}$ Euclidean space variance

$\mathfrak{J}_{2,\text{a}}$ Second random stress invariant

$\mathfrak{R}_\bullet$ Random axles

μ Distribution mode

β Dispersion of the distribution

κ_u, κ_a Bandwidth Parameters

δ Function of irregularity factor

γ Euler-Mascheroni constant

ζ_3 Apery constant

$\boldsymbol{F}_{\text{o}}$ Objective function vector

$\boldsymbol{G}_{\text{c}}$ Constraints vector

$\mathcal{V}_{f_{\text{o}}}$ Vulnerability function

$\sigma_{f_{\text{o}}}$ Standard deviation of the objective function

$\mu_{f_{\text{o}}}$ Average of the objective function

$\boldsymbol{F}_{\text{o}}^{\text{R}}$ Vector of robust objective functions

f_{o} Objective function

Sp Entropy measure

p Probability distribution

X Random variable

Λ Lagrange multipliers

$\overline{R}$ Average resistance value

$\overline{L}$ Average impedance value

$\delta_{\mathrm{R}}, \delta_{\mathrm{L}}$ Finite dispersions of resistance and impedance

$p_{\mathrm{R}}, p_{\mathrm{L}}$ Resistance and impedance probabilities

Γ Gamma function

ϵ_m Mean error measure

$l_{\mathrm{x}}, l_{\mathrm{y}}, L_{\mathrm{x}}, L_{\mathrm{y}}$ Width and length of the structure

$h_{\mathrm{s}}, h_{\mathrm{p}}$ Structure and piezoelectric layer thickness

α, β Proportional damping coefficients

$\boldsymbol{S}$ Inverse of material properties matrix

E, G, ν Modulus of elasticity and poisson ratio

Y Admittance

YI Bending rigidity

m, M_{t} Mass per unit length and at the tip of the structure

$w_{\mathrm{rel}}, w_{\mathrm{b}}$ Relative displacement and at the tip of the structure

$c_{\mathrm{a}}, c_{\mathrm{s}}$ Viscous damping coefficient and strain rate

ϑ Inverse coupling coefficient

$C_{\tilde{\mathrm{p}}}^{\mathrm{eq}}$ Equivalent capacitance

$\tilde{\theta}$ Electromechanical Coupling Term

$\delta_{\mathrm{t}}, \delta_{\mathrm{l}}$ Percentage of piezoelectric layer thickness and length

$\boldsymbol{\Xi}$ Modal strain energy

dx, dy Patch Distance

ρ_e Piezoelectric element density

f_{V} Maximum coverage percentage

$\boldsymbol{\rho}_{\mathrm{PZT}}$ Coverage Density Vector

$\mathcal{C}_{\%}$ Coverage Percentage of the PZT layer

N_{PZT} Number of PZT elements

RE_{η} Relative Efficiency

Contents

Chapter I

Introduction

Fatigue analysis in structures subjected to random loads is more efficient when using the frequency domain, due to the computational cost efficiency involved (ROSA; LIMA, 2015). Additionally, multiaxial fatigue analyses are not trivial in the time domain, requiring consideration of some more widespread theories, such as those pointed out in the study by Weber (1999), which, combined with material properties, allow for the assessment of the structure's failure possibility (BORESI; CHONG; LEE, 2010; DOWLING, 2007).

Stochastic finite element fatigue analysis has a high computational cost, given that there are numerous evaluations of calculation routines through parameters obtained by a generator, such as the Latin Hypercube (FLORIAN, 1992) and evaluated by the Monte Carlo method (RUBINSTEIN, 1981). Therefore, there is a need to reduce the numerical model to perform the analyses more efficiently while maintaining the reliability of the results. One option to reduce uses the Ritz modal basis (LAMBERT; KHALIJ; PAGNACCO, 2007), which enables satisfactory computational gains for application in thin plate models (ROSA; LIMA, 2015). Other methods available in the literature can also be considered for robust reduction of stochastic models (GERGES, 2013).

In addition to the need for fatigue analysis in structures subjected to random loads, mitigating such vibration effects proves to be important, for instance, by using smart materials. The concept of smart structures or adaptive structures is also used in this work, as these structures can transform environmental energy into some type of action or adaptation to this new environment, aiming to maintain their predetermined perfor-

mance (FARIA, 2006). Static and/or dynamic disturbances applied to a structure can be addressed with the design of a smart structure. These structures can be implemented such that signals from sensors indicate changes in the environment, causing the structure to adapt to these new configurations, with a control system handling all these tasks. Thus, it is possible to create a structure with all this embedded technology, ensuring its performance autonomously (SANTANA, 2007).

Piezoelectric (PZT) materials stand out among the available smart materials because they can be manufactured in various shapes, are lightweight, minimally intrusive, and easy to handle, with a wide range of applications (GRIPP; RADE, 2018; LI et al., 2016). These materials also have the characteristic of being used both as sensors and actuators, as well as being easily commercially available and adaptable to different types of structures, such as plates, shells, beams, and curved structures (FARIA, 2006).

Various control techniques have been suggested across different engineering disciplines for vibration attenuation and control (BALAJI; KARTHIK SELVAKUMAR, 2020). When it comes to active control systems, they require the use of amplifiers, associated detection electronics, and control systems, which makes their applications difficult. Among the various approaches, passive control using smart materials has recently attracted significant research attention. The piezoelectric patch associated with a monomodal shunt circuit, in particular, has demonstrated wide applications due to its distinctive characteristics (GRIPP; RADE, 2018). One of these characteristics is the ability to absorb deformation energy from a vibrating system and convert it into electrical energy, which can be harnessed for electronic devices (DE MARQUI et al., 2010; ERTURK, 2011). Consequently, vibration energy harvesting (VEH), or energy harvesting, has emerged as a promising alternative for small-scale devices, particularly for aircraft that require a limited amount of operational power (LI et al., 2016).

Both vibration control and energy harvesting problems require tuning their respective circuits to achieve effective output. For shunt circuits, although there are direct methods that do not require optimization routines to achieve good parameters (RAZE et al., 2020; HAGOOD; FLOTOW, 1991), most studies on parameter tuning in vibration control propose some type of optimization methodology (VIANA; VALDER STEFFEN, 2006; MARAKAKIS et al., 2022; AOUALI et al., 2021). Additionally, small variations in circuit parameters can lead to efficiency losses. Considering this, numerical optimization

techniques that account for the inherent uncertainties in circuit parameters are necessary to obtain more robust designs in such studies. The same problem is faced when considering the parameters of a vibration energy harvester, as the circuit configuration is crucial for reducing internal energy dissipation, achieving impedance matching, and improving energy conversion efficiency (ZHANG et al., 2022; SCHOEFTNER; BUCHBERGER, 2013).

Recent research highlights the intentional integration of nonlinearities in vibration energy harvesters, both to account for the real-world application conditions of structures that inherently possess nonlinearities and to optimize system performance for maximum energy harvesting compared to linear resonant counterparts (MAHMOUDI; KACEM; BOUHADDI, 2014; DREZET; KACEM; BOUHADDI, 2018; AOUALI; KACEM; BOUHADDI, 2022). Despite the model's enrichment, adding nonlinearities increases the complexity of solving the systems and consequently leads to higher computational costs for obtaining results (DAQAQ et al., 2014).

An interesting methodology used to improve structural performance in the initial phase of conceptual design is topology optimization, which has attracted significant attention in recent years due to its potential applications in the development of advanced electromechanical systems. Various solution approaches, such as PEMAP-P (Piezoelectric Material with Penalization and Polarization) (KÖGL; SILVA, 2005; NAKASONE; SILVA, 2010), SIMP (Solid Isotropic Material with Penalization) (GUZMÁN; SILVA; RUBIO, 2020), and MMA (Method of Moving Asymptotes) (HOMAYOUNI-AMLASHI et al., 2020), have been explored. The use of gradient-based mathematical programming (KANG; WANG, 2010) and genetic algorithms (GA) (WANG; TAI; QUEK, 2006), including other methods like Sequential Linear Programming (SLP) (SILVA; KIKUCHI, 1999), has also been employed to solve topology optimization problems for PZT structures (ZHANG; KANG, 2014; KANG; WANG; LUO, 2012; HOMAYOUNI-AMLASHI et al., 2020; NOH; YOON, 2012).

The consideration of PZT material properties in the structure has been investigated using techniques such as parametric positioning (SILVA, 2014; MOTTA MELLO et al., 2014; ZHANG; KANG; LI, 2014) and the density of the PZT layer for vibration control (ZHANG; KANG, 2013) and energy harvesting (ZHENG; CHANG; GEA, 2009). These comprehensive investigations contribute to the advancement of topology optimiza-

tion techniques in piezoelectric structures. Therefore, the objective of this work is to propose an optimal topological design of a vibration energy harvester device, reducing fatigue damage and vibration of the smart structure with the shunt conversion circuit.

1.1 Current research overview

With the aim of situating the topic of the work, a simplified version of the mapping study methodology was carried out, based on the initial methodology described by Bailey et al. (2007) and Petersen et al. (2008), also conducted by Sena et al. (2022). Using terms or keywords for the initial filtering of studies of interest, this system consists of searching bibliographic material registered in scientific databases.

Two scientific databases were used, namely the Coordenação de Aperfeiçoamento de Pessoal de Nível Superior (CAPES) Periodicals Portal (namely Periódicos CAPES) and the Web of Science Portal. Based on the research problem and initial searches on the topic, it was possible to define the main terms of the mapping as "Energy Harvesting", "Fatigue" and "Topology Optimization". Thus, three combinatorial arrangements of these three terms with an "AND" operator allow for narrowing down articles with a theme closely related to the desired one.

The initial search initially employed filters to discard studies not pertinent to the topic, such as works from other fields of knowledge. A scarcity of studies in languages other than English and Portuguese was observed, resulting in the non-application of this initial filter. Additionally, all selected articles for analysis were previously peer-reviewed. The search results can be represented in a Venn diagram, as shown in Fig. 1.1 and Fig. 1.2:

Initially, the proximity of the results between the databases is noticed. The number of results for searches containing only one term was much higher than the rest, indicating that representing these results in the diagram would not be adequate due to the predominance of values. The observation of a considerable amount of work resulting from the combination of two terms suggests a clear academic interest in exploring these specific themes, highlighting their relevance and potential for further analysis. Finally, the inclusion of all three terms in a single search revealed a knowledge gap in the existing literature, emphasizing the importance and necessity of addressing this research topic in

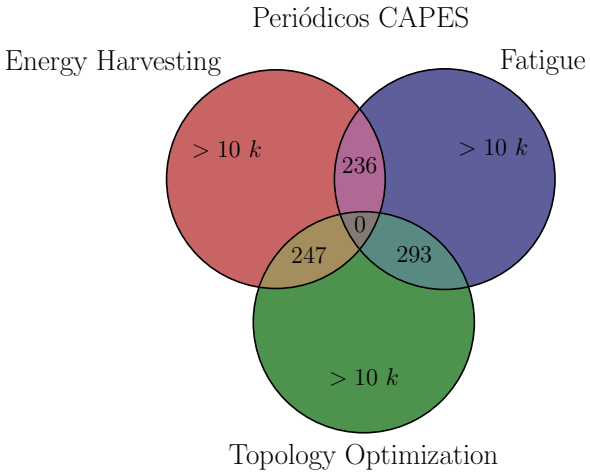

Figure 1.1: Venn diagram of Periódicos CAPES combination search results.

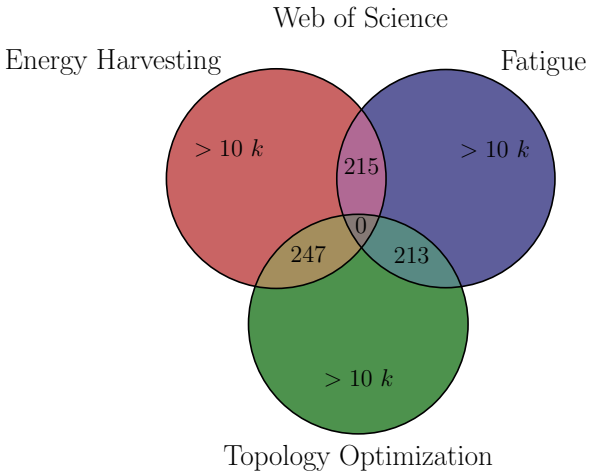

Figure 1.2: Venn diagram of Web of Science combination search results.

the context of the present project.

Another interesting analysis to be made consists of examining the publication year of the results found. In Fig. 1.3 and Fig. 1.4, we can see, for both databases, the number of publications per year. The increasing curve, starting around the 2000s until the present day, indicates the growing interest in the topics, as well as their timeliness. Technological development that allows advances in the manufacturing of smart materials, as well as computational advances in processing large models, explains this increase in academic interest in the theme.

Finally, a quantitative survey by scientific journal was conducted for both databases in Tab. 1.1 and Tab. 1.2, which contain the six journals with the highest

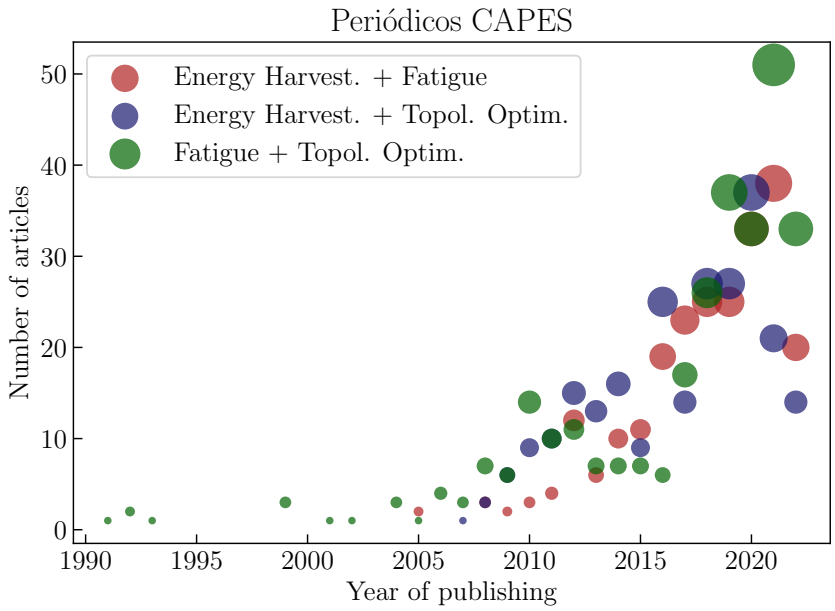

Figure 1.3: Number of publications per year from the Periódicos CAPES platform.

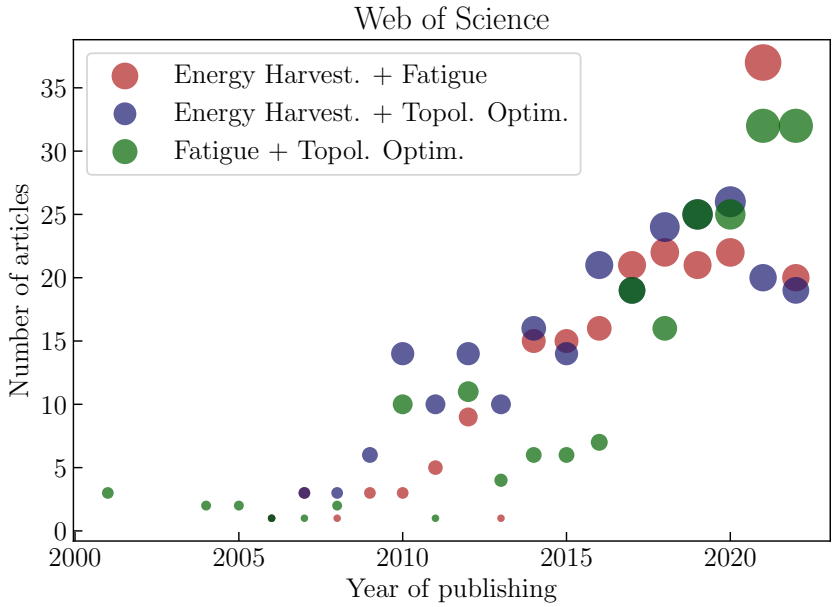

Figure 1.4: Number of publications per year from the Web of Science platform.

number of publications in the research set. This analysis makes it explicit that, despite the close values in the results of the quantitative diagrams, there are still differences between the databases regarding journals.

Periódicos Capes	
Scientific journal	Publications
Structural and multidisciplinary optimization	30
Journal of intelligent material systems and structures	23
Smart materials and structures	21
Journal of physics: Conference series	16
Energies	13
Computer methods in applied mechanics and engineering	13

Table 1.1: Number of publications per scientific journal in the Periódicos CAPES database.

Web of Science	
Scientific journal	Publications
Structural and multidisciplinary optimization	27
Smart materials and structures	20
Journal of intelligent material systems and structures	20
Nano energy	11
Sensors	10
ACS applied materials & interfaces	8

Table 1.2: Number of publications per scientific journal in the Web of Science database.

1.2 Objectives

The objective is to develop a robust optimal methodology for the design of a passive control technique for dynamic systems aimed at reducing the effects of fatigue response and increasing the amount of collected energy, taking into account circuit parameters and the distribution of the piezoelectric layer. Based on the stochastic finite element method with the aid of neural network metamodeling and multi-objective genetic

optimization methods, the aim is to define the optimal design of a structure subjected to external loading for a compromise between maximum harvested vibration energy and minimum fatigue damage accumulation with a reduced CPU computation time.

1.2.1 Specific objectives

- Designing monomodal shunt electrical circuits with different topologies;
- Damping vibrations passively on thin flat panels using monomodal shunt electrical circuits;
- Vibration energy harvesting by associating collection circuits with piezoelectric materials in the structure;
- Performing robust optimization of monomodal shunt circuit parameters to increase fatigue life.
- Performing robust optimization of monomodal shunt circuit parameters to increase harvested energy.
- Proposition, development, and application of robust reduction bases in the computational model and metamodeling using neural networks;
- Adding the topology of the piezoelectric layer to the robust optimization process for increased fatigue life and harvested energy;
- Obtaining the optimal robust characteristics of the system for a compromise between the two objectives.

Chapter II

Background theory

2.1 Multilayer plate models

The displacement field at a specific point on the plate is described, in condensed form, by:

$$\boldsymbol{U}(x,y,z,t) = \begin{Bmatrix} u(x,y,z,t) & v(x,y,z,t) & w(x,y,z,t) \end{Bmatrix}^{\mathsf{T}} . \tag{2.1}$$

According to the First-order Shear Deformation Theory (FSDT) for mechanical modeling of plates, displacements in space are defined by five degrees of freedom, including rotations ψ_{x} and ψ_{y} about the x and y axes, respectively (REDDY, 1997). The relationship between displacements and degrees of freedom is determined as:

$$u(x,y,z,t) = u_0(x,y,t) + z\psi_{\mathrm{x}}(x,y,t) \ , \tag{2.2a}$$

$$v(x,y,z,t) = v_0(x,y,t) + z\psi_{\mathrm{y}}(x,y,t) \ , \tag{2.2b}$$

$$w(x,y,z,t) = w_0(x,y,t) \ . \tag{2.2c}$$

The displacement field can be simplified as:

$$\boldsymbol{U}(x,y,z,t) = \boldsymbol{A}_{\mathrm{u}}(z)\boldsymbol{u}(x,y,t) \ , \tag{2.3}$$

where the matrix $\boldsymbol{A}_{\mathrm{u}}(z)$ and the degree of freedom vector $\boldsymbol{u}(x,y,t)$ are represented by:

$$\boldsymbol{A}_{\mathrm{u}}(z) = \boldsymbol{A}_0 + z\boldsymbol{A}_1 = \begin{bmatrix} 1 & 0 & 0 & 0 & 0 \\ 0 & 1 & 0 & 0 & 0 \\ 0 & 0 & 1 & 0 & 0 \end{bmatrix} + z \begin{bmatrix} 0 & 0 & 0 & 1 & 0 \\ 0 & 0 & 0 & 0 & 1 \\ 0 & 0 & 0 & 0 & 0 \end{bmatrix} , \tag{2.4a}$$

$$\boldsymbol{u}(x,y,t) = \begin{Bmatrix} u_0(x,y,t) & v_0(x,y,t) & w_0(x,y,t) & \psi_{\mathrm{x}}(x,y,t) & \psi_{\mathrm{y}}(x,y,t) \end{Bmatrix} . \tag{2.4b}$$

The relationship between displacements and strains from Linear Elasticity Theory, for the presented FSDT theory, results in:

$$\begin{gathered} \varepsilon_{\mathrm{xx}} = \frac{\partial u}{\partial x} , \quad \varepsilon_{\mathrm{yy}} = \frac{\partial v}{\partial y} , \quad \varepsilon_{\mathrm{zz}} = \frac{\partial w}{\partial z} , \\ \gamma_{\mathrm{yz}} = \frac{\partial v}{\partial z} + \frac{\partial w}{\partial y} , \quad \gamma_{\mathrm{xz}} = \frac{\partial u}{\partial z} + \frac{\partial w}{\partial x} , \quad \gamma_{\mathrm{xy}} = \frac{\partial u}{\partial y} + \frac{\partial v}{\partial x} . \end{gathered} \tag{2.5}$$

Combining Eqs. 2.2 and 2.5, the matrix relationship of Eq. 2.6 is obtained. To facilitate further analysis, the strains are separated according to the type of effect, namely bending and shear:

$$\boldsymbol{\varepsilon}_{\mathrm{b}}(x,y,z,t) = \boldsymbol{D}_{\mathrm{b}}(z)\boldsymbol{u}(x,y,t) = \left(\boldsymbol{D}_{\mathrm{b0}} + z\boldsymbol{D}_{\mathrm{b1}}\right)\boldsymbol{u}(x,y,t) , \tag{2.6a}$$

$$\boldsymbol{\varepsilon}_{\mathrm{s}}(x,y,z,t) = \boldsymbol{D}_{\mathrm{s0}}\boldsymbol{u}(x,y,t) , \tag{2.6b}$$

where:

$$\boldsymbol{D}_{\mathrm{b0}} = \begin{bmatrix} \frac{\partial}{\partial x} & 0 & 0 & 0 & 0 \\ 0 & \frac{\partial}{\partial y} & 0 & 0 & 0 \\ 0 & 0 & 0 & 0 & 0 \\ \frac{\partial}{\partial y} & \frac{\partial}{\partial x} & 0 & 0 & 0 \end{bmatrix} , \quad \boldsymbol{D}_{\mathrm{b1}} = \begin{bmatrix} 0 & 0 & 0 & \frac{\partial}{\partial x} & 0 \\ 0 & 0 & 0 & 0 & \frac{\partial}{\partial y} \\ 0 & 0 & 0 & 0 & 0 \\ 0 & 0 & 0 & \frac{\partial}{\partial y} & \frac{\partial}{\partial x} \end{bmatrix} ,$$

$$\boldsymbol{D}_{\mathrm{s}} = \begin{bmatrix} 0 & 0 & \frac{\partial}{\partial y} & 0 & 1 \\ 0 & 0 & \frac{\partial}{\partial x} & 1 & 0 \end{bmatrix} . \tag{2.7}$$

Based on the theoretical FSDT modeling presented, it is possible to build a model using the finite element method, using an eight-node flat plate element from the Serendipity family (REDDY, 1997), as shown in Fig. 2.1, which presents the element in both natural and local coordinates. The element has unitary dimensions in natural coordinates and dimensions (a, b) in local coordinates, where $\bar{a} = a/2$ and $\bar{b} = b/2$.

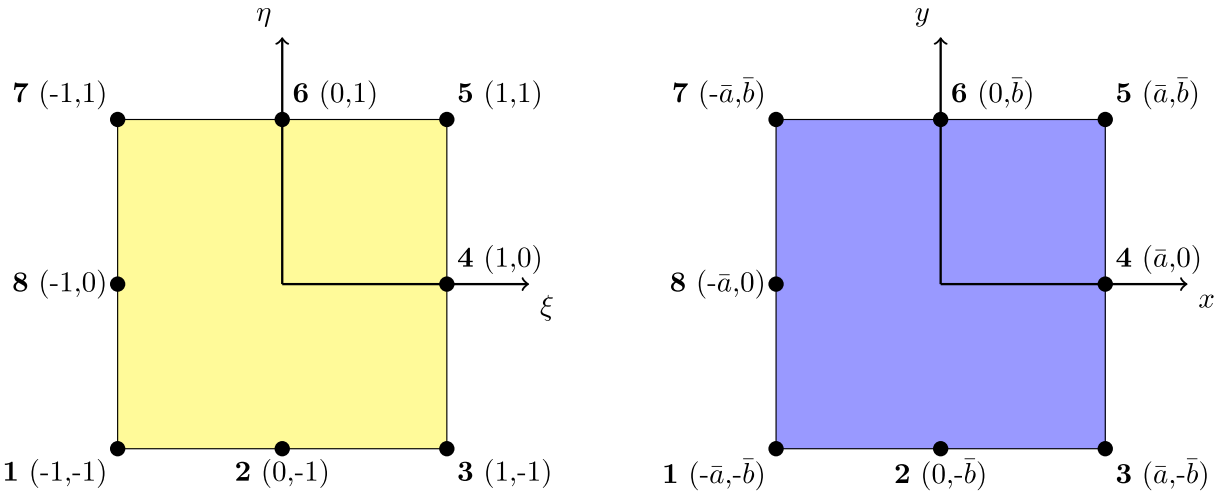

Figure 2.1: Rectangular element with eight nodes, in natural and global coordinates, respectively.

The relationship between natural and local coordinates, with x_i and y_i correspond to the coordinates of the i-th node of the element, is described according to:

$$\xi = \frac{(2x - x_4 - x_8)}{(x_4 - x_8)} = \frac{2x}{a} \quad \leftrightarrow \quad x = \frac{1}{2}\left[\xi(x_4 - x_8) + x_4 + x_8\right] = \frac{\xi a}{2} \ , \tag{2.8a}$$

$$\eta = \frac{(2y - y_6 - y_2)}{(y_6 - y_2)} = \frac{2y}{b} \quad \leftrightarrow \quad y = \frac{1}{2}\left[\eta(y_6 - y_2) + y_6 + y_2\right] = \frac{\eta b}{2} \ . \tag{2.8b}$$

With this relationship in mind, the Jacobian matrix of the linear transformation between natural and local coordinates can be defined as:

$$\boldsymbol{J} = \begin{bmatrix} \dfrac{\partial x}{\partial \xi} & \dfrac{\partial y}{\partial \xi} \\ \dfrac{\partial x}{\partial \eta} & \dfrac{\partial y}{\partial \eta} \end{bmatrix} = \frac{1}{2}\begin{bmatrix} (x_4 - x_8) & 0 \\ 0 & (y_6 - y_2) \end{bmatrix} \ , \tag{2.9}$$

with a determinant equal to $J = \det(\boldsymbol{J}) = ab/4$.

The correspondence between the total displacement of the finite element and the nodal displacement is achieved with the aid of Shape Functions, or Interpolation Functions. These functions are obtained from the polynomial approximation of the node behavior in the element, and for the Serendipity element, they correspond to the expressions:

$$\begin{Bmatrix} N_1(\xi,\eta) \\ N_2(\xi,\eta) \\ N_3(\xi,\eta) \\ N_4(\xi,\eta) \\ N_5(\xi,\eta) \\ N_6(\xi,\eta) \\ N_7(\xi,\eta) \\ N_8(\xi,\eta) \end{Bmatrix} = \frac{1}{4} \begin{Bmatrix} (1-\xi)(1-\eta)(-\xi-\eta-1) \\ 2(1-\xi^2)(1-\eta) \\ (1+\xi)(1-\eta)(\xi-\eta-1) \\ 2(1+\xi)(1-\eta^2) \\ (1+\xi)(1+\eta)(\xi+\eta-1) \\ 2(1-\xi^2)(1+\eta) \\ (1-\xi)(1+\eta)(-\xi+\eta-1) \\ 2(1-\xi)(1-\eta^2) \end{Bmatrix} . \tag{2.10}$$

The finite element then has 5 degrees of freedom per node, totaling 40 degrees of freedom per element, that is, the elemental displacement is equal to $\boldsymbol{u}_{\mathrm{e}} = \{u_i, v_i, w_i, \psi_{\mathrm{x}i}, \psi_{\mathrm{y}i}\}_{[40\times 1]}$, with $i = 1, 2, \ldots 8$. The interpolation matrix $\boldsymbol{N}(\xi,\eta)_{[5\times 40]}$, for the FSDT theory used, follows the structure presented as:

$$\boldsymbol{N} = \begin{bmatrix} N_1 & 0 & 0 & 0 & 0 & N_2 & 0 & 0 & \ldots & 0 & 0 & 0 \\ 0 & N_1 & 0 & 0 & 0 & 0 & N_2 & 0 & \ldots & 0 & 0 & 0 \\ 0 & 0 & N_1 & 0 & 0 & 0 & 0 & N_2 & \ldots & N_8 & 0 & 0 \\ 0 & 0 & 0 & N_1 & 0 & 0 & 0 & 0 & \ldots & 0 & N_8 & 0 \\ 0 & 0 & 0 & 0 & N_1 & 0 & 0 & 0 & \ldots & 0 & 0 & N_8 \end{bmatrix} . \tag{2.11}$$

In a simplified manner, the displacement of the finite element can be represented as:

$$\boldsymbol{u}(\xi,\eta,t) = \boldsymbol{N}(\xi,\eta)\boldsymbol{u}_e(t) \ , \tag{2.12}$$

with:

$$\boldsymbol{U}(\xi,\eta,z,t) = \boldsymbol{A}_{\mathrm{u}}\boldsymbol{N}(\xi,\eta)\boldsymbol{u}_e(t) \ . \tag{2.13}$$

The mechanical strains of the element can be described in terms of the shape matrix:

$$\boldsymbol{\varepsilon}_{\mathrm{b}}(\xi,\eta,z,t) = (\boldsymbol{D}_{\mathrm{b0}} + z\boldsymbol{D}_{\mathrm{b1}})\,\boldsymbol{N}(\xi,\eta)\boldsymbol{u}_e(t) = (\boldsymbol{B}_{\mathrm{b0}} + z\boldsymbol{B}_{\mathrm{b1}})\,\boldsymbol{u}_e \ , \tag{2.14a}$$

$$\boldsymbol{\varepsilon}_{\mathrm{s}}(x,y,z,t) = \boldsymbol{D}_{\mathrm{s0}}\boldsymbol{N}(\xi,\eta)\boldsymbol{u}_e(t) = \boldsymbol{B}_{\mathrm{s0}}\boldsymbol{u}_e \ . \tag{2.14b}$$

With the displacement and strain in hand, it is possible to obtain the mass and stiffness matrices from the calculation of kinetic energy and the strain energy, both obtained respectively by:

$$E_{\mathrm{c}} = \sum_{k=1}^{n} \frac{1}{2} \int_{V_{\mathrm{e}}} \rho_k \dot{\boldsymbol{U}}^{\mathsf{T}} \dot{\boldsymbol{U}} \ \mathrm{d}V_{\mathrm{e}} \ , \tag{2.15a}$$

$$P_{\mathrm{e}} = \sum_{k=1}^{n} \int_{V_{\mathrm{e}}} \boldsymbol{\sigma}^{\mathsf{T}} \boldsymbol{\varepsilon} \ \mathrm{d}V_{\mathrm{e}} \ , \tag{2.15b}$$

where ρ_k is the density of the material of layer k, V_{e} is the volume of the finite element, and $\dot{\boldsymbol{U}}$ is the variation of the displacement field over time. Substituting the values in Eq. 2.15a, the elemental mass matrix is obtained as a function of the physical characteristics of the element:

$$\boldsymbol{M}^{\mathrm{e}}_{\mathrm{uu}} = \sum_{k=1}^{n} \int_{V_{\mathrm{e}}} \rho_k \boldsymbol{N}^{\mathsf{T}} \boldsymbol{A}_{\mathrm{u}}^{\mathsf{T}} \boldsymbol{A}_{\mathrm{u}} \boldsymbol{N} \ \mathrm{d}V_{\mathrm{e}} \ . \tag{2.16}$$

At this point, before performing the integration of the shape functions, the process of factoring the result of the matrix multiplication $\boldsymbol{A} = \boldsymbol{A}_0 + z\boldsymbol{A}_1$ is carried out according to the degree of z. This process facilitates the calculation of the integral and assists in the inclusion of uncertainties present in the parameters through factored random variables of the matrices. The Eq. 2.17 describes the result of the factoring, resulting in the elemental mass matrix of Eq. 2.18, where z_k and z_{k+1} indicate the coordinates of layer k:

$$\bar{\boldsymbol{A}}^{(1)} = \boldsymbol{A}_0^{\mathsf{T}} \boldsymbol{A}_0 \ , \tag{2.17a}$$

$$\bar{\boldsymbol{A}}^{(2)} = \boldsymbol{A}_0^{\mathsf{T}} \boldsymbol{A}_1 + \boldsymbol{A}_1^{\mathsf{T}} \boldsymbol{A}_0 \ , \tag{2.17b}$$

$$\bar{\boldsymbol{A}}^{(3)} = \boldsymbol{A}_1^{\mathsf{T}} \boldsymbol{A}_1 \ , \tag{2.17c}$$

$$\boldsymbol{M}_{\mathrm{uu}}^{\mathrm{e}} = \sum_{k=1}^{n} \int_{z_k}^{z_{k+1}} \int_{-1}^{1} \int_{-1}^{1} \rho_k \boldsymbol{N}^{\mathsf{T}} \left(\bar{\boldsymbol{A}}^{(1)} + z\bar{\boldsymbol{A}}^{(2)} + z^2 \bar{\boldsymbol{A}}^{(3)} \right) \boldsymbol{N} J \, \mathrm{d}\eta \mathrm{d}\xi \mathrm{d}z \ . \tag{2.18}$$

The matrix of material properties depends on the planes of symmetry, reducing the independent stiffness terms in certain types of materials. The classification of these materials is carried out in three main categories: isotropic, orthotropic, and anisotropic (REDDY, 2006). Generalizing the formulation for orthotropic materials, we have the material properties matrix $\boldsymbol{C}$, and the relation between stress and strain $\boldsymbol{\sigma} = \boldsymbol{C}\boldsymbol{\varepsilon}$ is fully described in Eq. 2.19.

$$\begin{Bmatrix} \sigma_1 \\ \sigma_2 \\ \sigma_3 \\ \sigma_4 \\ \sigma_5 \\ \sigma_6 \end{Bmatrix} = \begin{bmatrix} C_{11} & C_{12} & C_{13} & 0 & 0 & 0 \\ C_{21} & C_{22} & C_{23} & 0 & 0 & 0 \\ C_{31} & C_{32} & C_{33} & 0 & 0 & 0 \\ 0 & 0 & 0 & C_{44} & 0 & 0 \\ 0 & 0 & 0 & 0 & C_{55} & 0 \\ 0 & 0 & 0 & 0 & 0 & C_{66} \end{bmatrix} \begin{Bmatrix} \varepsilon_1 \\ \varepsilon_2 \\ \varepsilon_3 \\ \varepsilon_4 \\ \varepsilon_5 \\ \varepsilon_6 \end{Bmatrix} . \tag{2.19}$$

The separation of the properties matrix $\boldsymbol{C}$ is also performed according to the type of effect (bending and shear), as shown in:

$$\boldsymbol{C}_{\mathrm{b}} = \begin{bmatrix} C_{11} & C_{12} & C_{13} & 0 \\ C_{21} & C_{22} & C_{23} & 0 \\ C_{31} & C_{32} & C_{33} & 0 \\ 0 & 0 & 0 & C_{66} \end{bmatrix} , \qquad \boldsymbol{C}_{\mathrm{s}} = \begin{bmatrix} C_{44} & 0 \\ 0 & C_{55} \end{bmatrix} . \tag{2.20}$$

Substituting the terms in the strain energy of Eq. 2.15b, and relating the stress and strain values along with the material properties matrix, we obtain the stiffness matrix in terms of bending and shear effects:

$$\boldsymbol{K}_{\mathrm{b}}^{\mathrm{e}} = \sum_{k=1}^{n} \int_{V_{\mathrm{e}}} \boldsymbol{B}_{\mathrm{bu}}^{\mathsf{T}} \boldsymbol{C}_{\mathrm{b}k} \boldsymbol{B}_{\mathrm{bu}} J \, \mathrm{d}V_{\mathrm{e}} \ , \tag{2.21a}$$

$$\boldsymbol{K}_{\mathrm{s}}^{\mathrm{e}} = \sum_{k=1}^{n} \int_{V_{\mathrm{e}}} \boldsymbol{B}_{\mathrm{su}}^{\mathsf{T}} \boldsymbol{C}_{\mathrm{s}k} \boldsymbol{B}_{\mathrm{su}} J \, \mathrm{d}V_{\mathrm{e}} \ , \tag{2.21b}$$

where $\boldsymbol{B}_{\mathrm{bu}} = (\boldsymbol{B}_{\mathrm{b0}} + z\boldsymbol{B}_{\mathrm{b1}})$ and $\boldsymbol{B}_{\mathrm{su}} = \boldsymbol{B}_{\mathrm{s0}} = \boldsymbol{B}_{\mathrm{s}}$. Analogously to the mass matrix, the terms of the stiffness matrix can be factored in terms of the degree of the term z only for the bending effects matrix, according to:

$$\bar{\boldsymbol{B}}_{\mathrm{b}k}^{(1)} = \boldsymbol{B}_{\mathrm{b0}}^{\mathsf{T}} \boldsymbol{C}_{\mathrm{b}k} \boldsymbol{B}_{\mathrm{b0}} \ , \tag{2.22a}$$

$$\bar{\boldsymbol{B}}_{\mathrm{b}k}^{(2)} = \boldsymbol{B}_{\mathrm{b0}}^{\mathsf{T}} \boldsymbol{C}_{\mathrm{b}k} \boldsymbol{B}_{\mathrm{b1}} + \boldsymbol{B}_{\mathrm{b1}}^{\mathsf{T}} \boldsymbol{C}_{\mathrm{b}k} \boldsymbol{B}_{\mathrm{b0}} \ , \tag{2.22b}$$

$$\bar{\boldsymbol{B}}_{\mathrm{b}k}^{(3)} = \boldsymbol{B}_{\mathrm{b1}}^{\mathsf{T}} \boldsymbol{C}_{\mathrm{b}k} \boldsymbol{B}_{\mathrm{b1}} \ . \tag{2.22c}$$

The result of this factorization corresponds to the elemental stiffness matrix, described as:

$$\boldsymbol{K}_{\mathrm{b}}^{\mathrm{e}} = \sum_{k=1}^{n} \int_{V_{\mathrm{e}}} \left(\bar{\boldsymbol{B}}_{\mathrm{b}k}^{(1)} + z\bar{\boldsymbol{B}}_{\mathrm{b}k}^{(2)} + z^2 \bar{\boldsymbol{B}}_{\mathrm{b}k}^{(3)} \right) J \ \mathrm{d}V_{\mathrm{e}} \ , \tag{2.23a}$$

$$\boldsymbol{K}_{\mathrm{s}}^{\mathrm{e}} = \sum_{k=1}^{n} \int_{V_{\mathrm{e}}} \boldsymbol{B}_{\mathrm{s}}^{\mathsf{T}} \boldsymbol{C}_{\mathrm{s}k} \boldsymbol{B}_{\mathrm{s}} J \ \mathrm{d}V_{\mathrm{e}} \ . \tag{2.23b}$$

With this, it is possible to assemble the global mechanical problem from the global matrices of the system, considering the relation $\boldsymbol{K}_{\mathrm{uu}}^{e} = \boldsymbol{K}_{\mathrm{b}} + \boldsymbol{K}_{\mathrm{s}}$. These are obtained following the classic procedure of connecting the system in finite elements. The result of the equation of motion is described in the mechanical problem by:

$$\boldsymbol{M}_{\mathrm{uu}} \ddot{\boldsymbol{u}}(t) + \boldsymbol{K}_{\mathrm{uu}} \boldsymbol{u}(t) = \boldsymbol{f}(t) \ , \tag{2.24}$$

where $\boldsymbol{u}(t)$ is the vector of global degrees of freedom, and $\boldsymbol{f}(t)$ represents the vector of generalized forces. Considering N as the number of finite elements, the global matrices correspond to:

$$\boldsymbol{M}_{\mathrm{uu}} = \bigcup_{n=1}^{N} \boldsymbol{M}_{\mathrm{uu,n}}^{\mathrm{e}} \ , \qquad \boldsymbol{K}_{\mathrm{uu}} = \bigcup_{n=1}^{N} \boldsymbol{K}_{\mathrm{uu,n}}^{\mathrm{e}} \ . \tag{2.25}$$

2.2 Electromechanical problem

The Mixed Theory is used for modeling laminated composite structures with piezoelectric elements, combining the Equivalent Layer Theory with the Theory of Discrete Equivalent Layers. Thus, mechanical displacements are calculated using a single

equivalent layer, while electrical potentials are discretely distributed along the piezoelectric layers. The mechanical displacement fields are then approximated via FSDT, while the electrical potential is approximated as (SARAVANOS; HEYLIGER, 1995; CHEE, 2000):

$$\Phi_k(x, y, z, t) = L_{kd}(z)\Phi_k(x, y, t) + L_{ku}(z)\Phi_{k+1}(x, y, t) \ , \tag{2.26}$$

where $\Phi_{(k)}$ corresponds to the electrical potential of the k-th layer, Φ_k and Φ_{k+1} are the electrical potentials at the lower and upper interfaces of the k-th layer, and $L_{kd}(z) = (z_{k+1} - z)/(z_{k+1} - z_k)$ and $L_{ku}(z) = (z - z_k)/(z_{k+1} - z_k)$ are the transverse interpolation functions, given by the coordinates of the lower and upper electrical potentials, respectively.

One can also define the electrical potential of the k-th layer in terms of the shape functions $\boldsymbol{N}_{\mathrm{u}}(\xi, \eta)$ and the nodal electrical potentials $\boldsymbol{\phi}_{ek}$, according to (SARAVANOS; HEYLIGER, 1995):

$$\boldsymbol{\Phi}_k(\xi, \eta, z, t) = \boldsymbol{L}_k(z)\boldsymbol{N}_{\mathrm{u}}(\xi, \eta)\boldsymbol{\phi}_{ek}(t) = \boldsymbol{N}_{\Phi}(\xi, \eta, z)\boldsymbol{\phi}_{ek}(t) \ . \tag{2.27}$$

The electric field of layer k is defined by the negative gradient of the electric potential, as shown in (BOYLESTAD, 2004):

$$\boldsymbol{E}_{(k)}(\xi, \eta, z, t) = -\nabla\boldsymbol{N}_{\Phi}(\xi, \eta, z)\boldsymbol{\phi}_{ek}(t) = -\boldsymbol{B}_{\Phi}(\xi, \eta, z)\boldsymbol{\phi}_{ek}(t) \ . \tag{2.28}$$

The elastic-piezoelectric-dielectric matrix, which includes the electromechanical coupling and the relationships between mechanical stresses $\boldsymbol{\sigma}$, mechanical strains $\boldsymbol{\epsilon}$, electric displacements $\boldsymbol{D}$, and electric field $\boldsymbol{E}$, is given by (CHEE, 2000):

$$\begin{Bmatrix} \boldsymbol{\sigma} \\ \boldsymbol{D} \end{Bmatrix} = \begin{bmatrix} \boldsymbol{C}_t & -\boldsymbol{e}_t^{\mathsf{T}} \\ \boldsymbol{e}_t & \boldsymbol{\chi}_t \end{bmatrix} \begin{Bmatrix} \boldsymbol{\epsilon} \\ \boldsymbol{E} \end{Bmatrix} \ , \tag{2.29}$$

where $\boldsymbol{e}_t$ represents the dielectric constants and $\boldsymbol{\chi}_t$ is the electric permittivity matrix, already accounting for the composite fibers. The element stiffness matrices of the electromechanical system are obtained from the deformation energy with the electrical component (FARIA, 2006):

$$\boldsymbol{U}_{\mathrm{e}} = \int_{V_{\mathrm{e}}} \left(\boldsymbol{\epsilon}^{\mathsf{T}} \boldsymbol{\sigma} - \boldsymbol{E}^{\mathsf{T}} \boldsymbol{D} \right) \, \mathrm{d}V_{\mathrm{e}} \; . \tag{2.30}$$

Combining Eqs. 2.29 and 2.30, it is possible to obtain the mechanical, electromechanical, and electrical stiffness matrices from the results of the following integrals (FARIA, 2006):

$$\boldsymbol{K}^{e}_{\mathrm{uu}} = \sum_{k=1}^{n} \int_{z_k}^{z_k+1} \int_{-1}^{1} \int_{-1}^{1} (\boldsymbol{B}_{\mathrm{u}}^{\mathsf{T}} \boldsymbol{C} \boldsymbol{B}_{\mathrm{u}}) J \, \mathrm{d}\eta \mathrm{d}\xi \mathrm{d}z \; , \tag{2.31}$$

$$\boldsymbol{K}^{e}_{\mathrm{u}\Phi} = \sum_{k=1}^{n} \int_{z_k}^{z_k+1} \int_{-1}^{1} \int_{-1}^{1} (\boldsymbol{B}_{\mathrm{u}}^{\mathsf{T}} \boldsymbol{e} \boldsymbol{B}_{\Phi}) J \, \mathrm{d}\eta \mathrm{d}\xi \mathrm{d}z \; , \tag{2.32}$$

$$\boldsymbol{K}^{e}_{\Phi\Phi} = \sum_{k=1}^{n} \int_{z_k}^{z_k+1} \int_{-1}^{1} \int_{-1}^{1} (-\boldsymbol{B}_{\Phi}^{\mathsf{T}} \boldsymbol{\chi} \boldsymbol{B}_{\Phi}) J \, \mathrm{d}\eta \mathrm{d}\xi \mathrm{d}z \; . \tag{2.33}$$

Knowing that $\boldsymbol{B}_{\Phi i} = \boldsymbol{B}_{\Phi i0} + z\boldsymbol{B}_{\Phi i1}$ and that $\boldsymbol{B}_{\Phi 0} = \boldsymbol{B}_{\Phi 0}$, it is possible to perform a new separation in terms of the multipliers z, following:

$$\bar{\boldsymbol{B}}^{(1)}_{\mathrm{b}ik} = \boldsymbol{B}_{\mathrm{b}0}^{\mathsf{T}} \boldsymbol{e}_{\mathrm{b}k} \boldsymbol{B}_{\Phi i0} \; , \tag{2.34a}$$

$$\bar{\boldsymbol{B}}^{(2)}_{\mathrm{b}ik} = \boldsymbol{B}_{\mathrm{b}0}^{\mathsf{T}} \boldsymbol{e}_{\mathrm{b}k} \boldsymbol{B}_{\Phi i1} + \boldsymbol{B}_{\mathrm{b}1}^{\mathsf{T}} \boldsymbol{e}_{\mathrm{b}k} \boldsymbol{B}_{\Phi i0} \; , \tag{2.34b}$$

$$\bar{\boldsymbol{B}}^{(3)}_{\mathrm{b}ik} = \boldsymbol{B}_{\mathrm{b}1}^{\mathsf{T}} \boldsymbol{e}_{\mathrm{b}k} \boldsymbol{B}_{\Phi i1} \; , \tag{2.34c}$$

$$\bar{\boldsymbol{B}}^{(1)}_{ik} = \boldsymbol{B}_{\Phi i0}^{\mathsf{T}} \boldsymbol{\chi}_k \boldsymbol{B}_{\Phi i0} \; , \tag{2.35a}$$

$$\bar{\boldsymbol{B}}^{(2)}_{ik} = \boldsymbol{B}_{\Phi i0}^{\mathsf{T}} \boldsymbol{\chi}_k \boldsymbol{B}_{\Phi i1} + \boldsymbol{B}_{\Phi i1}^{\mathsf{T}} \boldsymbol{\chi}_k \boldsymbol{B}_{\Phi i0} \; , \tag{2.35b}$$

$$\bar{\boldsymbol{B}}^{(3)}_{ik} = \boldsymbol{B}_{\Phi i1}^{\mathsf{T}} \boldsymbol{\chi}_k \boldsymbol{B}_{\Phi i1} \; , \tag{2.35c}$$

which determine the electromechanical and electrical stiffness matrices, respectively:

$$\boldsymbol{K}^{e}_{\mathrm{u}\Phi} = \sum_{k=1}^{n} \int_{z_k}^{z_k+1} \int_{-1}^{1} \int_{-1}^{1} \left[(\bar{\boldsymbol{B}}^{(1)}_{\mathrm{b}ik} + z\bar{\boldsymbol{B}}^{(2)}_{\mathrm{b}ik} + z^2 \bar{\boldsymbol{B}}^{(3)}_{\mathrm{b}ik}) + (\boldsymbol{B}_{\mathrm{s}0}^{\mathsf{T}} \boldsymbol{e}_{\mathrm{s}k} \boldsymbol{B}_{\Phi 0}) \right] J \, \mathrm{d}\eta \mathrm{d}\xi \mathrm{d}z \; , \tag{2.36}$$

$$\boldsymbol{K}^{e}_{\Phi\Phi} = \sum_{k=1}^{n} \int_{z_k}^{z_k+1} \int_{-1}^{1} \int_{-1}^{1} \left[(\bar{\boldsymbol{B}}^{(1)}_{ik} + z\bar{\boldsymbol{B}}^{(2)}_{ik} + z^2\bar{\boldsymbol{B}}^{(3)}_{ik}) + (\boldsymbol{B}^{\mathsf{T}}_{\Phi 0}\boldsymbol{\chi}_k\boldsymbol{B}_{\Phi 0}) \right] J \, \mathrm{d}\eta\mathrm{d}\xi\mathrm{d}z \ . \tag{2.37}$$

The matrix equation of motion, obtained after using classical finite element assembly techniques, is finally described in Eq. 2.38, with $\boldsymbol{K}_{\mathrm{u}\Phi}$ and $\boldsymbol{K}_{\Phi\Phi}$ being the global electromechanical and electrical matrices, respectively, $\boldsymbol{K}_{\mathrm{u}\Phi} = \boldsymbol{K}^{\mathsf{T}}_{\Phi\mathrm{u}}$, $\boldsymbol{\Phi}(t)$, $\boldsymbol{\Phi}(t)$ is the matrix of global electrical potentials, and $\boldsymbol{q}(t)$ is the vector containing global electrical charges:

$$\begin{bmatrix} \boldsymbol{M}_{\mathrm{uu}} & 0 \\ 0 & 0 \end{bmatrix} \begin{Bmatrix} \ddot{\boldsymbol{u}}(t) \\ \ddot{\boldsymbol{\Phi}}(t) \end{Bmatrix} + \begin{bmatrix} \boldsymbol{K}_{\mathrm{uu}} & \boldsymbol{K}_{\mathrm{u}\Phi} \\ \boldsymbol{K}_{\Phi\mathrm{u}} & \boldsymbol{K}_{\Phi\Phi} \end{bmatrix} \begin{Bmatrix} \boldsymbol{u}(t) \\ \boldsymbol{\Phi}(t) \end{Bmatrix} = \begin{Bmatrix} \boldsymbol{f}(t) \\ \boldsymbol{q}(t) \end{Bmatrix} \ . \tag{2.38}$$

2.2.1 Model reduction method

In dynamic modeling, iterative adjustment and optimization processes along with the dimensions of the global matrices due to the large number of degrees of freedom result in high computational costs. Model reduction aims to create a reduced basis that reproduces the dynamic responses of nominal models, even after modifications, which is essential for rapid and economical reanalysis in iterative adjustment and optimization processes, especially in fatigue analysis and topological analysis due to the computationally expensive matrix calculations involved.

Using modal approximations, the system's equations of motion are projected onto a reduced basis to decrease the number of degrees of freedom, thus accelerating the numerical solution of the problem, under the premise that exact responses can be approximated by solutions in a reduced subspace, as:

$$\boldsymbol{u}_{\mathrm{r}} = \boldsymbol{T}\boldsymbol{u} \ , \tag{2.39}$$

where the matrix $\boldsymbol{T} \in \mathbb{C}^{N\times NR}$ corresponds to the reduction basis, $\boldsymbol{u}_{\mathrm{r}} \in \mathbb{C}^{NR}$ denotes the reduced responses, and NR represents the modes retained in the basis, with $NR \ll N$.

In the context of obtaining reduction bases, Gerges (2013) suggested techniques such as the Ritz modal basis enriched with static residuals due to external efforts, suitable for linear structures with known physical characteristics. The basis consists of the first

$\boldsymbol{N}_{\mathrm{m}}$ modes (modal response $\boldsymbol{U}_{\mathrm{mod}}$ of the nominal system) and enriched with the static residual $\boldsymbol{U}_{\mathrm{s}}$ resulting from the application of a unit force $\boldsymbol{F}$ to the structure:

$$\boldsymbol{U}_{\mathrm{s}} = \boldsymbol{K}_{\mathrm{uu}}^{-1}\boldsymbol{F} \ . \tag{2.40}$$

The number of modes to be used depends on specific criteria, with a recommendation of using 1.5 times the maximum desired frequency in the area of interest (MACIEL; BARBOSA, 2015; ROSA; LIMA, 2015). The results of the static analysis should be coupled with truncated vibration modes, resulting in the following enriched basis:

$$\boldsymbol{T} = \begin{bmatrix} \boldsymbol{U}_{\mathrm{mod}} & \boldsymbol{U}_{\mathrm{s}} \end{bmatrix} \ . \tag{2.41}$$

To utilize the reduction basis, the new matrices of mechanical mass and stiffness are calculated by multiplying the respective global matrices by the reduction basis. The electromechanical stiffness matrices are obtained by applying the basis to the mechanical portion of the degrees of freedom, and the electrical stiffness matrix does not undergo the mechanical reduction process, as:

$$\boldsymbol{M}_{\mathrm{uu}}^{\mathrm{r}} = \boldsymbol{T}^{\mathsf{T}}\boldsymbol{M}_{\mathrm{uu}}\boldsymbol{T} \ , \tag{2.42a}$$

$$\boldsymbol{K}_{\mathrm{uu}}^{\mathrm{r}} = \boldsymbol{T}^{\mathsf{T}}\boldsymbol{K}_{\mathrm{uu}}\boldsymbol{T} \ , \tag{2.42b}$$

$$\boldsymbol{K}_{\mathrm{u\Phi}}^{\mathrm{r}} = \boldsymbol{T}^{\mathsf{T}}\boldsymbol{K}_{\mathrm{u\Phi}} \ , \tag{2.42c}$$

$$\boldsymbol{K}_{\mathrm{\Phi u}}^{\mathrm{r}} = \boldsymbol{K}_{\mathrm{\Phi u}}\boldsymbol{T} \ . \tag{2.42d}$$

2.3 Shunt circuit tuning in the model

2.3.1 Inclusion of the shunt circuit in the model

Representing the equations in the Fourier domain, neglecting the initial conditions, we have (ZAMBOLINI-VICENTE, 2000; RIBEIRO; LIMA, 2015):

$$(\boldsymbol{K}_{\mathrm{uu}} + j\omega\boldsymbol{C}_{\mathrm{eq}} - \omega^2\boldsymbol{M}_{\mathrm{uu}})\boldsymbol{U}(\omega) + \boldsymbol{K}_{\mathrm{u\Phi}}\boldsymbol{\Phi}(\omega) = \boldsymbol{F}(\omega) \ , \tag{2.43}$$

$$\boldsymbol{K}_{\Phi \mathrm{u}}\boldsymbol{U}(\omega) + \boldsymbol{K}_{\Phi\Phi}\boldsymbol{\Phi}(\omega) = \boldsymbol{Q}(\omega) \ . \tag{2.44}$$

By combining and rearranging these equations, two Frequency Response Functions (FRFs) can be obtained for the analysis of the electromechanical system. The mechanical FRF $\boldsymbol{H}_{\mathrm{u}}$ is obtained by isolating the mechanical displacements $\boldsymbol{U}$ per applied unit force $\boldsymbol{F}$. The electrical FRF corresponds to the electrical potential $\boldsymbol{\Phi}$ per applied unit force $\boldsymbol{F}$. To do this, Boylestad (2004) presents that the electric current in a circuit corresponds to the variation of electric charge over time, which in turn is proportional to the inverse of impedance times the electric potential, according to Ohm's second law:

$$\frac{dq(t)}{dt} = I(t) = Z^{-1}\Phi(t) \ . \tag{2.45}$$

This relationship allows obtaining the vector of electric charges $\boldsymbol{Q}(\omega)$ that circulates through the shunt circuit given by:

$$\boldsymbol{Q}(\omega) = \left(\frac{1}{j\omega}\right) \boldsymbol{Z}^{-1}(\omega)\boldsymbol{L}_{\mathrm{i}}\boldsymbol{\Phi}(\omega) \ , \tag{2.46}$$

where the matrix of electrical impedances $\boldsymbol{Z}$ and the variable $\boldsymbol{L}_{\mathrm{i}}$ represent the choice between the independent electric potentials associated with the electrodes where the shunt circuits are connected.

Combining the previous equations with Eq. 2.44, we obtain:

$$\boldsymbol{K}_{\Phi \mathrm{u}}\boldsymbol{U}(\omega) + \left(\boldsymbol{K}_{\Phi\Phi} - \frac{\boldsymbol{Z^{-1}(\omega)}}{j\omega}\boldsymbol{L}_{\mathrm{i}}\right) \boldsymbol{\Phi}(\omega) = 0 \ . \tag{2.47}$$

The equation describing the mechanical FRF and the electrical FRF of the electromechanical system is given by Eq. 2.48, considering that the term $[\boldsymbol{KCM}] = (\boldsymbol{K}_{\mathrm{uu}} + j\omega\boldsymbol{C}_{\mathrm{eq}} - \omega^2\boldsymbol{M}_{\mathrm{uu}})$ is used for a better representation of the equations and that for a single circuit the matrix $\boldsymbol{L}_{\mathrm{i}}$ is not necessary:

$$\boldsymbol{H}_{\mathrm{u}}(\omega) = \left[[\boldsymbol{KCM}] - \boldsymbol{K}_{\mathrm{u}\Phi}\left(\boldsymbol{K}_{\Phi\Phi} - \frac{1}{j\omega\boldsymbol{Z}}\right)^{-1}\boldsymbol{K}_{\Phi \mathrm{u}}\right]^{-1} \ , \tag{2.48}$$

$$\boldsymbol{H}_{\Phi}(\omega) = \left[\boldsymbol{K}_{\Phi \mathrm{u}}[\boldsymbol{KCM}]^{-1}\boldsymbol{K}_{\mathrm{u}\Phi} + \frac{1}{j\omega\boldsymbol{Z}} - \boldsymbol{K}_{\Phi\Phi}\right]^{-1}\boldsymbol{K}_{\Phi \mathrm{u}}[\boldsymbol{KCM}]^{-1} \ . \tag{2.49}$$

2.3.2 Shunt circuit tuning

Among the different configurations of shunt circuits described in the literature (LESIEUTRE, 1998), such as resistive, resonant, capacitive, and switched, the choice is made considering the type of application. The resonant circuit, composed of a resistor and an inductor, is relevant due to its ability to adjust to different frequencies, similar to a Dynamic Vibration Absorber (DVA). There are two main configurations: parallel resonant and series resonant. In Fig. 2.2, the representation of a resistive and parallel resonant circuit is shown.

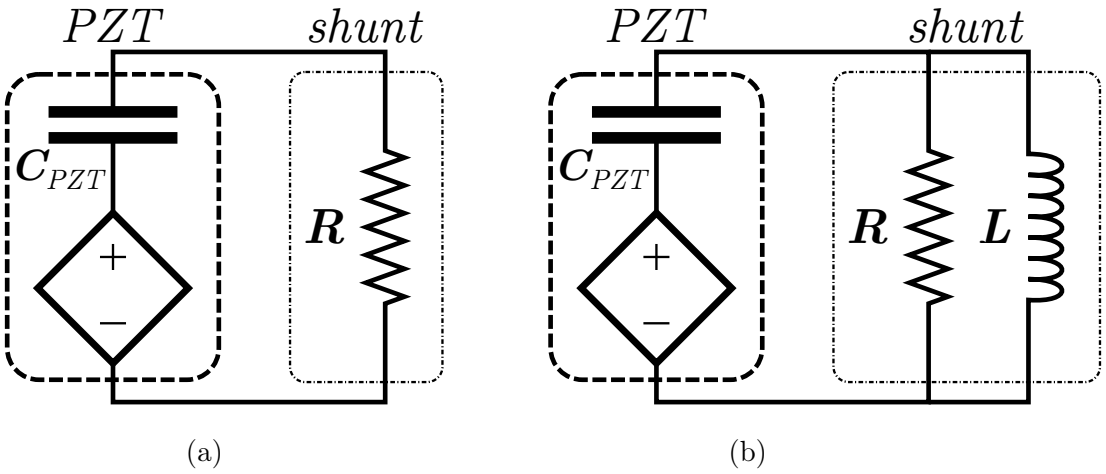

Figure 2.2: Shunt circuits (a) Resistive (b) Resonant in parallel.

For the vibration control of the structure, it is necessary to tune the shunt circuit to the mode or modes that need to be attenuated. Tuning involves adjusting the parameters of the circuit, such as resistors, inductors, and capacitors, to match the equivalent impedance of the circuit to the desired configurations. By analyzing its transfer function and applying the relationships between the natural frequencies and the ideal damping factor for the system, tuning can be performed at a specific frequency based on the formulation proposed by Hagood and Flotow (1991):

$$R_{\text{opt}}^{(\text{s})} = \frac{\sqrt{2}k_{ij}}{C_{\text{pzt}}\omega_n\left(1+k_{ij}^2\right)}\ , \qquad R_{\text{opt}}^{(\text{p})} = \frac{1}{\sqrt{2}C_{\text{pzt}}\omega_n k_{ij}}\ , \tag{2.50}$$

$$L_{\text{opt}}^{(\text{s})} = \frac{1}{C_{\text{pzt}}\omega_n^2\left(1+k_{ij}^2\right)}\ , \qquad L_{\text{opt}}^{(\text{p})} = \frac{1}{C_{\text{pzt}}\omega_n^2\left(1-\frac{k_{ij}^2}{2}\right)}\ , \tag{2.51}$$

where (s) and (p) are indicators of series and parallel circuits respectively, C_{pzt} is the capacitance of the piezoelectric patch, ω_n is the natural frequency in the mode of interest, and k_{ij} is the coupling factor.

The Eqs. 2.50 and 2.51 show that the ideal resistances and inductances for series and parallel resonant circuits vary inversely with the natural frequency of the system. For systems with low natural frequencies, the required inductances are high, making the use of conventional inductors impractical. This drives the interest in synthetic inductors, which are more compact and lightweight, and can achieve suitable inductance values.

The correct choice of the circuit's electrical impedance shifts the peak of the loss factor curve to the frequency that needs to be attenuated, thereby dissipating the vibration in the desired mode (HAGOOD; FLOTOW, 1991). The aim is to design resonant shunt circuits both in parallel (WU, 1998) and in series (FLEMING; BEHRENS; MOHEIMANI, 2002), whose tunings are detailed by Silva (2014).

To obtain the equivalent impedances Z of each circuit, first the impedance of each type of component is calculated (resistor and inductor, respectively), in the frequency domain, by the following relationships:

$$Z_{\text{res}}(\omega) = R \ , \tag{2.52}$$

$$Z_{\text{ind}}(\omega) = j\omega L \ , \tag{2.53}$$

where R is the resistance and L is the inductance. The total impedance values are calculated for the resistive circuit Z_{R}, for the series resonant circuit $Z_{\text{RL}}^{(\text{s})}$, and for the parallel resonant circuit $Z_{\text{RL}}^{(\text{p})}$ by, respectively:

$$Z_{\text{R}} = Z_{\text{res}} \ , \tag{2.54}$$

$$Z_{\text{RL}}^{(\text{s})} = Z_{\text{res}} + Z_{\text{ind}} \ , \tag{2.55}$$

$$Z_{\text{RL}}^{(\text{p})} = \frac{Z_{\text{res}} Z_{\text{ind}}}{Z_{\text{res}} + Z_{\text{ind}}} \ . \tag{2.56}$$

2.3.3 Calculation of power in shunt circuits

In an analysis of ideal direct current circuits, Boylestad (2004) describes that the power of a circuit is given by the relation:

$$P = VI \ , \tag{2.57}$$

with P being the circuit power, V the electrical voltage, and I the electric current passing through the system.

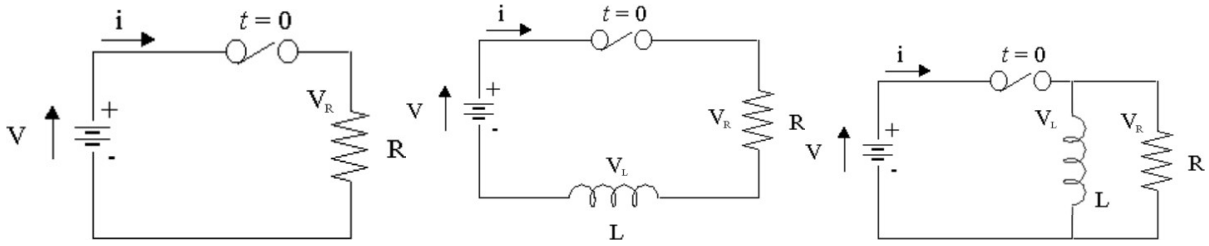

(a) (b) (c)

Figure 2.3: Electrical diagram of the circuits (a) Resistive (b) Resonant in series (c) Resonant in parallel.

To calculate the current values in different circuits, we need to analyze the components present and their configuration. Figure 2.3 displays the necessary information for circuit analysis. For the resistive circuit, the voltage across the circuit is the same as the voltage across the resistor, so $V = V_{\mathrm{R}} = RI$. Similarly, in the parallel resonant circuit, the system voltage is the same as that across both components, with $V = V_{\mathrm{R}} = V_{\mathrm{L}} = RI$. For the series resonant circuit, by Kirchhoff's law, the system voltage equals the sum of the voltages across the components ($V = V_{\mathrm{R}} + V_{\mathrm{L}}$), resulting in:

$$V - RI - L\frac{\mathrm{d}I}{\mathrm{d}t} = 0 \ . \tag{2.58}$$

Solving the Ordinary Differential Equation (ODE), it's possible to obtain the value of the current in the system as a function of time t as shown in the graph in Fig. 2.4:

$$I = \frac{V\left(1 - \mathrm{e}^{\frac{Rt}{L}}\right)}{R} \ . \tag{2.59}$$

Considering a steady-state system to be analyzed, for all described circuits, the resulting power of the system will have the value:

$$P = \frac{V^2}{R} \ . \tag{2.60}$$

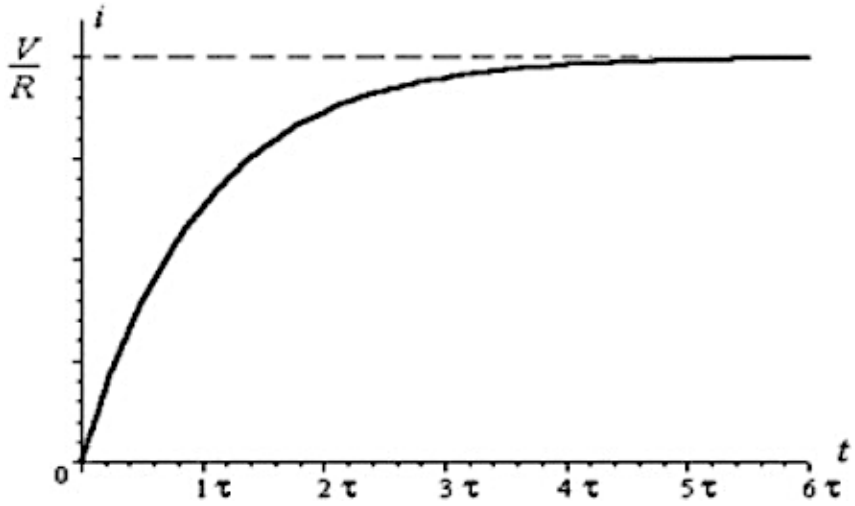

Figure 2.4: Graph of current over time.

In finite element analysis, the calculated voltage corresponds to the electric potential per unit force in the frequency domain $\boldsymbol{H}_{\phi}(\omega)$. Thus, the calculated power $\boldsymbol{\Upsilon}(\omega)$ corresponds to:

$$\boldsymbol{\Upsilon}(\omega) = \frac{\boldsymbol{H}_{\Phi}^{2}}{R} \ . \tag{2.61}$$

In optimization processes and practical applications, the frequency of interest corresponds to the maximum power, i.e., at the natural frequencies of the structure. In the analyses conducted in this work, the calculated value at the frequency ω_1 of the first vibration mode will be used for the calculation of scalar power.

2.4 Stress response under random loads in the frequency domain

The fatigue analysis in the time domain requires knowledge of the entire temporal analysis, thus recording the stress history in the structure. In addition to the high computational cost involved in this type of analysis, another problem with this type of analysis is the evaluation of convolution integrals for numerical analyses, especially in the context of random loadings (LAMBERT; KHALIJ; PAGNACCO, 2007).

An alternative in this case is solving the problem in the frequency domain, where it is only necessary to obtain the external forces and the power spectral densi-

ties (LAMBERT; KHALIJ; PAGNACCO, 2007). According to Bendat (2010), the four statistical properties required to describe a Gaussian random process X are:

- Mean and mean squared - the mean μ_x and the variance s^2 represent the central tendency and dispersion around the process, respectively; the mean square ψ_x^2 provides an estimate of the variance.

- Probability density function - the function $p(x)$ assigns a probability value to each possible value of the discrete random variable, with the area under the curve equaling one.

- Autocorrelation function - the function $R_x(\tau)$ corresponds to the influence of the variation of values along the process, with τ corresponding to the desired lag in measurement.

- Power spectral density - also called the autospectral density function, $\phi_x(\omega)$ represents the rate of change of the mean square value as a function of frequency, obtained from the Fourier transform of the autocorrelation functions.

Assuming an external loading $\boldsymbol{f}(t)$ with properties $\boldsymbol{\phi}_f(\omega)$ and $R_f(\tau)$ equal to the power spectral density matrix and autocorrelation function, resulting in a displacement $\boldsymbol{u}(t)$ and consequently the properties $\boldsymbol{\phi}_u(\omega)$ and $R_u(\tau)$ related to this displacement. These values are calculated using:

$$\boldsymbol{\phi}_{\mathrm{u}}(\omega) = \int_{-\infty}^{\infty} R_{\mathrm{u}}(\tau)\mathrm{e}^{-j\omega t}\ \mathrm{d}\tau\ , \tag{2.62a}$$

$$\boldsymbol{\phi}_{\mathrm{f}}(\omega) = \int_{-\infty}^{\infty} R_{\mathrm{f}}(\tau)\mathrm{e}^{-j\omega t}\ \mathrm{d}\tau\ . \tag{2.62b}$$

After applying the Fourier transform, the spectral density equations result in, now depending on the autocorrelation functions:

$$R_{\mathrm{u}}(\tau) = \int_{-\infty}^{\infty} \boldsymbol{\phi}_{\mathrm{u}}(\omega)\mathrm{e}^{j\omega t}\ \mathrm{d}\tau\ , \tag{2.63a}$$

$$R_{\mathrm{f}}(\tau) = \int_{-\infty}^{\infty} \boldsymbol{\phi}_{\mathrm{f}}(\omega)\mathrm{e}^{j\omega t}\ \mathrm{d}\tau\ . \tag{2.63b}$$

By definition, the autocorrelation function of a stationary random process is given by:

$$R_{\mathrm{u}}(\tau) = \mathbb{E}\left[\boldsymbol{u}(t)\boldsymbol{u}^{\mathsf{T}}(t+\tau)\right] = \mathbb{E}\left[\boldsymbol{u}(t-\tau)\boldsymbol{u}^{\mathsf{T}}(t)\right] \ , \tag{2.64a}$$

$$\mathbb{E}\left[g(x)\right] = \int_{-\infty}^{\infty} g(x)p(x)\ \mathrm{d}x \ , \tag{2.64b}$$

where $\mathbb{E}\left[\bullet\right]$ corresponds to the mathematical expectation or the expected value of a random variable.

Based on the original developments presented by Lambert, Khalij, and Pagnacco (2007), the previous equation is rewritten according to the definition:

$$\begin{aligned} R_{\mathrm{u}}(\tau) &= \mathbb{E}\left[\int_{-\infty}^{\infty}\int_{-\infty}^{\infty} g(\lambda)f(t-\lambda)f^{\mathsf{T}}(t+\tau-\zeta)g^{\mathsf{T}}(\zeta)\ \mathrm{d}\lambda\mathrm{d}\zeta\right] \\ &= \int_{-\infty}^{\infty}\int_{-\infty}^{\infty}\int_{-\infty}^{\infty} g(\lambda)f(t-\lambda)f^{\mathsf{T}}(t+\tau-\zeta)g^{\mathsf{T}}(\zeta)\ \mathrm{d}\lambda\mathrm{d}\zeta\mathrm{d}t \ . \end{aligned} \tag{2.65}$$

The function $g(t)$ corresponds to the system's response to the application of a unit impulse, and is given by:

$$g(t) = \int_{-\infty}^{\infty} \boldsymbol{G}(\omega)\mathrm{e}^{j\omega t}\ \mathrm{d}\omega \ . \tag{2.66}$$

The loading function $\boldsymbol{f}(t)$ can be described according to, considering that it is a stationary and ergodic process:

$$\int_{-\infty}^{\infty} f(t-\lambda)f^{\mathsf{T}}(t+\tau-\zeta)\ \mathrm{d}t = \int_{-\infty}^{\infty} f(t)f^{\mathsf{T}}(t+\tau+\lambda-\zeta)\ \mathrm{d}t = R_{\mathrm{f}}(\tau+\lambda-\zeta) \ . \tag{2.67}$$

Substituting Eq. 2.67 into Eq. 2.66, we obtain:

$$R_{\mathrm{u}}(\tau) = \int_{-\infty}^{\infty}\int_{-\infty}^{\infty} g(\lambda)R_{\mathrm{f}}(\tau+\lambda-\zeta)g^{\mathsf{T}}(\zeta)\ \mathrm{d}\lambda\mathrm{d}\zeta \ . \tag{2.68}$$

With this equation, it is possible to calculate the displacement response of the structure subjected to random loading in the time domain, which does not depend

on t and corresponds to a linear system. By definition, the system response will be a stationary random process if the input excitation also has this characteristic. Therefore, we rewrite the power spectral density function and the autocorrelation function of the loading according to:

$$\boldsymbol{\phi}_{\mathrm{u}}(\omega) = \int_{-\infty}^{\infty} \left[\int_{-\infty}^{\infty} \int_{-\infty}^{\infty} g(\lambda) R_{\mathrm{f}}(\tau + \lambda - \zeta) g^{\mathsf{T}}(\zeta) \, \mathrm{d}\lambda \mathrm{d}\zeta \right] \mathrm{e}^{j\omega t} \, \mathrm{d}\tau \ , \tag{2.69}$$

$$R_{\mathrm{f}}(\tau + \lambda - \zeta) = \int_{-\infty}^{\infty} \boldsymbol{\phi}_{\mathrm{f}}(\omega) \mathrm{e}^{j\omega(\tau+\lambda-\zeta)} \mathrm{d}\omega \ . \tag{2.70}$$

Combining the two previous equations and using the definition of the impulse function $g(t)$, along with some mathematical manipulations, we arrive at:

$$\begin{aligned}
\phi_{\mathrm{u}}(\omega) &= \int_{-\infty}^{\infty} \left[\int_{-\infty}^{\infty} \int_{-\infty}^{\infty} g(\lambda) \int_{-\infty}^{\infty} \boldsymbol{\phi}_{\mathrm{f}}(\omega) \mathrm{e}^{j\omega(\tau+\lambda-\zeta)} \, \mathrm{d}\omega g^{\mathsf{T}}(\zeta) \, \mathrm{d}\lambda \mathrm{d}\zeta \right] \mathrm{e}^{j\omega t} \, \mathrm{d}\tau \\
&= \int_{-\infty}^{\infty} \left[\int_{-\infty}^{\infty} g(\lambda) \mathrm{e}^{-j\omega\lambda} \, \mathrm{d}\lambda \times \int_{-\infty}^{\infty} \boldsymbol{\phi}_{\mathrm{f}}(\omega) \mathrm{e}^{j\omega(\tau+\lambda-\zeta)} \, \mathrm{d}\omega \times \int_{-\infty}^{\infty} g^{\mathsf{T}}(\zeta) \mathrm{e}^{j\omega\zeta} \, \mathrm{d}\zeta \right] \mathrm{e}^{j\omega t} \, \mathrm{d}\tau \\
&= \int_{-\infty}^{\infty} \left[\boldsymbol{G}(\omega) \times \int_{-\infty}^{\infty} \boldsymbol{\phi}_{\mathrm{f}}(\omega) \mathrm{e}^{j\omega(\tau+\lambda-\zeta)} \, \mathrm{d}\omega \times \boldsymbol{G}^{\mathsf{H}}(\omega) \right] \mathrm{e}^{j\omega t} \, \mathrm{d}\tau \\
&= \boldsymbol{G}(\omega) \left[\int_{-\infty}^{\infty} R_{\mathrm{f}}(\tau) \mathrm{e}^{j\omega\tau} \right] \boldsymbol{G}^{\mathsf{H}}(\omega) \ ,
\end{aligned} \tag{2.71}$$

which defines the value of the power spectral density of the displacement. In simplified form:

$$\boldsymbol{\phi}_{\mathrm{u}}(\omega) = \boldsymbol{G}(\omega) \boldsymbol{\phi}_{\mathrm{f}}(\omega) \boldsymbol{G}^{\mathsf{H}}(\omega) \ . \tag{2.72}$$

Considering the displacement-strain relationships, as well as the stress-strain relationships in finite elements, the power spectral density matrix of stress results in:

$$\boldsymbol{\phi}_{\mathrm{s}}(\omega) = \boldsymbol{C}\boldsymbol{B}\boldsymbol{G}(\omega) \boldsymbol{\phi}_{\mathrm{f}}(\omega) \boldsymbol{G}^{\mathsf{H}}(\omega) \boldsymbol{B}^{\mathsf{T}} \boldsymbol{C}^{\mathsf{T}} \ , \tag{2.73}$$

$$\boldsymbol{\phi}_{\mathrm{s}}(\omega) = \begin{bmatrix} \Phi_{\mathrm{xx,xx}} & \Phi_{\mathrm{xx,yy}} & \Phi_{\mathrm{xx,zz}} & \Phi_{\mathrm{xx,yz}} & \Phi_{\mathrm{xx,zx}} & \Phi_{\mathrm{xx,xy}} \\ \Phi_{\mathrm{yy,xx}} & \Phi_{\mathrm{yy,yy}} & \Phi_{\mathrm{yy,zz}} & \Phi_{\mathrm{yy,yz}} & \Phi_{\mathrm{yy,zx}} & \Phi_{\mathrm{yy,xy}} \\ \Phi_{\mathrm{zz,xx}} & \Phi_{\mathrm{zz,yy}} & \Phi_{\mathrm{zz,zz}} & \Phi_{\mathrm{zz,yz}} & \Phi_{\mathrm{zz,zx}} & \Phi_{\mathrm{zz,xy}} \\ \Phi_{\mathrm{yz,xx}} & \Phi_{\mathrm{yz,yy}} & \Phi_{\mathrm{yz,zz}} & \Phi_{\mathrm{yz,yz}} & \Phi_{\mathrm{yz,zx}} & \Phi_{\mathrm{yz,xy}} \\ \Phi_{\mathrm{zx,xx}} & \Phi_{\mathrm{zx,yy}} & \Phi_{\mathrm{zx,zz}} & \Phi_{\mathrm{zx,yz}} & \Phi_{\mathrm{zx,zx}} & \Phi_{\mathrm{zx,xy}} \\ \Phi_{\mathrm{xy,xx}} & \Phi_{\mathrm{xy,yy}} & \Phi_{\mathrm{xy,zz}} & \Phi_{\mathrm{xy,yz}} & \Phi_{\mathrm{xy,zx}} & \Phi_{\mathrm{xy,xy}} \end{bmatrix} . \tag{2.74}$$

2.5 Fatigue analysis in dynamic systems

2.5.1 Spectral moments

According to the definition presented by Bendat (2010), a Gaussian stationary process $\phi_{\mathrm{s}}(\omega)$ has a set of values called spectral moments related to the Power Spectral Density (PSD) of that process, where the spectral moment λ_m has degree m and is calculated by:

$$\lambda_m = \frac{1}{2\pi} \int_{-\infty}^{\infty} \omega^m \phi_{\mathrm{s}}(\omega) \, \mathrm{d}\omega \, . \tag{2.75}$$

From the information contained in the moments, it is possible to calculate some important statistical characteristics, such as the number of crossings of a level b in a period T with positive slope, the number of crossings of zero with positive slope, and the number of maxima in a period T with, repectively:

$$N_{\mathrm{b}} = \frac{T}{2\pi} \sqrt{\frac{\lambda_2}{\lambda_0}} \exp\left(-\frac{b^2}{2\lambda_0}\right) , \tag{2.76}$$

$$N_{\mathrm{b}} = \frac{T}{2\pi} \sqrt{\frac{\lambda_2}{\lambda_0}} , \tag{2.77}$$

$$N_{\mathrm{max}} = \frac{T}{2\pi} \sqrt{\frac{\lambda_4}{\lambda_2}} . \tag{2.78}$$

Another spectral measure of the signal is bandwidth, which can be narrowband or wideband, depending on the presence of significant values in a certain frequency range.

To indicate the bandwidth, the factor α_2 is used, which is the ratio of the number of zero crossings to the number of maxima:

$$\alpha_2 = \frac{N_0}{N_{\max}} = \frac{\lambda_1}{\sqrt{\lambda_0 \lambda_2}} \ , \tag{2.79}$$

which tends to zero for wideband processes and tends to one for narrowband processes.

2.5.2 Uniaxial fatigue life

As described by Chen, Wang, and Guedes Soares (2011), the number of stress cycles that a structure can withstand before failure occurs is known as fatigue life N_f, where fatigue strength is the prediction of this life using the S-N characteristic curve together with the Palmgren-Miner rule. The S-N curve of a material corresponds to a two-segment curve representing the number of cycles it withstands at a given stress range. These values are calculated using linear regression of experimental data, as seen in the ABS Rules for Building and Classing Steel Vessels (ABS, 2010). The S-N curve can be represented as:

$$NS^{m_{f1}} = C_{f_1} \qquad \Longrightarrow \ N \leq 10^7 ciclos \ , \tag{2.80}$$

$$NS^{m_{f2}} = C_{f_2} \qquad \Longrightarrow \ N \geq 10^7 ciclos \ , \tag{2.81}$$

where N equals the number of load cycles to failure, S is the stress range, and m_{f1}, m_{f2}, C_{f1}, and C_{f2} are the exponents and coefficients of fatigue strength as a material characteristic (CHEN; WANG; GUEDES SOARES, 2011). An example of a generic S-N curve is shown in Fig. 2.5, with the correspondence of each stress range and number of cycles.

The Palmgren-Miner rule, first cited by Palmgren (1924) and later combined with Miner's rule, allowed the definition of accumulated damage in a structure subjected to k different stress ranges $S_i (1 \leq i \leq k)$ with n_i cycles each, using:

$$D = \sum_{i=1}^{k} \frac{n_i}{N_i} < 1 \ , \tag{2.82}$$

where N_i is the number of loading cycles under the stress range S_i in the S-N curve. When the accumulated damage value equals 1, fatigue failure occurs.

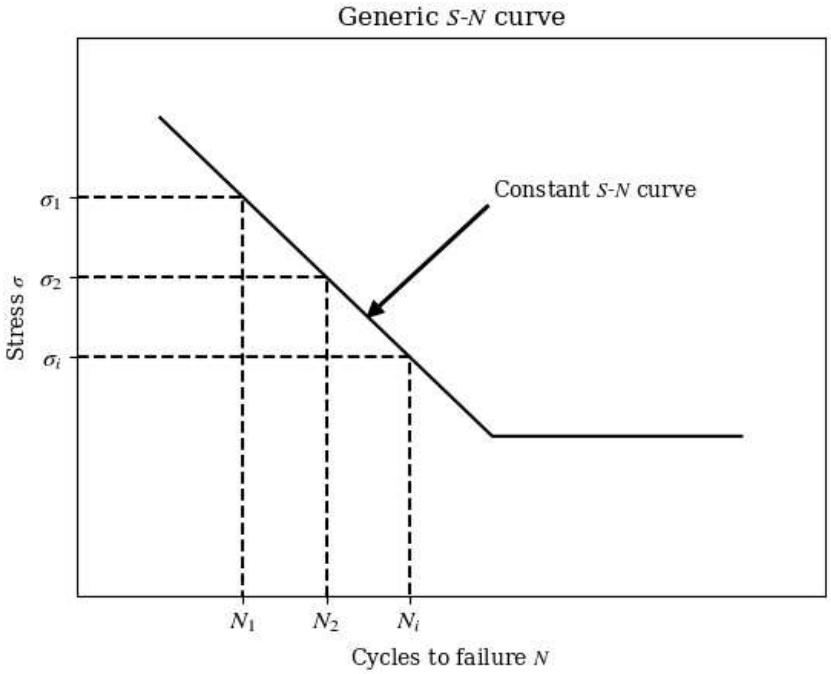

Figure 2.5: Relationship between voltage and cycles to failure on an S-N curve.

Fatigue life can be estimated using accumulated damage and the time interval related to the signal used in the previous calculations. The fatigue life, where T_f is the time considered in the analysis, is obtained with:

$$N_f = \frac{T_f}{D} \ . \tag{2.83}$$

The rainflow method is used to simplify a complex load history into a set of elementary load cycles, using the signal peaks to do so. It was first proposed by Endo et al. (1974), with the signal peaks and valleys being rotated to the vertical axis, resembling a pagoda roof with rainwater running off. The Fig. 2.6 shows an example of a signal being counted using the rainflow method (MILNE; KARIHALOO, 2003).

There are three basic rules for the rainflow method: rainflow starts from each peak or valley, but does not start while rain is flowing downward; rainflow stops when the magnitude of the next peak or valley is equal to or greater than the first peak or valley; rainflow stops when it encounters the previous rainflow. Each interval is counted as half a cycle. When the counted half cycles occur in pairs of equal magnitudes, they form a complete cycle (MILNE; KARIHALOO, 2003).

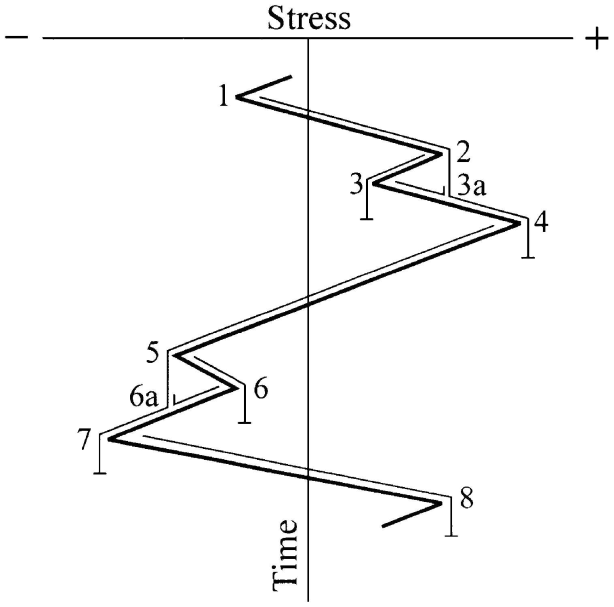

Figure 2.6: Example of the rainflow cycle counting method and name analogy.

2.5.3 Multiaxial fatigue life

The proposition to use the octahedral plane as the plane of maximum stresses, made by Sines (1959), is based on the second invariant of the deviatoric stress tensor (J_2). This proposition is based on the calculation of the damage coefficient D_{sines}, which characterizes the condition of the structure regarding structural system failure. Other factors, such as the mean hydrostatic stress $p_{\text{h}}(t)$ and the multiaxial fatigue strength factors t_{1} and f_{1}, determine whether the system has collapsed by resulting in accumulated damage greater than 1. The formulation of damage by the Sines criterion is:

$$D_{\text{sines}} = \frac{\sqrt{J_{2,\text{a}}} + \alpha \mathbb{E}\left[p_{\text{h}}(t)\right]}{t\_{1}} \,, \tag{2.84}$$

where $\sqrt{J_{2,\text{a}}}$ is the estimate of the square root of the second invariant of the deviatoric stress tensor, $\alpha = \frac{3t\_{1}(S_{\text{ut}}+f\_{1})}{f\_{1}S_{\text{ut}}} - \sqrt{6}$, $\mathbb{E}\left[p_{\text{h}}(t)\right] = \frac{\sigma_{\text{x}}+\sigma_{\text{y}}+\sigma_{\text{z}}}{3}$, and S_{ut} is the ultimate tensile strength.

Estimation of the square root of the second invariant of the deviation tensor

According to Boresi (2011), by definition, we have the second invariant of the deviatoric stress tensor, where $\boldsymbol{d}(t)$ corresponds to the deviatoric stress tensor:

$$\sqrt{J_2(t)} = \sqrt{\frac{1}{2}\boldsymbol{d}(t) \cdot \boldsymbol{d}(t)} \ . \tag{2.85}$$

In the specific case where the loading is proportional and in phase, the values of the second invariant are calculated using the stress components:

$$\sqrt{J_{2,\mathrm{a}}} = \sqrt{\frac{1}{6}\left[(\sigma_{\mathrm{x,a}} - \sigma_{\mathrm{y,a}})^2 + (\sigma_{\mathrm{y,a}} - \sigma_{\mathrm{z,a}})^2 + (\sigma_{\mathrm{z,a}} - \sigma_{\mathrm{x,a}})^2 + 6(\tau_{\mathrm{xy,a}} + \tau_{\mathrm{yz,a}} + \tau_{\mathrm{xz,a}})^2\right]} \ , \tag{2.86}$$

with $\sigma_{i,\mathrm{a}}$ and $\tau_{ij,\mathrm{a}}$ being the estimated values for the normal and shear stresses, respectively.

The Eq. 2.86 can be simplified based on a decomposition in a five-dimensional Euclidean space $\boldsymbol{D}_e(t) = [D_1(t), D_2(t), D_3(t), D_4(t), D_5(t)]$, where (LAMBERT; PAGNACCO; KHALIJ, 2010):

$$D_1(t) = \frac{\sqrt{3}}{2}\left(\sigma_{\mathrm{x}}(t) - \frac{1}{3}\sigma_{\mathrm{y}}(t) - \frac{1}{3}\sigma_{\mathrm{z}}(t)\right) \ , \tag{2.87a}$$

$$D_2(t) = \frac{1}{2}\sigma_{\mathrm{y}}(t) - \frac{1}{2}\sigma_{\mathrm{z}}(t) \ , \tag{2.87b}$$

$$D_3(t) = \tau_{\mathrm{xy}}(t) \ , \tag{2.87c}$$

$$D_4(t) = \tau_{\mathrm{yz}}(t) \ , \tag{2.87d}$$

$$D_5(t) = \tau_{\mathrm{zx}}(t) \ . \tag{2.87e}$$

The Eq. 2.86 can be rewritten considering the new Euclidean space, resulting in:

$$\sqrt{J_2(t)} = \sqrt{D_1^2(t) + D_2^2(t) + D_3^2(t) + D_4^2(t) + D_5^2(t)} \ , \tag{2.88}$$

or, considering proportional loading in phase:

$$\sqrt{J_{2,\mathrm{a}}} = \sqrt{D_{1,\mathrm{a}}^2 + D_{2,\mathrm{a}}^2 + D_{3,\mathrm{a}}^2 + D_{4,\mathrm{a}}^2 + D_{5,\mathrm{a}}^2} \ . \tag{2.89}$$

Other methods for estimating the value of $\sqrt{J_{2,\mathrm{a}}}$ are necessary in cases where the loading is non-proportional and out of phase. Li and Freitas (2002) describes a method that considers an ellipse with two semi-axes R_1 and R_2 that encloses the circumscribed loading path, thus including the effects of non-proportionality. To calculate the value of the square root of the second invariant according to the ellipse shown in Fig. 2.7, we use:

$$\sqrt{J_{2,\mathrm{a}}} = \sqrt{R_1^2 + R_2^2} \ . \tag{2.90}$$

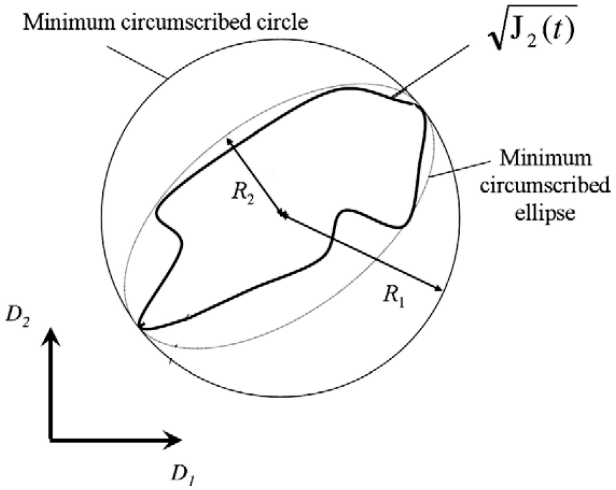

Figure 2.7: Load path and minimum ellipse circumscribed according to the theory presented (LAMBERT; PAGNACCO; KHALIJ, 2010).

This formulation is limited to two-dimensional space, making it impossible to apply to the initially presented case. Therefore, Lambert, Pagnacco, and Khalij (2010) propose a theory to include the loading path in a prismatic shell, better representing non-proportional loadings to obtain the value of $\sqrt{J_{2,\mathrm{a}}}$. We then rewrite Eq. 2.90 in terms of the dimensions of the prismatic shell, resulting in:

$$\sqrt{J_{2,\mathrm{a}}} = \sqrt{R_1^2 + R_2^2 + R_3^2 + R_4^2 + R_5^2} \ . \tag{2.91}$$

Adaptation of the Sines criterion for random loading

In the case of random variables, the determination of values is not performed directly. Instead, the value of the mathematical expectation, or expected value, is calculated. The fatigue index for the Sines criterion is calculated, for random loadings, according to:

$$\mathbb{E}\left[D_{\mathrm{sines}}\right] = \frac{\mathbb{E}\left[\sqrt{J_{2,\mathrm{a}}}\right] + \alpha \mathbb{E}\left[p_{\mathrm{h}}(t)\right]}{t_{\_1}} \ . \tag{2.92}$$

Considering zero hydrostatic pressure, the problem results in knowing the property $t_{\_1}$ and estimating $\mathbb{E}\left[\sqrt{J_{2,\mathrm{a}}}\right]$, as in:

$$\mathbb{E}\left[D_{\text{sines}}\right] = \frac{\mathbb{E}\left[\sqrt{J_{2,\text{a}}}\right]}{t_{\_1}} \ , \tag{2.93}$$

where:

$$\mathbb{E}\left[\sqrt{J_{2,\text{a}}}\right] \approx \sqrt{\mathbb{E}\left[R_1^2\right] + \mathbb{E}\left[R_2^2\right] + \mathbb{E}\left[R_3^2\right] + \mathbb{E}\left[R_4^2\right] + \mathbb{E}\left[R_5^2\right]} \ . \tag{2.94}$$

The following steps are necessary to determine the axes R_i of the prism in the five-dimensional space for the case of random loading (LAMBERT; PAGNACCO; KHALIJ, 2010):

a. $D_i'(t) \rightarrow$ one of the vector components $\boldsymbol{D}'(t)$, linearly associated to $\boldsymbol{D}(t)$ through the equation $\boldsymbol{D}'(t) = \boldsymbol{P}_{\text{D}}\boldsymbol{D}(t)$;

b. $\boldsymbol{P}_{\text{D}} \rightarrow$ obtained through the eigenvectors of the covariance matrix $\mathbb{V}\left[\boldsymbol{D}(t)\right]$;

c. $X_i(t) = D_i'(t) - \mathbb{E}\left[D_i'\right] \rightarrow$ a Gaussian random process with zero mean and spectral moments $\lambda_{m,i}(D_i')$;

d. $N(\alpha_0, 0, T) \rightarrow$ the number of passages by the value α_0 in the $[0, T]$ interval;

e. $T_{\text{f}}(\alpha_0) \rightarrow$ the time of the first crossing at the level α_0;

f. $\mathfrak{R}_i = \max\limits_{0 \leq t \leq T} X_i(t) \rightarrow$ the maximum value reached by X_i in the $[0, T]$ interval.

It is possible to calculate the probability that the maximum value does not exceed the level α_0 in a time interval $(0, T)$ using:

$$\mathbb{P}\left[\mathfrak{R}_i \leq \alpha_0\right] = \mathbb{P}\left[T_{\text{f}}(\alpha_0) > T\right] = \mathbb{P}\left[N(\alpha_0, 0, T) = 0\right] \ . \tag{2.95}$$

In Eq. 2.76, the expectation of the number of crossings results in:

$$\mathbb{E}\left[N(\alpha_0, 0, T)\right] = \frac{T}{2\pi}\sqrt{\frac{\lambda_{2,i}}{\lambda_{0,i}}}\exp\left(-\frac{\alpha_0^2}{2\lambda_{0,i}}\right) = N_{0,i}\exp\left(-\frac{\alpha_0^2}{2\lambda_{0,i}}\right) \ , \tag{2.96}$$

with $N_{0,i}$ equal to the number of crossings through zero with positive slope.

According to Preumont (1985), the Gumbel distribution is the best fit for the previous equation, and it is calculated according to:

$$P_{\mathrm{R}_i}(\alpha) = \exp\left(-\exp\left(\frac{\mu - \alpha_0}{\beta}\right)\right) . \tag{2.97}$$

The Gumbel distribution assumes that previous states are not necessary for predicting subsequent states as long as the current state is known, according to a Markovian process. The mode μ_i, dispersion β_i, bandwidth parameters κ_u and κ_a, and the irregularity factor function δ_i are calculated following:

$$\mu_i = \sqrt{2\ln\left(\kappa_{\mathrm{u}} N_{0,i}\right)} , \tag{2.98a}$$

$$\beta_i = \frac{1}{\sqrt{2\ln\left(\kappa_{\mathrm{a}} N_{0,i}\right)}} , \tag{2.98b}$$

$$\kappa_{\mathrm{u}} = \begin{cases} 1.5(1 - \mathrm{e}^{1.8\delta_i}) & \delta_i < 0.5 \\ 0.94 & \delta_i \geq 0.5 \end{cases} , \tag{2.98c}$$

$$\kappa_{\mathrm{a}} = \begin{cases} 7\delta_i & \delta_i < 0.5 \\ 4.05 & \delta_i \geq 0.5 \end{cases} , \tag{2.98d}$$

$$\delta_i = \sqrt{1 - \frac{\lambda_{1,i}^2}{\lambda_{0,i}\lambda_{2,i}}} . \tag{2.98e}$$

Using the properties of the Gumbel distribution, it is possible to formulate the expectation and variance of R_i as described in:

$$\mathbb{E}\left[\mathfrak{R}_i\right] = \sqrt{\lambda_{0,i}}(\mu_i + \gamma\beta_i) , \tag{2.99a}$$

$$\mathbb{V}\left[\mathfrak{R}_i\right] = \lambda_{0,i}\frac{(\beta_i\pi)^2}{6} , \tag{2.99b}$$

where $\gamma \approx 0.57721$ is the Euler-Mascheroni constant.

The statistical characterization of $\sqrt{\mathfrak{J}_{2,\mathrm{a}}} = \sqrt{\mathfrak{R}_1^2 + \mathfrak{R}_2^2 + \mathfrak{R}_3^2 + \mathfrak{R}_4^2 + \mathfrak{R}_5^2}$ is performed based on the statistical properties of the semi-axes $\mathfrak{R}_i$, assuming that there is no correlation between them. Estimating the square of the square root of the second invariant, we have:

$$\mathbb{E}\left[\mathfrak{J}_{2,\mathrm{a}}\right] = \mathbb{E}\left[\mathfrak{R}_1^2\right] + \mathbb{E}\left[\mathfrak{R}_2^2\right] + \mathbb{E}\left[\mathfrak{R}_3^2\right] + \mathbb{E}\left[\mathfrak{R}_4^2\right] + \mathbb{E}\left[\mathfrak{R}_5^2\right] , \tag{2.100a}$$

$$\mathbb{V}\left[\mathfrak{J}_{2,\mathrm{a}}\right] = \mathbb{V}\left[\mathfrak{R}_1^2\right] + \mathbb{V}\left[\mathfrak{R}_2^2\right] + \mathbb{V}\left[\mathfrak{R}_3^2\right] + \mathbb{V}\left[\mathfrak{R}_4^2\right] + \mathbb{V}\left[\mathfrak{R}_5^2\right] . \tag{2.100b}$$

Then, the lack of correlation between the random variables allows for the relationships to be performed:

$$\mathbb{E}\left[\mathfrak{R}_i^2\right] = \mathbb{E}\left[\mathfrak{R}_i\right]^2 + \mathbb{V}\left[\mathfrak{R}_i\right] \ , \tag{2.101a}$$

$$\mathbb{V}\left[\mathfrak{R}_i^2\right] = \mathbb{E}\left[\left(\mathfrak{R}_i^2 - \mathbb{E}\left[\mathfrak{R}_i^2\right]\right)^2\right] = \mathbb{E}\left[\mathfrak{R}_i^4\right] - \mathbb{E}\left[\mathfrak{R}_i^2\right] \ . \tag{2.101b}$$

The only unknown in Eq. 2.101 is the term $\mathbb{E}\left[\mathfrak{R}_i^4\right]$, which can be obtained from statistical properties of random variables, corresponding to:

$$\mathbb{E}\left[\mathfrak{R}_i^4\right] = \int_{-\infty}^{\infty} \mathfrak{R}_i^4 \ \mathrm{d}P_{\mathfrak{R}_i} = 4\mathbb{E}\left[\mathfrak{R}_i\right]^2 \mathbb{V}\left[\mathfrak{R}_i\right] + \frac{22}{5}\mathbb{V}\left[\mathfrak{R}_i\right]^2 + 48\zeta_3\frac{\sqrt{6}}{\pi^3}\mathbb{E}\left[\mathfrak{R}_i\right]\mathbb{V}\left[\mathfrak{R}_i\right]^{3/2} \ , \tag{2.102}$$

with $\zeta_3 = 1.20206$ being the Apery constant.

From the assumption that $\sqrt{\mathfrak{J}_{2,\mathrm{a}}}$, being a random variable and a combination of $\mathfrak{R}_i$, is also described by the Gumbel probability distribution, it is possible to establish the relationship described in:

$$\mathbb{E}\left[\mathfrak{J}_{2,\mathrm{a}}^2\right] = 4\mathbb{E}\left[\sqrt{\mathfrak{J}_{2,\mathrm{a}}}\right]^2 \mathbb{V}\left[\sqrt{\mathfrak{J}_{2,\mathrm{a}}}\right] + \frac{22}{5}\mathbb{V}\left[\sqrt{\mathfrak{J}_{2,\mathrm{a}}}\right]^2 + 48\zeta_3\frac{\sqrt{6}}{\pi^3}\mathbb{E}\left[\sqrt{\mathfrak{J}_{2,\mathrm{a}}}\right]\mathbb{V}\left[\sqrt{\mathfrak{J}_{2,\mathrm{a}}}\right]^{3/2} \ . \tag{2.103}$$

The expectation and variance expressions are then rewritten as follows:

$$\mathbb{E}\left[\mathfrak{J}_{2,\mathrm{a}}^2\right] = \mathbb{E}\left[\mathfrak{J}_{2,\mathrm{a}}\right]^2 - \mathbb{V}\left[\mathfrak{J}_{2,\mathrm{a}}\right] \ , \tag{2.104a}$$

$$\mathbb{V}\left[\sqrt{\mathfrak{J}_{2,\mathrm{a}}}\right] = \mathbb{E}\left[\mathfrak{J}_{2,\mathrm{a}}\right] - \mathbb{E}\left[\sqrt{\mathfrak{J}_{2,\mathrm{a}}}\right]^2 \ . \tag{2.104b}$$

By substituting Eq. 2.103 into Eq. 2.104, we obtain an equation whose only unknown is the value $\mathbb{E}\left[\sqrt{\mathfrak{J}_{2,\mathrm{a}}}\right]$, as shown in:

$$\begin{aligned}\mathbb{E}\left[\mathfrak{J}_{2,\mathrm{a}}\right]^2 + \mathbb{V}\left[\mathfrak{J}_{2,\mathrm{a}}\right] - 4\mathbb{E}\left[\sqrt{\mathfrak{J}_{2,\mathrm{a}}}\right]^2 \left(\mathbb{E}\left[\mathfrak{J}_{2,\mathrm{a}}\right] - \mathbb{E}\left[\sqrt{\mathfrak{J}_{2,\mathrm{a}}}\right]^2\right) - \frac{22}{5}\left(\mathbb{E}\left[\mathfrak{J}_{2,\mathrm{a}}\right] - \mathbb{E}\left[\sqrt{\mathfrak{J}_{2,\mathrm{a}}}\right]^2\right)^2 \\ - 48\zeta_3\frac{\sqrt{6}}{\pi^3}\mathbb{E}\left[\sqrt{\mathfrak{J}_{2,\mathrm{a}}}\right]\left(\mathbb{E}\left[\mathfrak{J}_{2,\mathrm{a}}\right] - \mathbb{E}\left[\sqrt{\mathfrak{J}_{2,\mathrm{a}}}\right]^2\right)^{3/2} = 0 \ .\end{aligned} \tag{2.105}$$

The estimation of the value of $\mathbb{E}\left[\sqrt{\mathfrak{J}_{2,\mathrm{a}}}\right]$ is performed by solving the previous equation using the Newton-Raphson method, thus obtaining the second invariant of the

deviatoric tensor inserted in a random process. The Sines coefficient is finally calculated for fatigue damage expectation.

2.6 Multi-objective optimization

The existence of multiple objectives in a problem results in a set of optimal solutions, known as Pareto-optimal solutions, instead of a single solution. In the absence of additional information, it is not possible to determine the superiority of one Pareto-optimal solution over another. This requires the user to seek as many Pareto-optimal solutions as possible so that, based on prior problem information, they can define the best outcome. Classical optimization methods, including multi-criteria decision-making methods, propose converting the multi-objective optimization problem into a single-objective optimization problem, emphasizing one Pareto-optimal solution at a time. This methodology requires repeating the optimization process, hoping to obtain a different solution in each simulation run, which has proven to be not very effective (ESCHENAUER; OSYCZKA, 1990; DEB et al., 2002).

A vector of objective functions $\boldsymbol{F}_o(\boldsymbol{x})$ of size m, with a vector $\boldsymbol{G}_{\mathrm{c}}(\boldsymbol{x})$ of constraints with boundary conditions, dependent on the design variable vector $\boldsymbol{x}$ belonging to the search space Ω, form a multi-objective optimization problem as follows:

$$\begin{aligned} \min_{\boldsymbol{x}} \quad & \boldsymbol{F}_{\mathrm{o}}(\boldsymbol{x}) = \begin{bmatrix} f_{\mathrm{o}1}(\boldsymbol{x}) & f_{\mathrm{o}2}(\boldsymbol{x}) & \dots & f_{om}(\boldsymbol{x}) \end{bmatrix}^{\mathsf{T}} \\ \text{s.t.} \quad & \boldsymbol{G}_{\mathrm{c}}(\boldsymbol{x}) \leq 0 \\ & \boldsymbol{x} \in \Omega \end{aligned} \quad . \tag{2.106}$$

Among the algorithms available for multi-objective optimization problems, the Non-dominated Sorting Genetic Algorithm (NSGA) proves to be a good option due to its efficiency in finding the Pareto solution. Initially described by Srinivas and Deb (1994), it assigns a cost to each solution based on its dominance. First, a population of solutions is randomly generated and evaluated for the objective functions. The solutions are then saved in a temporary population containing the non-dominated solutions in another set

with an assigned cost of 1. These solutions are then recombined using mutation methods, and the process restarts for the second generation.

An evolution of this algorithm was developed by the same authors (DEB et al., 2002). NSGA-II calculates the cost of a solution considering not only the solutions that dominate it, but also the solutions it dominates. A crowding distance is also calculated for each solution to implement elitism. To calculate this distance, first the larger and closer values, as well as the smaller and closer values of each objective function, are calculated as follows (SIMON, 2013):

$$f_{oi}^{-}(x) = \max_{y} \{ f_{oi}(y) \ni f_{oi}(y) < f_{oi}(x) \} \ , \tag{2.107}$$

$$f_{oi}^{+}(x) = \min_{y} \{ f_{oi}(y) \ni f_{oi}(y) > f_{oi}(x) \} \ , \tag{2.108}$$

where $f_{oi}(x)$ is the value of the i-th objective function of variable x, and the crowding distance is calculated as follows:

$$d(x) = \sum_{i=1}^{k} \left(f_{oi}^{+}(x) - f_{oi}^{-} \right) \ . \tag{2.109}$$

In each generation, the non-dominated curves form a scale according to their rank (or cost). From the moment the rank 1 solutions reach a value desired by the designer, the optimization process is terminated, as shown in Fig. 2.8.

2.6.1 Robust multi-objective optimization

Numerical optimization techniques can face obstacles due to several factors. For example, objective functions may have discontinuities, design variables may have different sensitivities, estimating initial values for these variables may be complicated, and model results may contain noise. Furthermore, most real-world applications have uncertainties associated with the problem, since some parameters are obtained by estimates or cannot be calculated in advance (VANDERPLAATS, 1984; KÖBIS, 2013).

Taking uncertainties into account in design variables adds complexity to the optimization problem, and although the literal meaning of optimization differs from the meaning of robustness (MARCZYK, 2000), this consideration is essential to ensure optimal and robust solutions, especially for more realistic practical applications. Further-

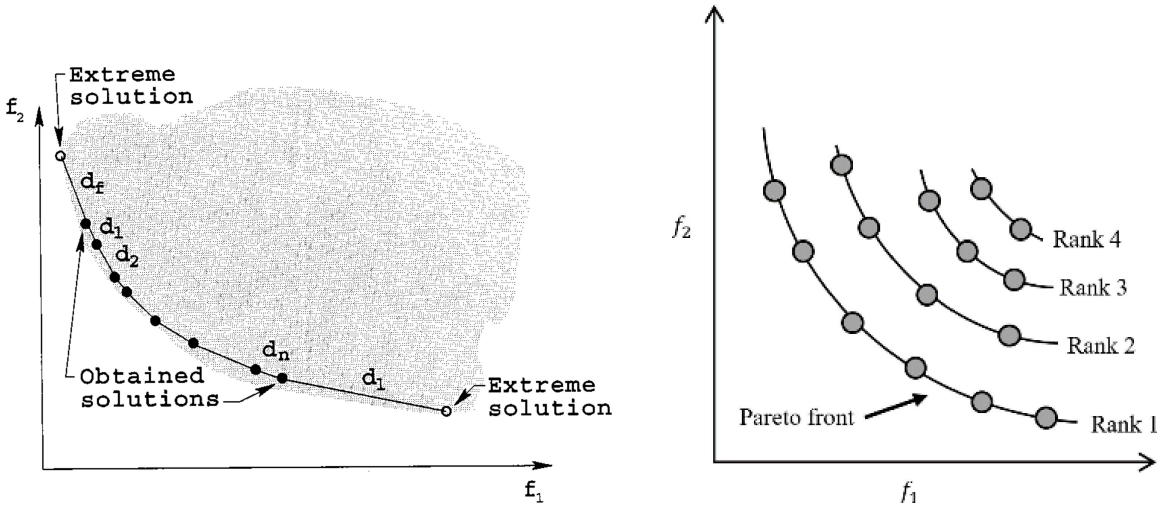

(a) (b)

Figure 2.8: Pareto curves (a) Population of solutions (DEB et al., 2002) (b) Domination of solutions by rank (VERMA; PANT; SNASEL, 2021).

more, it is important to mention that the need for high precision in manufacturing can significantly increase the cost of building optimized systems, making them economically unfeasible in many cases (BEYER; SENDHOFF, 2007; MOREIRA, 2015).

Among the techniques for robust optimization design, the vulnerability function methodology proves to be efficient in describing a set of sub-optimal solutions with different degrees of sensitivity to variations in design variables. These functions simultaneously minimize the objective functions and the vulnerability of each of these functions. As a measure of dispersion, the problem described in Eq. 2.106 now also considers the vulnerability functions $\mathcal{V}_{f_{\mathrm{o}1}}$ of each objective $f_{oi}(\boldsymbol{x})$ (LIMA, 2007):

$$\begin{aligned} \min_{\boldsymbol{x}} \quad & \boldsymbol{F}_{\mathrm{o}}^{\mathrm{R}}(\boldsymbol{x}) = \begin{bmatrix} f_{\mathrm{o}1}(\boldsymbol{x}) & \mathcal{V}_{f_{\mathrm{o}1}}(\boldsymbol{x}) & f_{\mathrm{o}2}(\boldsymbol{x}) & \mathcal{V}_{f_{\mathrm{o}2}}(\boldsymbol{x}) & \dots & f_{om}(\boldsymbol{x}) & \mathcal{V}_{f_{om}}(\boldsymbol{x}) \end{bmatrix}^{\mathsf{T}} \\ \text{s.t.} \quad & \boldsymbol{G}_{\mathrm{c}}(\boldsymbol{x}) \leq 0 \\ & \boldsymbol{x} \in \Omega \end{aligned} \quad , \tag{2.110}$$

with the vulnerability functions, also known as coefficient of variation, being defined by the dispersion measure:

$$\mathcal{V}_{f_o} = \frac{\sigma_{f_o}}{\mu_{f_o}} \ , \tag{2.111}$$

where σ_{f_o} and μ_{f_o} correspond to the standard deviation and mean of the function f_o, respectively, within a design variable variation space for each iteration.

2.7 Definition of the probabilistic model for robust design

The probabilistic modeling of each parameter of the shunt electrical circuit, using the Maximum Entropy Method, involves obtaining the probability density function that best defines a given random variable considering the available information about it (SOIZE, 2012). This method allows the selection of a distribution with maximum uncertainty using a set of distributions that satisfy the constraints of a given random variable. According to Shannon (1948), a random variable X with a distribution $p(X)$ has an entropy measure equal to:

$$S(p(X)) = -\int p(X) \ln\left(p(X)\right) \ \mathrm{d}X \ . \tag{2.112}$$

By using the method of Lagrange multipliers, it's possible to construct a functional for the entropy of the probability density function $p(X)$. Maximizing this functional yields the expression for the most probable probability density function of the random variable:

$$p(X) = \exp\left(-1 + \sum_{i=0}^{n} \Lambda_i X^i\right) \ , \tag{2.113}$$

where Λ_i are the Lagrange multipliers obtained from the $n+1$ constraint equations of the statistical moments of the random variable X.

Considering uncertainties in the shunt circuit requires analyzing these probabilities in each circuit element, with the resistor and inductor values considered as random variables in the system. These variables have known intervals ($R, L \in]0, +\infty[$), known means ($\mathbb{E}[R] = \overline{R}$, $\mathbb{E}[L] = \overline{L}$), and finite dispersions ($\mathbb{E}[\ln(R)] = c_R \ \forall \ |c_R| < +\infty$, $\mathbb{E}[\ln(L)] = c_L \ \forall \ |c_L| < +\infty$). Solving Equation 2.113 and applying the restrictions

of the statistical moments yields the following probability functions for resistance and inductance (ZAMBOLINI-VICENTE, 2000):

$$p_{\mathrm{R}}(R) = \frac{1}{\overline{R}} \left(\frac{1}{\delta_{\mathrm{R}}^2}\right)^{\frac{1}{\delta_{\mathrm{R}}^2}} \frac{1}{\Gamma\left(\frac{1}{\delta_{\mathrm{R}}^2}\right)} \left(\frac{R}{\overline{R}}\right)^{\frac{1}{\delta_{\mathrm{R}}^2}-1} \exp\left(-\frac{R}{\delta_{\mathrm{R}}^2 \overline{R}}\right) , \tag{2.114}$$

$$p_{\mathrm{L}}(L) = \frac{1}{\overline{L}} \left(\frac{1}{\delta_{\mathrm{L}}^2}\right)^{\frac{1}{\delta_{\mathrm{L}}^2}} \frac{1}{\Gamma\left(\frac{1}{\delta_{\mathrm{L}}^2}\right)} \left(\frac{L}{\overline{L}}\right)^{\frac{1}{\delta_{\mathrm{L}}^2}-1} \exp\left(-\frac{L}{\delta_{\mathrm{L}}^2 \overline{L}}\right) , \tag{2.115}$$

where δ_{R} and δ_{L} correspond to the dispersion value of the resistive and inductive parameters, respectively, and $\Gamma(\bullet)$ is the Gamma function defined by:

$$\Gamma(X) = \int_0^{+\infty} t^{X-1} \exp(-t) \ \mathrm{d}t \ . \tag{2.116}$$

The power calculation and fatigue response functions of the model, used in the optimization process, now depend on the random values of the impedance $\boldsymbol{Z}(\omega, \theta)$ of the shunt circuit, where θ indicates a random perturbation. In this context, the Latin Hypercube Sampling (LHS) method will be employed for the dispersion levels to be investigated. Additionally, during the sample generation process, the probability density functions obtained for each random parameter characterizing the different types of shunt circuits considered in this work will be taken into account.

2.8 Metamodeling using artificial neural networks

The use of genetic algorithms to solve the Multi-objective Robust Optimization Problem (MROP) in structural dynamics is computationally expensive for obtaining solutions. The function call for each individual to define vulnerability at high dispersion levels makes it impossible to obtain results in a feasible time. Therefore, it is necessary to introduce methods to approximate functions in order to reduce these computational costs (WYSOCKI et al., 2021). Two commonly used methods for reducing processing time are metamodeling analyses using neural networks and model reduction in finite elements.

Regarding new methodologies for multidimensional estimates, neural networks represent a promising technology due to their ability to be trained and used to investigate systems involving nonlinear dynamics (MOHAMMADI-AMIN; GHADIRI, 2013).

Artificial Neural Networks (ANNs) are computational models composed of neurons, or perceptrons, which have weighted connections between them, forming an input layer, one or more hidden layers, and an output layer, as shown in Figure 2.9. Each neuron corresponds to a nonlinear activation processing of the adjacent layers. This characteristic allows the use of ANNs as an approximation of complex functions (DADRAS ESLAMLOU; HUANG, 2022).

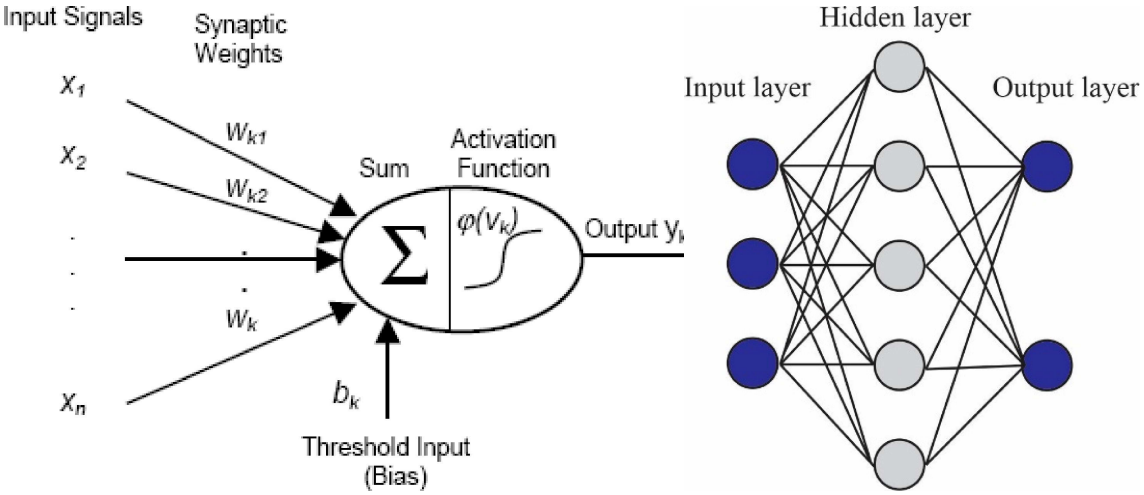

(a) Components of a neuron. (b) Neural network with a hidden layer.

Figure 2.9: Representative scheme of an Artificial Neural Network (MOHAMMADI-AMIN; GHADIRI, 2013; DADRAS ESLAMLOU; HUANG, 2022).

For training and adjusting the weights of a neural network, the backpropagation method is used, where values of previously calculated solutions are used along with optimization algorithms to make these adjustments. The goal of the optimizations is to reduce the difference between the intended value Y and the calculated value $\hat{Y}$ (SAJEDI; LIANG, 2019). Among the various measures of mean difference ϵ_m, the minimum squared error is widely used and is calculated by:

$$\epsilon_m = MSE = \frac{1}{n}\sum_{i=1}^{n}\left\|Y_i - \hat{Y}_i\right\|^2 . \tag{2.117}$$

During an epoch, pre-calculated samples are divided into training and testing sets. The training samples are used in the optimization backpropagation process of the weights. After these samples pass through, the error is calculated using the testing sam-

ples, which then defines the performance of that epoch. Various criteria can be used to define the number of epochs, with the main ones being designer-defined and the early stopping criterion, which ends training once a minimum average error is reached. Another concern during training is overfitting, when the network loses its ability to generalize to new data. Regularization techniques, data augmentation, and cross-validation can be employed to limit the model's complexity and improve the overall performance of the neural network.

Chapter III

Numerical model verification

For verification of the implemented numerical model, according to the theory mentioned, arbitrary data from a plate structure were used in two main cases: single-layer and multilayer with the insertion of piezoelectric material. Within the single-layer case, the use of two types of materials was compared: isotropic and orthotropic. In the multilayer case, only isotropic and piezoelectric materials were used.

In this, arbitrary data from a plate structure were used for comparison between modal analysis and the analysis of the Frequency Response Function (FRF) and the Power Spectral Density (PSD). The comparisons for validation consider the implementation done in this work, the commercial software ANSYS, and a code developed by the laboratory considering the Classical Laminate Theory (CLT).

In the modal analysis, the following cases were compared:

1. Comparison between code, ANSYS and classical theory - Without piezoelectric layer
2. Comparison between the code and ANSYS - With piezoelectric layer

In the harmonic analysis, the following cases were considered:

1. Comparison between code and classical theory - No damping
2. Comparison between the code and classical theory - With damping

3.1 Structure data

The structure chosen for validation consists of a plate with dimensions $l_x = 0.3\ m$ and $l_y = 0.2\ m$ and a thickness of $0.8\ mm$. In the multilayer analysis, the thickness of the piezoelectric material layer is $0.3\ mm$. As a boundary condition, the two shorter side edges were clamped. The chosen mesh has dimensions of 10×10, that is, nine divisions in each direction, totaling 100 elements. Figure 3.1 shows the geometric characteristics of the structure and the boundary conditions.

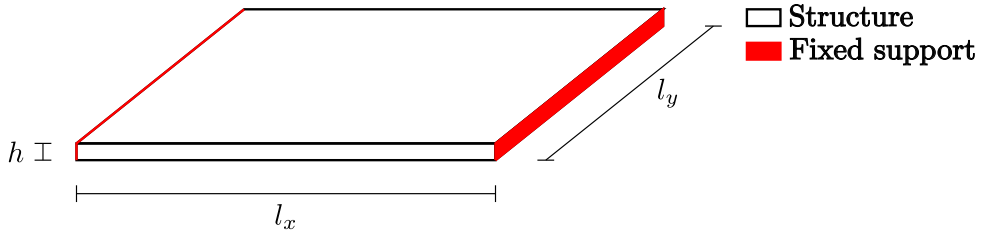

Figure 3.1: Proposed structure for analyzing model validation.

For the harmonic analysis, a frequency band of $[0, 300]$ Hz with 1500 points was considered, and Rayleigh damping parameters equal to $\alpha = 0$ and $\beta = 5 \times 10^{-5}$ (ROSA; LIMA, 2015). These parameters multiply the mass and stiffness matrices, respectively, to obtain the proportional damping matrix.

3.1.1 Material data

According to Reddy (1997), the relationship between strain and stress in the FSDT theory for isotropic materials is given by Eq. 3.1, or alternatively in the matrix form described by:

$$\boldsymbol{\varepsilon} = \boldsymbol{S}\boldsymbol{\sigma}\ , \tag{3.1}$$

$$\begin{Bmatrix} \varepsilon_{xx} \\ \varepsilon_{yy} \\ \varepsilon_{yz} \\ \varepsilon_{xz} \\ \varepsilon_{xy} \end{Bmatrix} = \begin{bmatrix} \frac{1}{E} & -\frac{\nu}{E} & 0 & 0 & 0 \\ -\frac{\nu}{E} & \frac{1}{E} & 0 & 0 & 0 \\ 0 & 0 & \frac{1}{G} & 0 & 0 \\ 0 & 0 & 0 & \frac{1}{G} & 0 \\ 0 & 0 & 0 & 0 & \frac{1}{G} \end{bmatrix} \begin{Bmatrix} \sigma_{xx} \\ \sigma_{yy} \\ \sigma_{yz} \\ \sigma_{xz} \\ \sigma_{xy} \end{Bmatrix} . \tag{3.2}$$

By calculating the inverse of the matrix $\boldsymbol{S}$, it is possible to obtain the material property matrix $\boldsymbol{C}$, which depends only on the elastic moduli and the Poisson's ratio. Thus, it results in:

$$\boldsymbol{S}^{-1} = \boldsymbol{C} = \begin{bmatrix} -\frac{E}{v^2-1} & \frac{Ev}{v^2-1} & 0 & 0 & 0 \\ \frac{Ev}{v^2-1} & -\frac{E}{v^2-1} & 0 & 0 & 0 \\ 0 & 0 & G & 0 & 0 \\ 0 & 0 & 0 & G & 0 \\ 0 & 0 & 0 & 0 & G \end{bmatrix} . \tag{3.3}$$

The shear modulus G is calculated as a function of E and ν, according to:

$$G = \frac{E}{2(1+\nu)} . \tag{3.4}$$

The shear correction coefficient used in the FSDT model follows:

$$E = \begin{bmatrix} kGh & 0 \\ 0 & kGh \end{bmatrix} , \tag{3.5}$$

where $k = 5/6$ and h corresponds to the layer thickness. Thus, for Aluminum, chosen material for the structure, and PZT G1195 for the piezoelectric material, the mechanical characteristics are described in Tab. 3.1.

Property	Aluminum	PZT G1195
Elastic Modulus - E (MPa)	70	63
Poisson's ratio - ν	0.33	0.3
Density - ρ (kg/m^3)	2700	7700

Table 3.1: Physical properties of materials.

In the ANSYS software, the SHELL281 element type was used, which considers the FSDT theory of plates with 8 nodes per element and 5 degrees of freedom per node, totaling 40 degrees of freedom per element.

3.1.2 Mesh Convergence

A mesh convergence analysis was conducted with the first three natural frequencies, starting from a division of elements 3×3 and increasing one element in each direction per iteration, as shown in Fig. 3.2. It can be observed that, from the 10×10 mesh, the values stabilize, with no frequency changes in subsequent iterations. Considering that the processing time follows an exponential regression of value $t(n) = 3 \times 10^{-6} n^{6.9129}$, with n being the number of mesh divisions, it is not computationally feasible to choose a very refined mesh for this type of problem. It was decided to use a mesh with 12×12 elements in the present work.

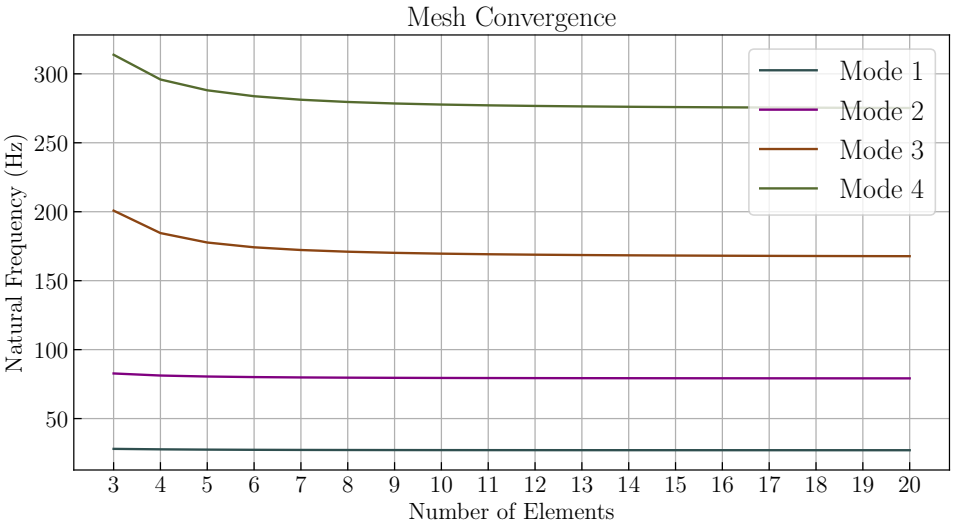

Figure 3.2: Results of the first four Natural Frequencies according to the number of divisions.

3.1.3 Modal Analysis

For the comparison of modal analysis, only the first 5 vibration modes of the structure were used. The results of the two analyses are described in Table 3.2. The piezoelectric material layer does not have electromechanical coupling at this stage of the verification of the code developed in the Python programming language. Only the mechanical implementation of the two materials was validated in these results.

For better visualization of the results, the same results are presented graphically in Figure 3.3. It can be observed that the values, although not exact, have satisfactory

	Without PZT layer			With PZT layer	
Mode	Code	ANSYS	Classic	Code	ANSYS
1	49.69	48.99	48.61	54.31	52.95
2	68.29	67.35	67.09	74.64	73.42
3	140.72	135.50	134.41	143.70	146.26
4	158.69	162.64	154.17	153.75	169.84
5	168.07	247.13	161.68	183.44	176.69

Table 3.2: Natural frequencies (Hz) for the first 5 modes of vibration.

proximity, allowing verification of the mechanical part of the model implementation. The differences observed between the results, especially between the code proposed in this work and ANSYS, are due to the different theories of multilayer plates used by the latter.

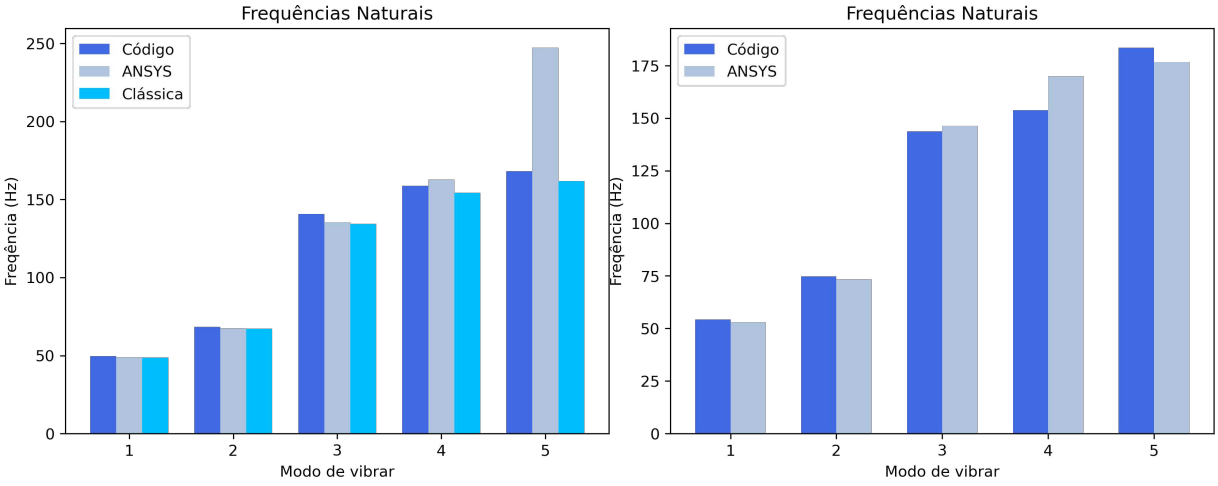

(a) (b)

Figure 3.3: Natural frequencies (a) Without PZT layer (b) With PZT layer.

The vibration modes and modal displacements are illustrated in Fig. 3.4, according to the results from the ANSYS software.

3.1.4 Harmonic response analysis

To obtain the Frequency Response Functions (FRFs) for comparison purposes, a unit force was applied at the central node of the plate in the direction of the z axis, and

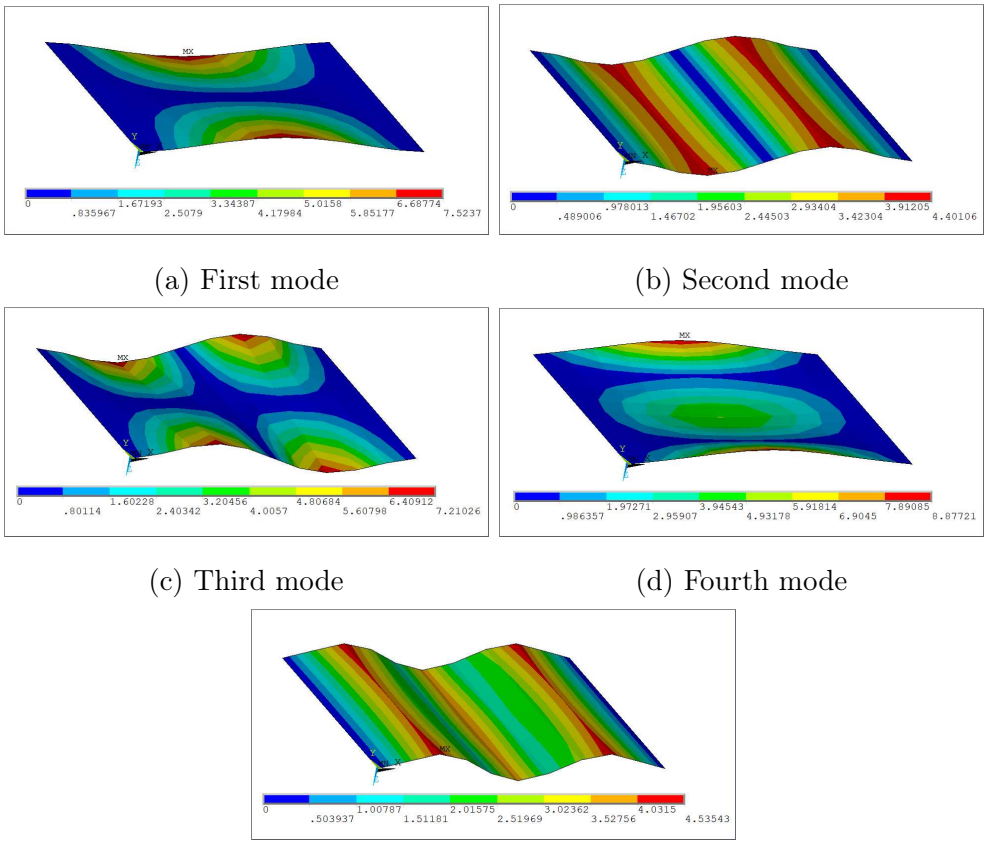

(a) First mode (b) Second mode

(c) Third mode (d) Fourth mode

(e) Fifth mode

Figure 3.4: Modal displacements by vibration mode.

the responses were obtained at the same point. The results, both for the case without damping and for the case with damping, are presented in Fig. 3.5.

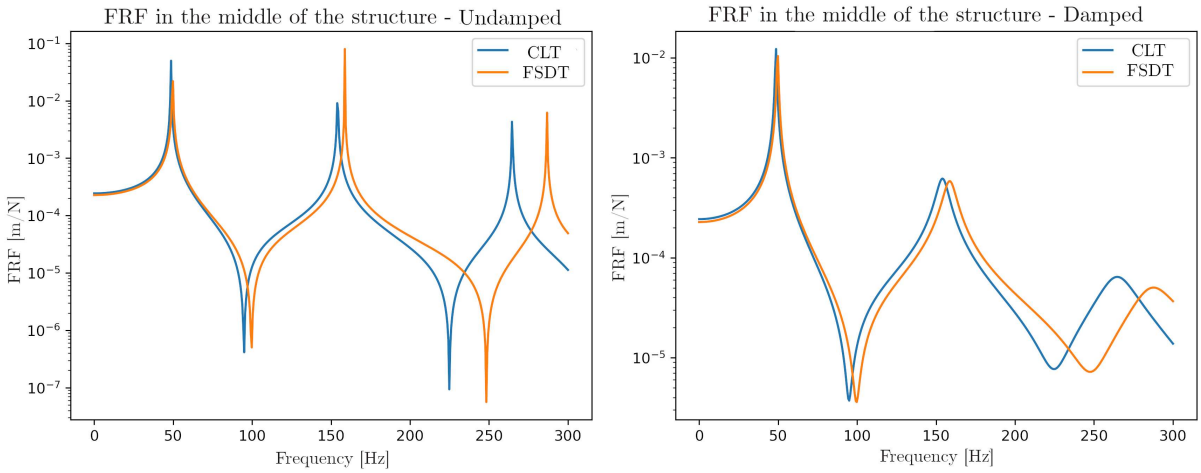

(a) (b)

Figure 3.5: FRFs (a) Undamped system (b) Damped system

Through the analysis of the amplitudes of the FRFs for both investigated cases, a good correlation between the models can be noticed. However, there is a degradation in the correlation between resonances as the frequency increases. This can be explained by the difference in the theories employed by both models. In the implemented theory (FSDT), there is a correction for transverse shear, which achieves a good approximation as the thickness increases. On the other hand, in the classical theory (CLT), the effects of transverse shear deformations and transverse normal deformation are neglected.

3.2 Analysis of electromechanical coupling in the frequency domain

According to Moheimani and Fleming (2006), the resonant shunt circuit behaves analogously to a Dynamic Vibration Absorber, in which a relatively small second-order system is attached to the dynamics of the global system. This behavior is of interest for fatigue analysis in structures. The electromechanical data of the piezoelectric patch are described in the following table:

Property	PZT G1195
χ_{11}, χ_{22}, χ_{33} - (F/m)	1.5930e-08
e_{15}, e_{24} - (C/m^2)	0.00
e_{31} - (C/m^2)	-18.30
e_{32}, e_{33} - (C/m^2)	-9.01

Table 3.3: Electrical properties of piezoelectric patch.

3.2.1 Modal analysis with electromechanical coupling

Table 3.4 shows the results obtained from the electromechanical system for two scenarios: open circuit and closed circuit.

The difference in the values found corresponds to what is expected for this type of analysis. According to Erturk (2011), with the short circuit, there is no admittance between the poles of the piezoelectric ceramic ($Y(\omega) \rightarrow 0$), indicating that the structure

Mode	Open Circuit	Short Circuit
1	54.3171	54.3088
2	74.6393	74.6393
3	144.8559	143.7032
4	153.7479	153.7479
5	183.4365	183.4365

Table 3.4: Natural frequencies (Hz) for electromechanical coupling.

will have only the mechanical properties acting on the stiffness of the system. For the open circuit case, as there is no connection between the poles, the admittance is considered infinite ($Y(\omega) \rightarrow \infty$), increasing the overall stiffness of the system and consequently the natural frequencies.

3.2.2 Frequency response with shunt circuit

Using different configurations of the resonant shunt circuit, it is possible to obtain variations in the frequency response function graphs, according to Figs. 3.6 and 3.7. For comparative purposes and to understand the influence of the variation of values on the results, two cases were considered: first with constant inductance and variation in resistance, then varying the inductance and keeping the resistance constant.

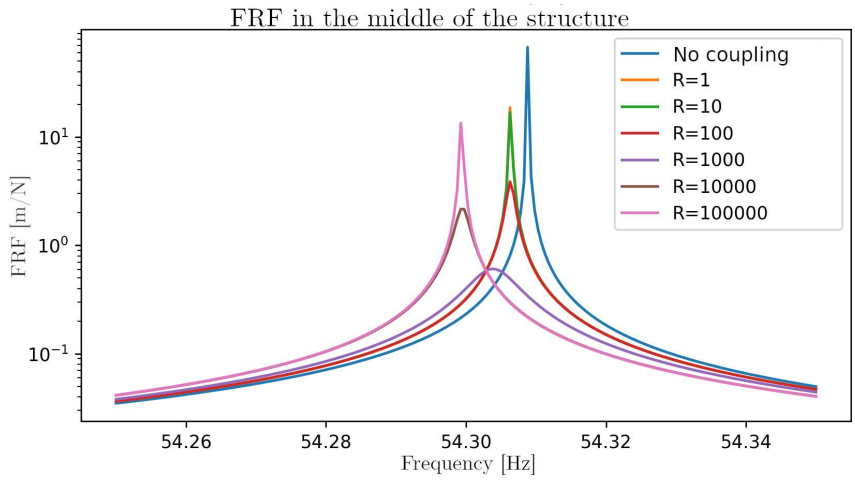

Figure 3.6: Variation in shunt circuit resistance - FRF First mode.

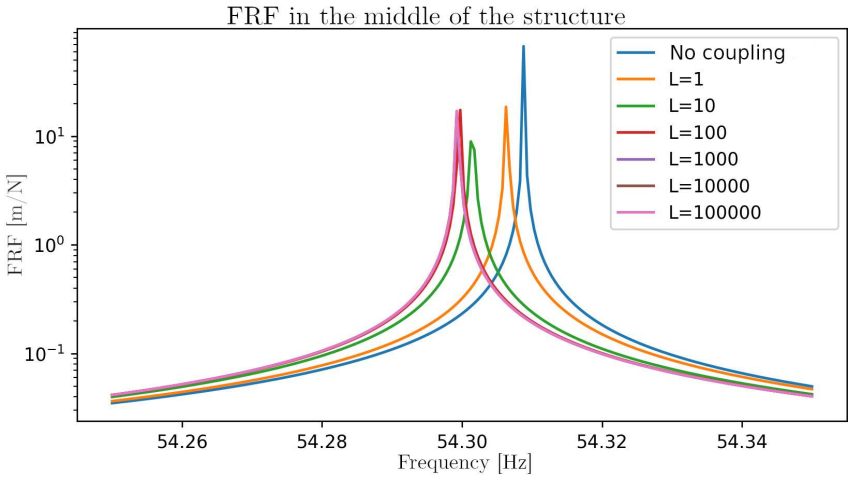

Figure 3.7: Variation of shunt circuit inductance - FRF First mode.

In the first case, it is noticeable that there is a change in the resonance peak value, indicating an attenuation in the displacement of the structure at the studied point. It is also noticeable that there is a limit value of resistance that corresponds to the highest possible attenuation for the structural conditions. In the second case, it is evident that there is no attenuation in the peak value, but there is a translation of the peak, indicating a variation in the structure's frequency.

3.2.3 Power spectral density with shunt circuit

The voltage responses of the previous shunt circuit configurations were also obtained, as described in the literature review. The spectral loading considered was white noise with intensity $\phi_f = 85 \times 10^3$ Pa^2/Hz, for the entire frequency band analyzed. The system response tensor has 3 principal values for stress analysis in the plane stress state: axial stress in the x and y directions, and shear stress xy. By considering constant impedance and varying resistance values, it is possible to compare the results for each stress according to Figs. 3.8, 3.9, and 3.10.

A curious fact in this application is that since the chosen loading has constant excitation across frequency, the attenuation generated by the shunt circuit in the PSD has the same characteristics as the attenuation in the FRF.

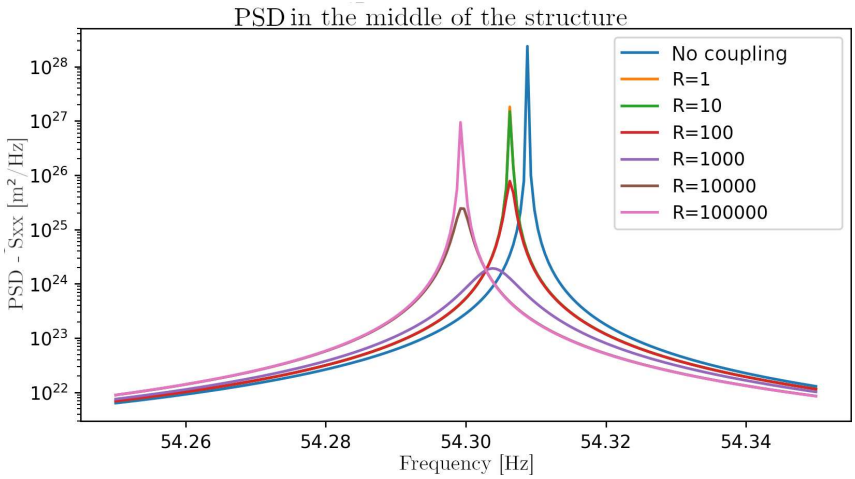

Figure 3.8: PSD First mode (σ_{xx}).

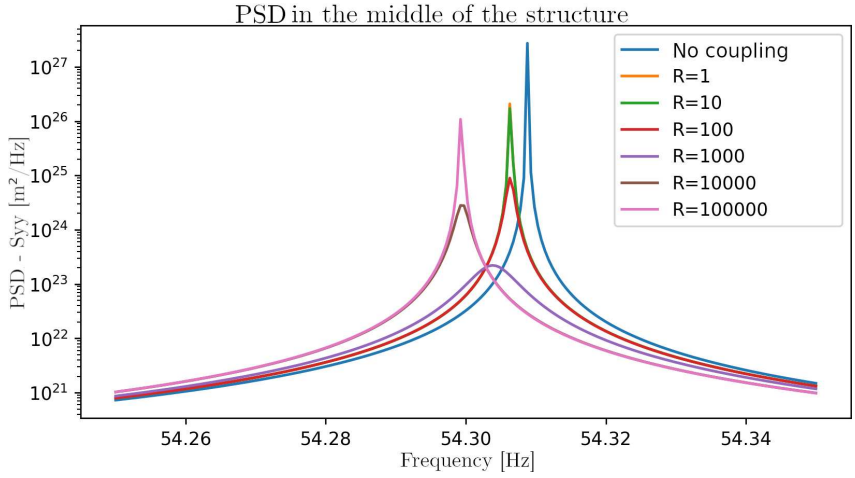

Figure 3.9: PSD First mode (σ_{yy}).

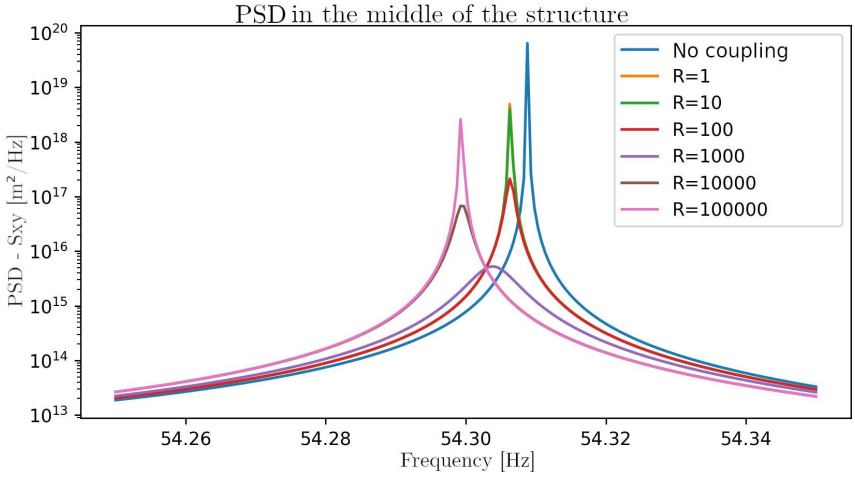

Figure 3.10: PSD First mode (σ_{xy}).

3.3 Neural network training

In order to reduce the calculation time of the objective functions, a neural network metamodel was defined where the design variables correspond to the inputs, and the expected objectives correspond to the outputs. Thus, among all the optimization cases studied in this work, the possible design variables are the elements of the shunt circuit (resistance R and inductance L) and the elements of the FEM model that have a piezoelectric layer, i.e., each element of the structure corresponds to a binary input indicating the presence or absence of this element. As for the two output values, the fatigue indicator $\mathbb{E}[D_{\text{sines}}]$ and the collected power indicator Υ were considered. Based on analyses performed with the problem, the chosen neural network architecture corresponds to:

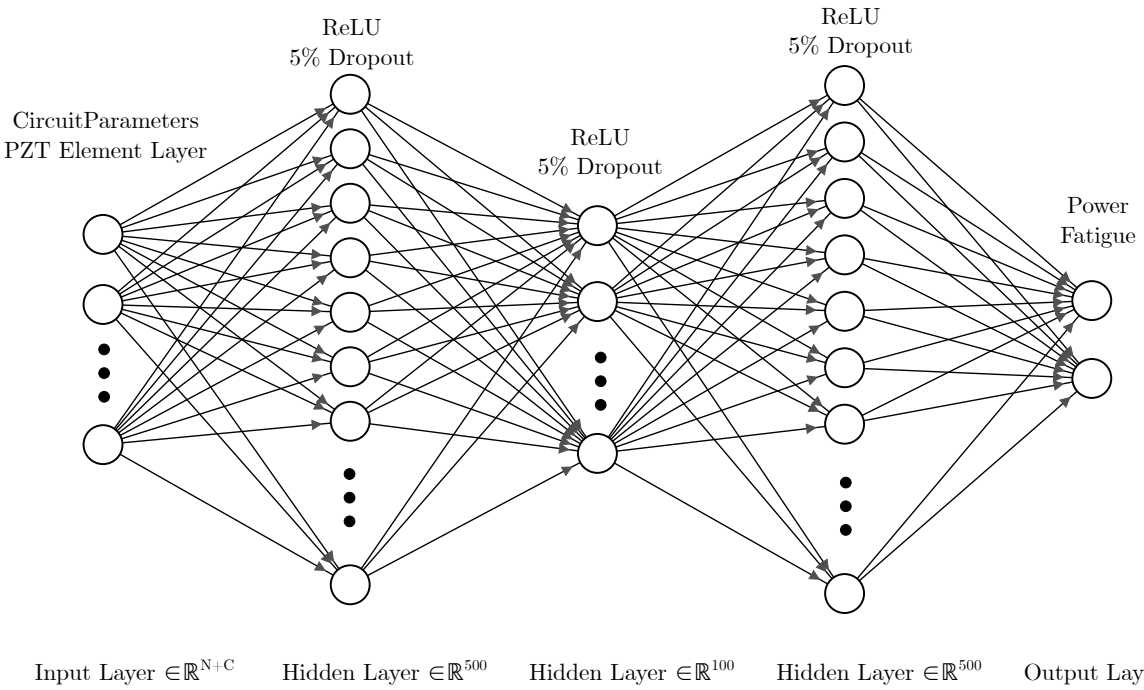

Figure 3.11: The architecture of the neural network used, with N equal to the number of elements, and C equal to the number of circuit parameters.

It can be noticed that the hidden layers have Rectified Linear Unit (ReLU) activation function. In addition, a dropout rate, which consists of not utilizing a percentage of connections between neurons during training, was inserted in each layer in order to reduce overfitting effects. Finally, an L2 regularizer, also known as Ridge regression, was

added to the hidden layers to add a quadratic magnitude of the coefficients as a penalty term to the loss function.

For the generation of the data used in training the network, a search space was defined for the design variables of $R = [10^1, 10^5]$ and $L = [10^{-1}, 10^2]$, following other works in the same area and commercially available values. For the input elements, the density $d_i \in \{0, 1\}$ corresponds to the boolean value of the presence of a PZT layer in element i. A parametric routine was created to generate the data, using pseudo-random values from a normal distribution within the space of each variable.

Finally, the chosen weight optimization algorithm was Nadam, which corresponds to an adaptation of the Adam algorithm (Adaptive Moment Estimation) with incorporated Nesterov momentum concepts. A separation rate of 80% and 20% in the training and testing data over 50 epochs, respectively. Additionally, an early stopping criterion was defined, which monitors the loss function value of the testing data, interrupting the routine if these values indicate overfitting.

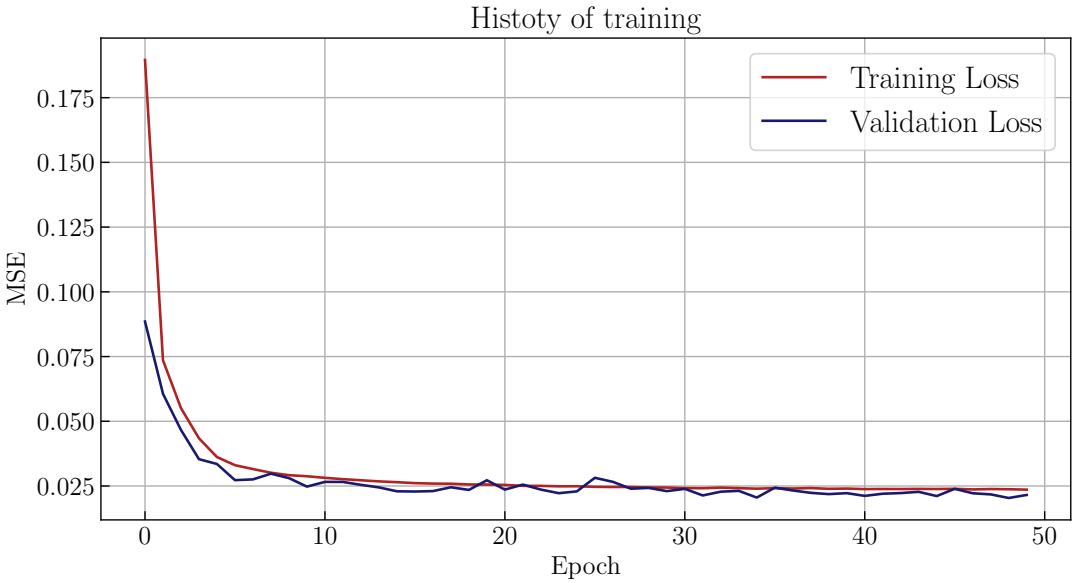

Figure 3.12: History of resistive circuit training.

After generating a dataset of 166 thousand pre-calculated results, the training history of the neural network for the parallel resistive and resonant circuit in Figs. 3.12 and 3.13 respectively, resulted in an MSE of 0.02 and 0.04, respectively. Using 20% of the dataset for model verification, results taken randomly and not used in the training of the network, it is possible to obtain the regression result of the real values and predicted

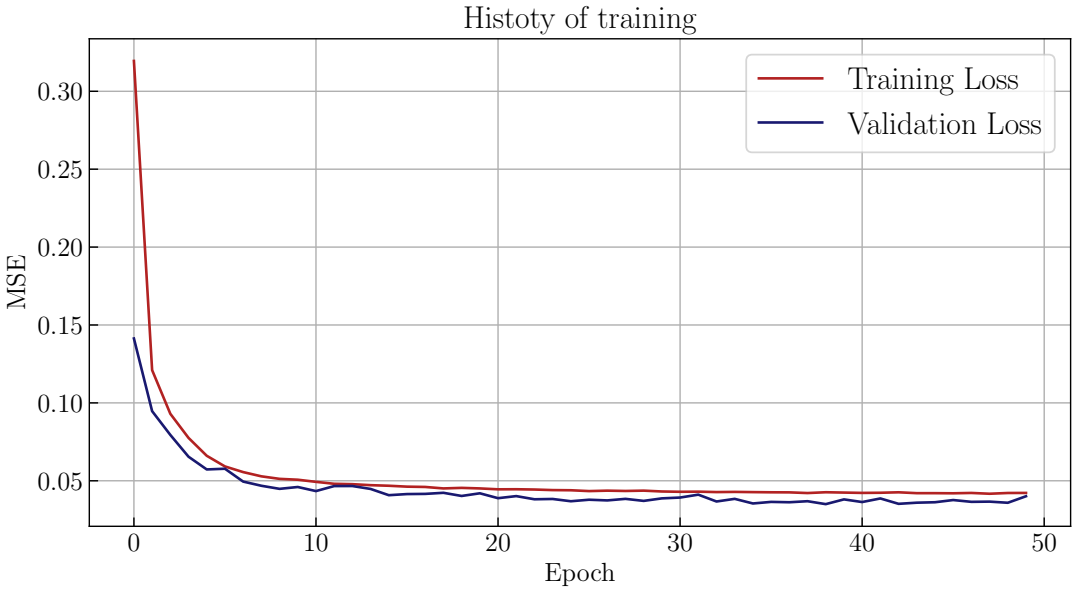

Figure 3.13: Resonant circuit training history.

values. Figures 3.14 and 3.15 correspond to the results of both objectives for the resistive and resonant circuit, respectively.

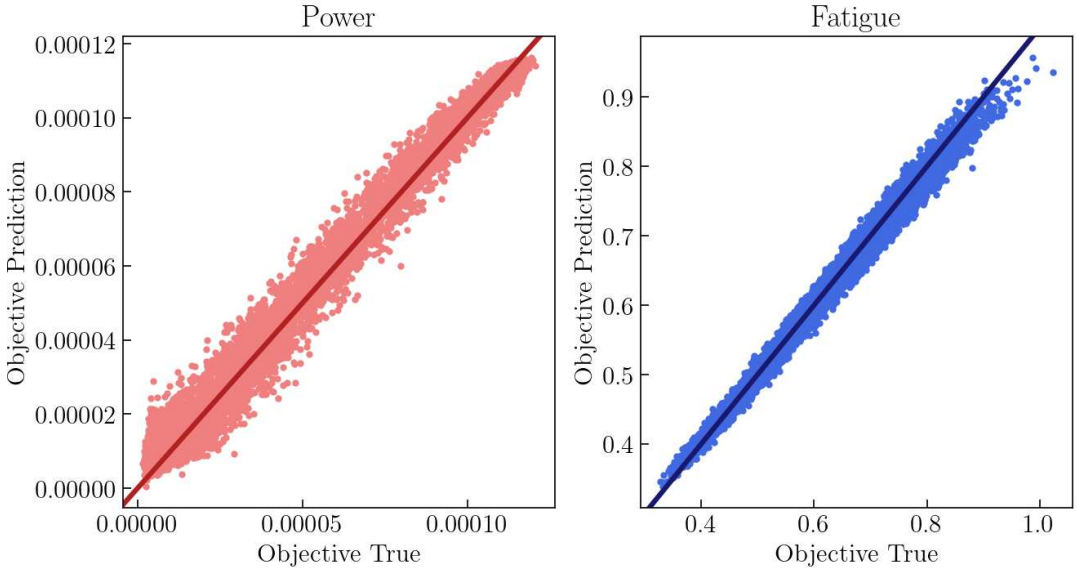

Figure 3.14: Regression result of the resistive circuit model.

By training the neural network, the model can be directly used for evaluating the objective functions. Another major advantage of using the metamodel is the use of tensors to represent input and output data, which make predictions with almost no computational overhead. This allows for the insertion of robustness calculation based on

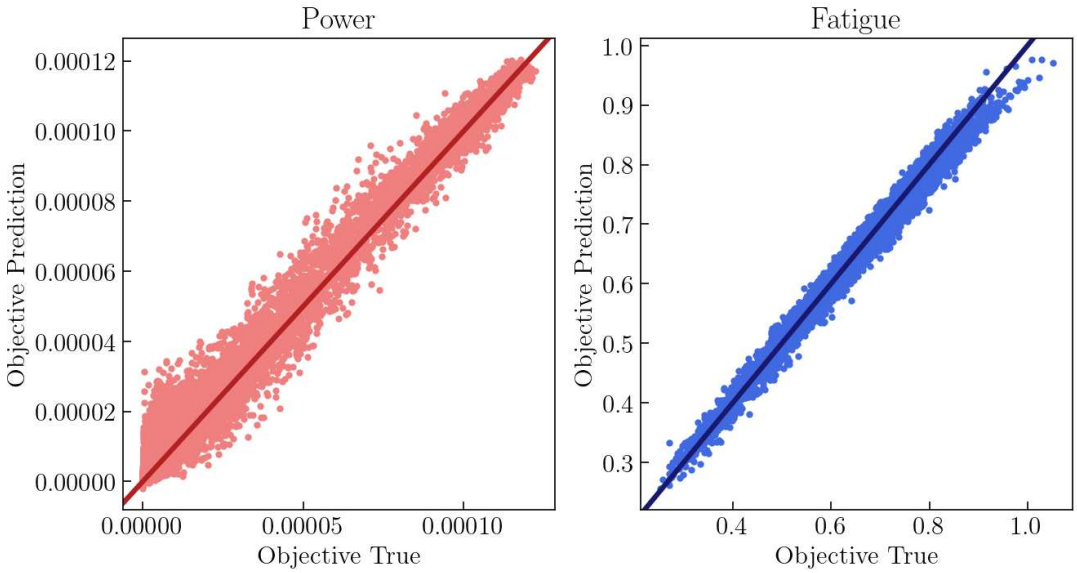

Figure 3.15: Resonant circuit model regression result.

the mean and standard deviation, without significantly increasing processing time.

Chapter IV

Shunt circuit optimization

In this chapter, the optimization process will focus on optimizing the elements of the shunt circuit, and the influence that the optimization results have on fatigue levels and the amount of harvested energy.

4.1 Monoaxial fatigue life gain

For the monoaxial fatigue life analysis, an analytical model was considered for the vibrations of a cantilever beam under transversal base excitation. This model is widely used in energy harvesting analyses, where the goal is to extract vibration from the system in the form of electrical energy through a coupled electrical circuit. In this regard, a bimorph beam (metallic substructure covered with layers of piezoceramic), as shown in Fig. 4.1, harmonically excited at the base and with a mass at the tip (M_t), was modeled (ERTURK, 2011).

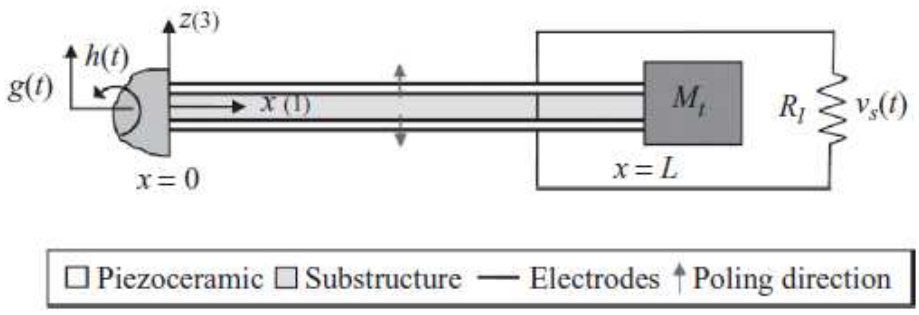

Figure 4.1: Schematic diagram of vibration control with shunt circuit.

The Fig. 4.1 depicts the oscillatory base in translation $g(t)$ and rotation $(h(t))$. However, all analyses conducted neglect the excitation by rotation. Additionally, some assumptions of the model are: Euler-Bernoulli beam model with piezoelectric coupling; coupled electromechanical equations for beams oscillating transversely; linear elastic deformations; internal and external damping mechanisms; perfect bonding between the substructure and the piezoceramics; continuous and ideal piezoelectric electrode with negligible thickness; polarization in the direction 3 of the piezoceramics; and the induced electric field is uniform along the length of the beam.

Given the assumed hypotheses and the constitutive relations of piezoelectricity, it is possible to write the equation governing the forced vibration of the system described in(ERTURK, 2011):

$$\begin{aligned} &YI\frac{\partial^4 w(x,t)}{\partial x^4} + c_{\mathrm{s}} I\frac{\partial^5 w_{\mathrm{rel}}(x,t)}{\partial x^4 \partial t} + c_{\mathrm{a}}\frac{\partial w_{\mathrm{rel}}(x,t)}{\partial t} \\ &+ m\frac{\partial^2 w_{\mathrm{rel}}(x,t)}{\partial t^2} \vartheta v(t)\left[\frac{\mathrm{d}\delta(x)}{\mathrm{d}x} - \frac{\mathrm{d}\delta(x-L)}{\mathrm{d}x}\right] = -[m + M_{\mathrm{t}}\delta(x-L)]\frac{\partial^2 w_{\mathrm{b}}(x,t)}{\partial t^2}\ , \end{aligned} \tag{4.1}$$

where YI is the flexural rigidity under short-circuit condition, $w_{\mathrm{rel}}(x,t)$ is the transverse displacement of the beam (neutral line) relative to the base at position x and time t, c_{a} is the viscous damping coefficient of the air, c_{s} is the strain-rate damping coefficient (appears as an effective term $c_{\mathrm{s}}I$ for the composite structure), m is the mass per unit length of the beam, M_{t} is the mass at the tip, $\delta(x)$ is the Dirac delta function, ϑ is the inverse coupling coefficient (depends on whether the circuit is connected in series or parallel), and $v(t)$ is the voltage across the electrodes of each piezoceramic layer.

The displacement of the beam can be represented as a series of eigenfunctions, based on proportional damping. Solving for the relative displacement in the frequency domain, the following representation of the relative displacement is obtained:

$$w_{\mathrm{rel}}(x,t) = \sum_{r=1}^{\infty}\left[\left(F_r - \tilde{\theta}_r \frac{\displaystyle\sum_{r=1}^{\infty}\frac{j\omega\tilde{\theta}_r F_r}{\omega_r^2 - \omega^2 + j2\zeta_r\omega_r\omega}}{Y(\omega) + j\omega C_{\tilde{\mathrm{p}}}^{\mathrm{eq}} + \displaystyle\sum_{r=1}^{\infty}\frac{j\omega\tilde{\theta}_r^2}{\omega_r^2 - \omega^2 + j2\zeta_r\omega_r\omega}}\right)\frac{\phi_r(x)\mathrm{e}^{j\omega t}}{\omega_r^2 - \omega^2 + j2\zeta_r\omega_r\omega}\right], \tag{4.2}$$

where $C_{\tilde{\mathrm{p}}}^{\mathrm{eq}}$ is the equivalent capacitance, $Y(\omega)$ is the admittance of the shunt circuit. For each mode r, there is the external loading applied to the structure F_r, the electromechan-

ical coupling term $\tilde{\theta}_r$, the natural frequency ω_r, the eigenfunction ϕ_r, and the damping factor ζ_r.

Bauchau (2009) describes that, in the case of cross-sections symmetric with respect to a plane perpendicular to the neutral axis, the stress in the beam is calculated according to:

$$\sigma_{\mathrm{xx}}(x) = -\bar{y} Y_{\mathrm{s}} \frac{\mathrm{d}^2 w(x)}{\mathrm{d}x^2} \ , \tag{4.3}$$

where $\bar{y}$ is the height of the cross-section of maximum stress (maximum stress is $|\bar{y}| = \pm h/2$) and Y_s is the elastic modulus of the material.

With this, applying the known values and using the admittance as $Y = 1/R$, it is possible to obtain the Frequency Response Function (FRF) of the stress at the beam tip. This function contains information on the influence of the shunt circuit on the total displacement of the structure. As it is already known, the displacement at the tip of a cantilever beam is directly proportional to the deformation and stress present in the structure. Finding the minimum value of the peak of a specific vibration mode in the displacement FRF provides a resistance value in the shunt circuit that corresponds to minimum vibration in the structure. Therefore, this resistance results in the minimum stress at the cross-section near the base, resulting in an optimal model with less stress accumulation in the time domain. Thus, an optimization problem can be formulated using the peak of the stress FRF as the objective function to be minimized, and the resistance R as the design variable.

The characteristics defined for the structure are described in Table 4.1, where the structure is an aluminum 2024-T3 beam and the piezoelectric layer is of type PZT-4 (LIPSKI, 2016; EFUNDA, 2021).

Using eight vibration modes for superposition and solving the equation of motion, a vertical displacement of $W_0 = 25.4$ mm, an excitation frequency of $\omega = 1.5$ krad/s, and a test window of $t = 200$ s were defined, according to values available for experimental testing. Conducting an analysis in open and closed circuits, we observe in Fig. 4.2 the difference in response in an open and closed circuit, where a decrease in displacement amplitude can be observed.

Following this, optimization of the displacement FRF was performed using an

	Structure	PZT
Length (L) (mm)	100	100
Width (b) (mm)	30	30
Thickness (h_s, h_p) (mm)	1	0.3 (cada)
Thickness	Aluminum 2024-T3	PZT-4
Density (ρ_s, ρ_p) (kg/m²)	2780	7500
Elastic modulus (Y_s, $\bar{c}_{11}^E$) (GPa)	73.1	81.3
Piezoelectric Constant ($\bar{e}_{31}$) (C/m²)	—	−10
Permittivity constant ($\bar{\varepsilon}_{33}^E$) (nF/m)	—	12.74
Fatigue constant (C_f)	3.15e14	—
Fatigue exponent (m_f)	4.10	—

Table 4.1: Geometric and material values.

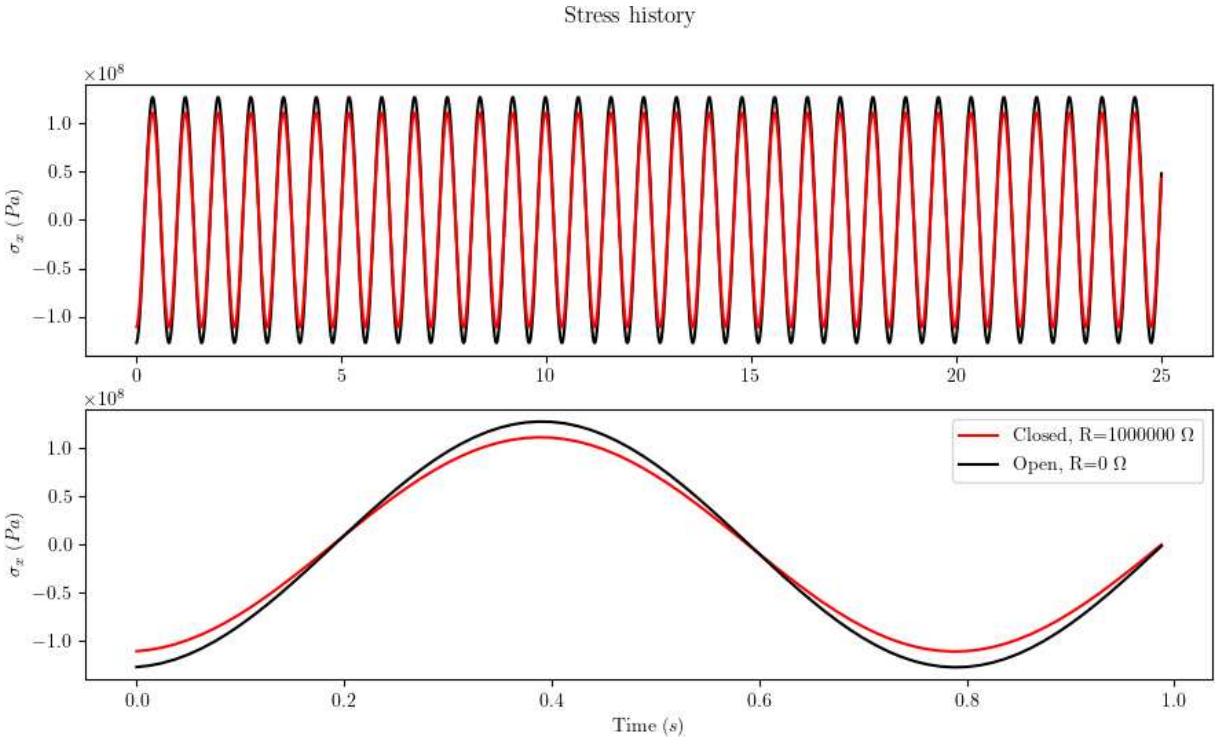

Figure 4.2: History of stress at the base of the beam (most stressed region).

NSGAII genetic algorithm. Setting up the optimization problem with 10,000 function evaluations, the algorithm calculates the optimal resistance as $R = 39633.92\ \Omega$. Figure 4.3 contains the displacement FRF at the tip of the structure over a wide range of resistances,

including the previously calculated optimal resistance. The curve of the optimal peak is clearly distinguished compared to the other values.

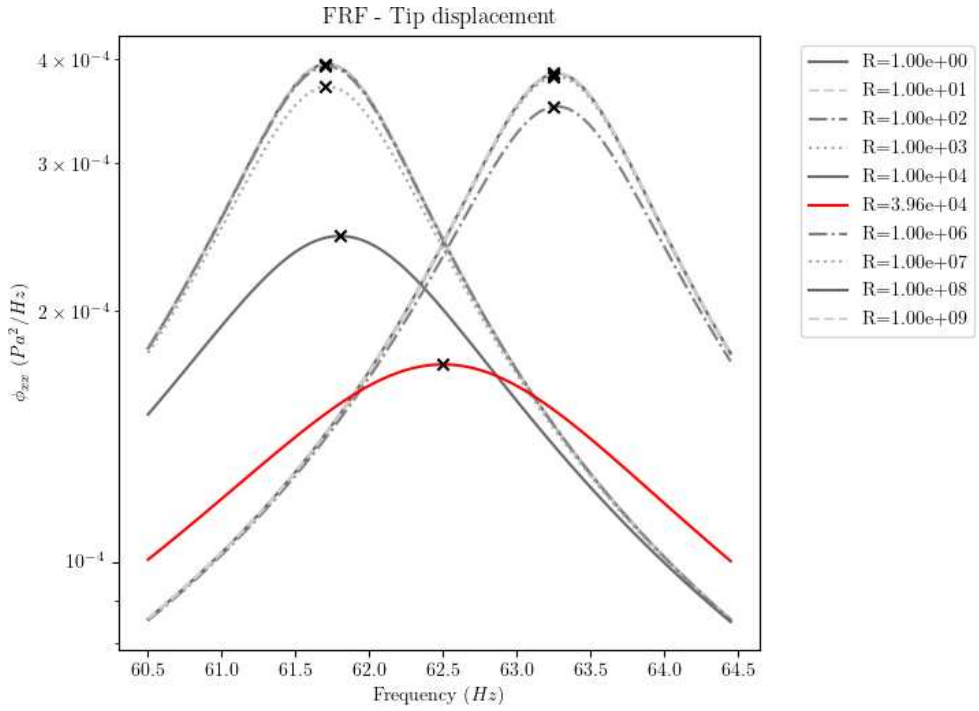

Figure 4.3: FRF of the displacement at the beam tip for various cases and the optimal case.

Using the same resistance values mentioned earlier, a fatigue analysis was performed with the rainflow cycle counting method applied to the stress history. The most stressed part of the beam is exactly at the fixed support, and the results of the analysis are shown in Fig. 4.4. The optimal resistance value consists of the highest fatigue life expectancy equal to $N_\mathrm{f} = 212.28$ h, which is inversely proportional to damage and has the lowest damage $D = 2.61714 \times 10^{-4}$.

The initial analysis with an analytical beam allows us to observe the positive and direct influence on the fatigue life of the structure. Due to the simplicity of the studied model, the optimization process is fast and can converge to optimal results in a short time, enabling its application in structural monitoring projects.

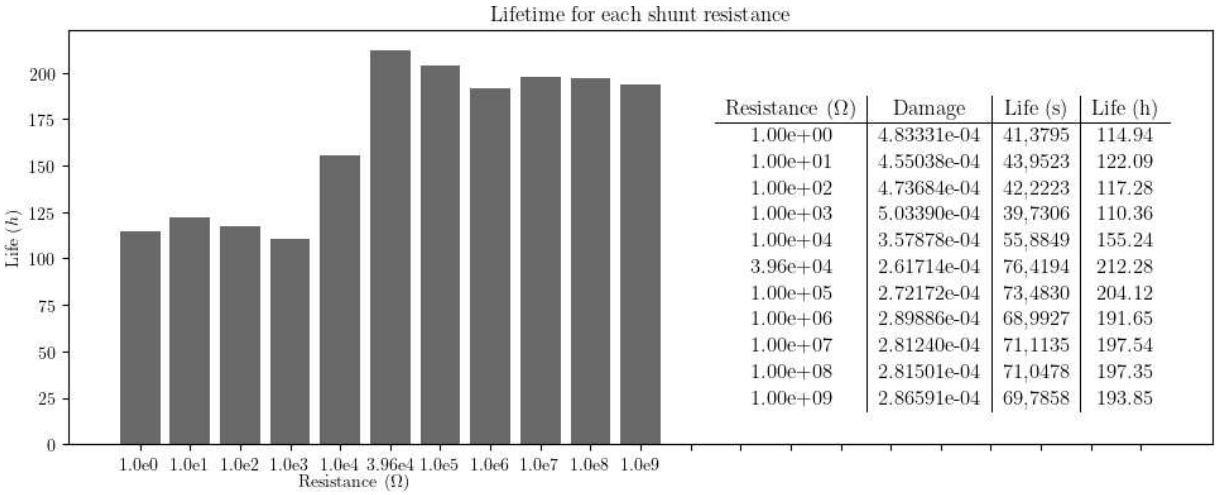

Resistance (Ω)	Damage	Life (s)	Life (h)
1.00e+00	4.83331e-04	41,3795	114.94
1.00e+01	4.55038e-04	43,9523	122.09
1.00e+02	4.73684e-04	42,2223	117.28
1.00e+03	5.03390e-04	39,7306	110.36
1.00e+04	3.57878e-04	55,8849	155.24
3.96e+04	2.61714e-04	76,4194	212.28
1.00e+05	2.72172e-04	73,4830	204.12
1.00e+06	2.89886e-04	68,9927	191.65
1.00e+07	2.81240e-04	71,1135	197.54
1.00e+08	2.81501e-04	71,0478	197.35
1.00e+09	2.86591e-04	69,7858	193.85

Figure 4.4: Bar graph of fatigue life in hours and complete results.

4.2 Multiaxial fatigue life gain

To analyze the effects of the shunt circuit on the structure with the optimal values resulting from the optimization process, an aluminum plate structure with a piezoelectric layer was selected as shown in Fig. 4.5. The finite element model consists of a mesh of 12×12 elements with a free-clamped boundary condition and an external loading with white noise of 10^3 Pa^2/Hz at the free end. This loading is used at all frequency points in the fatigue calculation. The material properties follow the data in Tab. 4.1 with an equivalent damping $\boldsymbol{C}_{\text{eq}} = 5 \times 10^{-5}\boldsymbol{K}$. The geometric data of the structure are $L_x = 140$ mm, $L_y = 110$ mm, $h_s = 0.6$ mm, and $h_p = 0.1$ mm.

The presented structure will be used in the sequential optimizations. Initially, the optimization will focus on the shunt circuit elements, considering the single objective of fatigue life, and subsequently, on the amount of collected energy. For each optimization, robustness influence was considered. This initial analysis allows quantifying the local influence of the circuit for each objective, as well as identifying the influence of robustness on the objective functions. The optimization problem takes the following form, where $\mathcal{V}_{\mathbb{E}[D_{\text{sines}}]}$ is the vulnerability function of the Sines fatigue estimate, $R \in [10^1, 10^5]$ and $L \in [10^{-2}, 10^1]$:

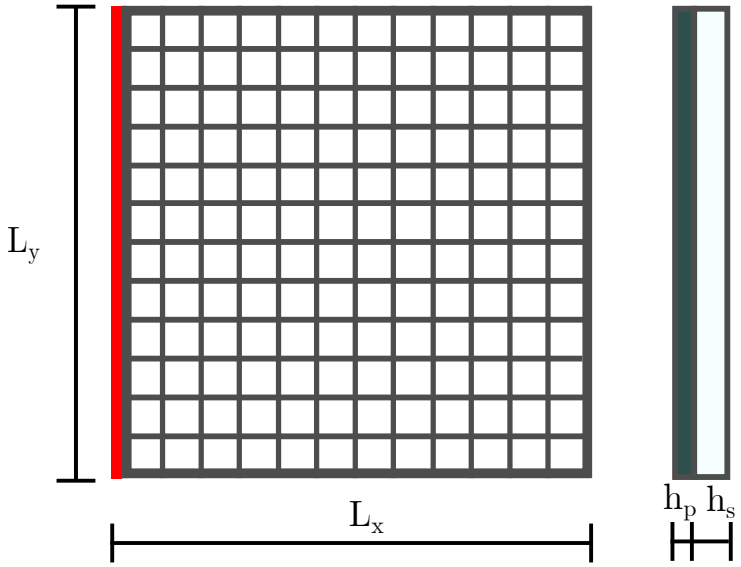

Figure 4.5: Schematic of the board structure.

$$\begin{aligned} \min_{\boldsymbol{R},\boldsymbol{L}} \quad & \boldsymbol{F}_{\mathrm{o}}^{\mathrm{R}} = \begin{bmatrix} \mathbb{E}\left[D_{\mathrm{sines}}\right] & \mathcal{V}_{\mathbb{E}[D_{\mathrm{sines}}]} \end{bmatrix}^{\mathsf{T}} \\ \text{s.t.} \quad & R_{\min} \leq \boldsymbol{R} \leq R_{\max} \\ & L_{\min} \leq \boldsymbol{L} \leq L_{\max} \end{aligned} \quad . \tag{4.4}$$

After 200 generations with a population of 100 individuals, and using a spread of 5% with 1000 trials, the following results are obtained for the resistive circuit with the population of non-dominated outcomes, disregarding the inductance portion in the optimization problem:

The curve exhibits a behavior similar to linear, indicating that the fatigue index varies linearly with the resistance variation. This characteristic can be justified by the influence of the resistive shunt circuit on the Frequency Response Functions, directly affecting the fatigue damage of the structure. In the resistive circuit curve, it is possible to clearly visualize the result with higher damage and lower variation ($R = 12.00\ \Omega$), lower damage and higher variation ($R = 21.31\ \Omega$), and compromise between the two values ($R = 16.65\ \Omega$).

In the resonant circuit, the non-dominated results are shown in Fig. 4.7.

The fatigue values in the resonant system are similar to those in the resistive circuit, also maintaining the linearity of the curve. However, the level of variability

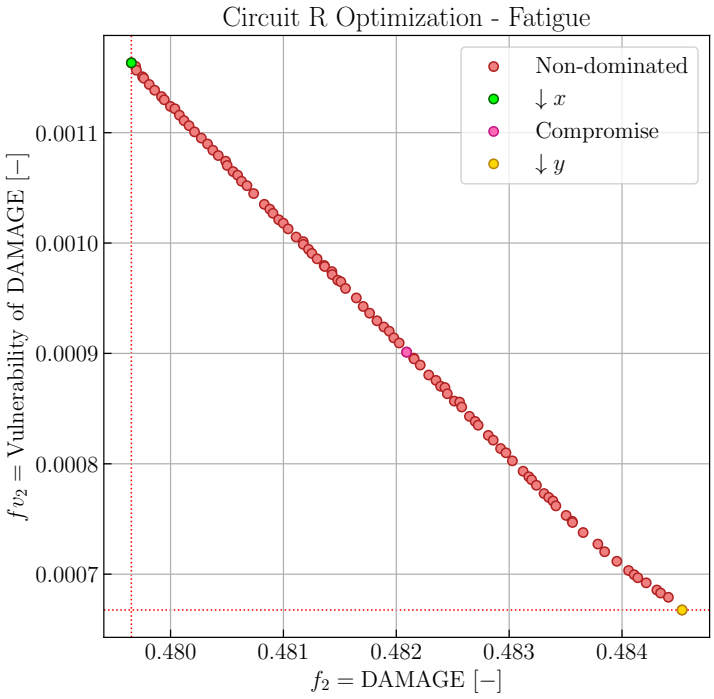

Figure 4.6: Non-dominated optimal solutions in robust fatigue analysis with resistive circuit.

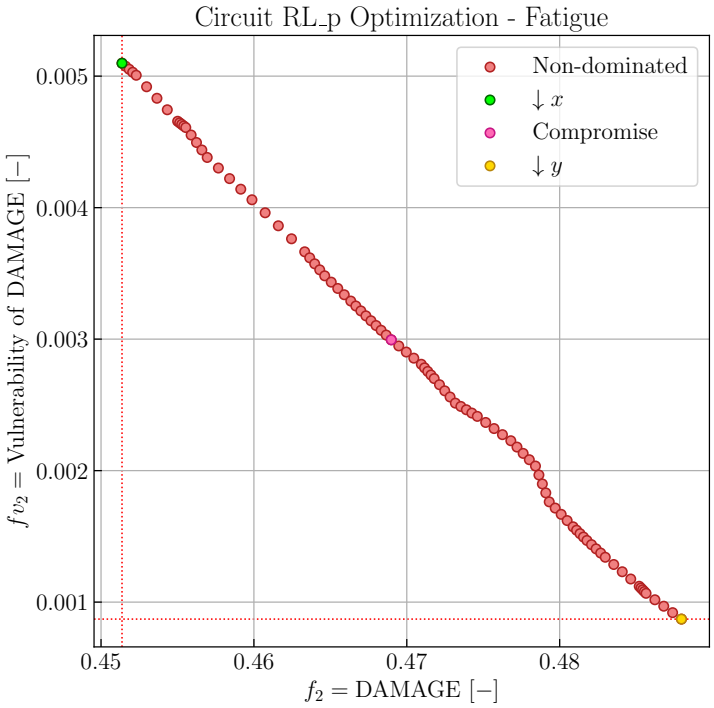

Figure 4.7: Non-dominated optimal solutions in robust fatigue analysis with resonant circuit.

appears to be lower than in the resistive circuit, resulting in a more robust system. It is possible to select the three results in the same way, with higher damage and lower variation ($R = 7.77$ kΩ, $L = 9.99$ H), lower damage and higher variation ($R = 81.51$ kΩ, $L = 9.99$ H), and compromise between the two values ($R = 80.18$ kΩ, $L = 9.99$ H). It is noticeable that, in this analysis, the inductance values tend to approach the maximum limits of the optimization problem.

4.3 Enhanced harvested energy

In the energy harvesting analysis, the optimization problem takes the following general form, with the same limiting values for the variables:

$$\begin{aligned} \min_{\boldsymbol{R},\boldsymbol{L}} \quad & \boldsymbol{F}_{\mathrm{o}}^{\mathrm{R}} = \begin{bmatrix} -\Upsilon & \mathcal{V}_{\Upsilon} \end{bmatrix}^{\mathsf{T}} \\ \text{s.t.} \quad & R_{\min} \leq \boldsymbol{R} \leq R_{\max} \\ & L_{\min} \leq \boldsymbol{L} \leq L_{\max} \end{aligned} \cdot \tag{4.5}$$

The inversion of sign in the power values was used, as the analysis's interest is to obtain maximum power results. The same parameters were used for energy harvesting analysis. For the resistive circuit, without considering the inductance portion in the optimization, the following Pareto curve is obtained:

In the case of energy, besides the mirrored curvature (maximization problem), the curve does not exhibit a linear characteristic due to the inclusion of complex terms in the power calculation. The variability values have a wide range compared to the results of the resonant circuit. Considering the three points of interest, we have the following: for minimum power and minimum variability ($R = 250.54\ \Omega$), maximum power and maximum variability ($R = 230.39\ \Omega$), and a compromise between the results ($R = 238.76\ \Omega$).

In the resonant circuit there is the following Pareto curve:

It's possible to visualize the same curve shape, but with less significant results and variability within a smaller range. Nevertheless, the results do not surpass those of the resistive circuit. The points of interest are for minimum power and minimum variability

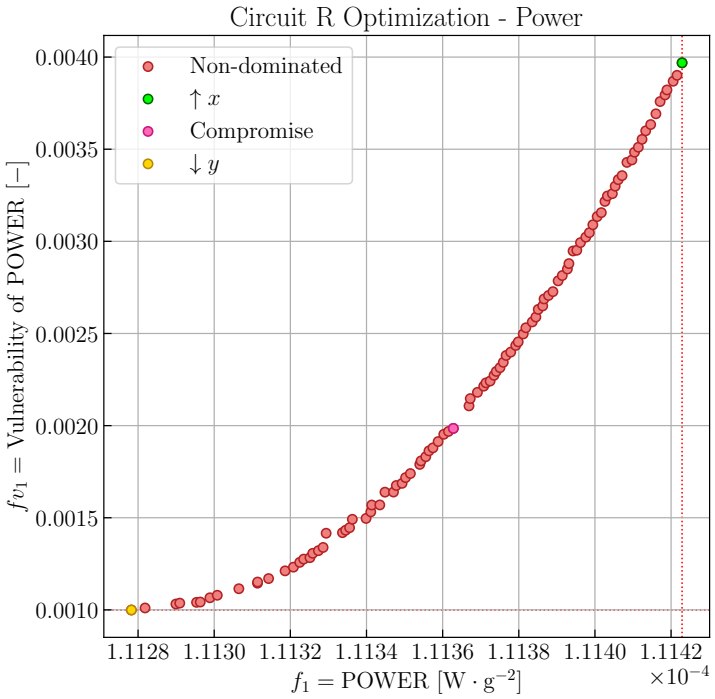

Figure 4.8: Non-dominated optimal solutions in robust power analysis with resistive circuit.

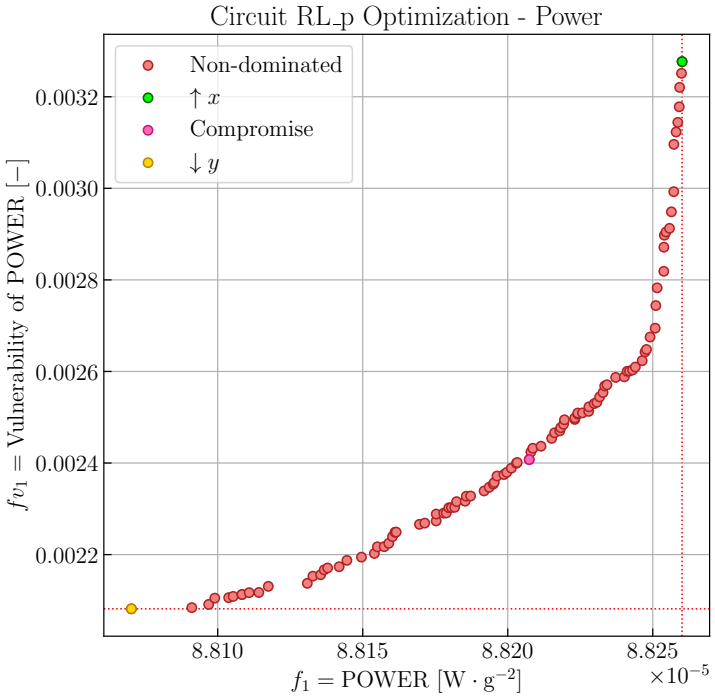

Figure 4.9: Non-dominated optimal solutions in robust power analysis with resonant circuit.

($R = 397.24\ \Omega$, $L = 5.06$ H), maximum power and maximum variability ($R = 410.04\ \Omega$, $L = 4.29$ H), and a compromise between the results ($R = 407.09\ \Omega$, $L = 4.67$ H).

4.4 Compromise between harvested power and dynamic fatigue

From the latest examples, it's possible to conclude that the values of the shunt circuit parameters have a direct influence on vibration control and fatigue gain, as well as in the case of vibration energy harvesting. Despite being counterintuitive, the idea of optimizing a shunt circuit to meet both needs is intriguing. To verify this possibility, a manual sweep of resistance values was performed on a plate structure, resulting in the normalized values shown in Fig. 4.10.

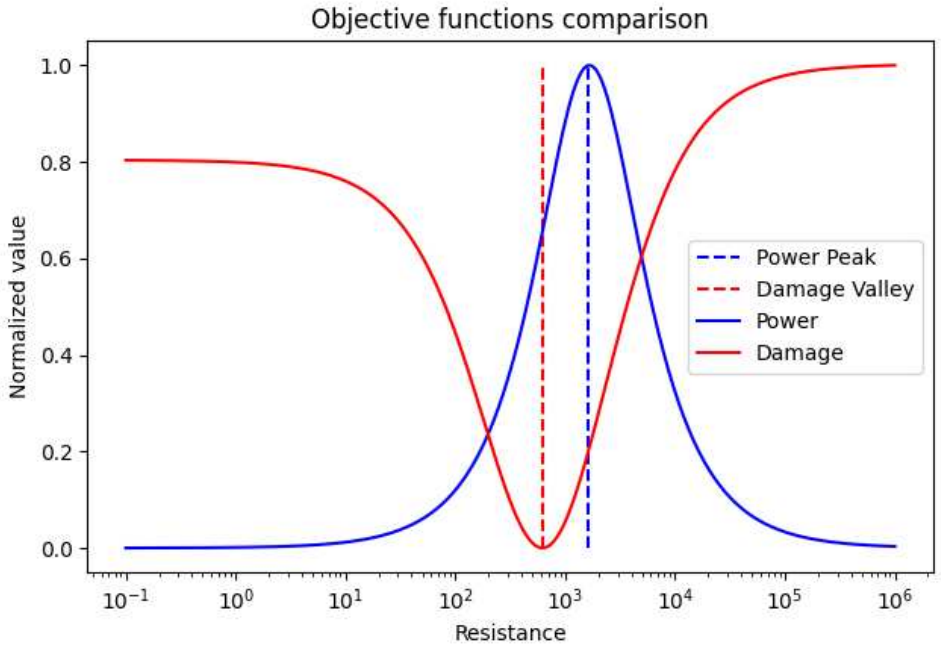

Figure 4.10: Analysis of normalized fatigue and energy collection values.

It's noticeable that as we increase the resistance values, both curves reach peak values, eventually returning to a baseline value. Observing the maximum and minimum values, there's a range of resistance between maximum energy and the minimum fatigue value. This range indicates the possibility of defining a multi-objective compromise with non-dominated values in a Pareto curve, allowing the designer to choose the best result

that suits their application.

The robust optimization problem presented earlier is related, incorporating the collection power and damage expectancy as objective functions, along with their respective variabilities, as shown in:

$$\begin{aligned} \min_{\boldsymbol{R},\boldsymbol{L}} \quad & \boldsymbol{F}_{\mathrm{o}}^{\mathrm{R}} = \begin{bmatrix} -\Upsilon & \mathcal{V}_{\Upsilon} & \mathbb{E}\left[D_{\mathrm{sines}}\right] & \mathcal{V}_{\mathbb{E}[D_{\mathrm{sines}}]} \end{bmatrix}^{\mathsf{T}} \\ \text{s.t.} \quad & R_{\min} \leq \boldsymbol{R} \leq R_{\max} \\ & L_{\min} \leq \boldsymbol{L} \leq L_{\max} \end{aligned} \quad . \tag{4.6}$$

The same parameters were used to solve the optimization problem in the resistive circuit. Due to the additional dimensions introduced in the problem, an analysis of all objectives together becomes impractical. Therefore, initially, the focus of interest is on the two main objectives, as shown in Fig. 4.11. A regularity in the curve is observed, with a considerable range of results and the possibility of choosing the most suitable result for the application. Consequently, for the maximum power result, $R = 250.13\ \Omega$ is obtained, for minimum fatigue $R = 2963.77\ \Omega$, and for the compromise between the two results $R = 1107.79\ \Omega$.

The vulnerability values of each objective function can be compared with their respective objective functions, as shown in Fig. 4.12. Due to the complexity introduced in the problem, the variability curves do not exhibit a regular Pareto-like shape as in the other results. Additionally, the graphs show that the maximum, minimum, and compromise values are all the same result point, indicating that, in terms of variability, there is only one optimal solution compared to its specific function. Nevertheless, as in the previous results, the variability values are on the scale of 1×10^{-2}, highlighting the inherent robustness of the problem.

The same optimization problem is computed for the parallel resonant circuit. The results are presented in Fig. 4.13, showing a relatively linear curve, enabling the selection of results for maximum power ($R = 408.09\ \Omega$, $L = 4.33$ H), minimum fatigue damage ($R = 8153.96\ \Omega$, $L = 9.99$ H), and compromise between the results ($R = 1132.16\ \Omega$, $L = 9.12$ H). An interesting characteristic to discuss is the presence of a cluster of solu-

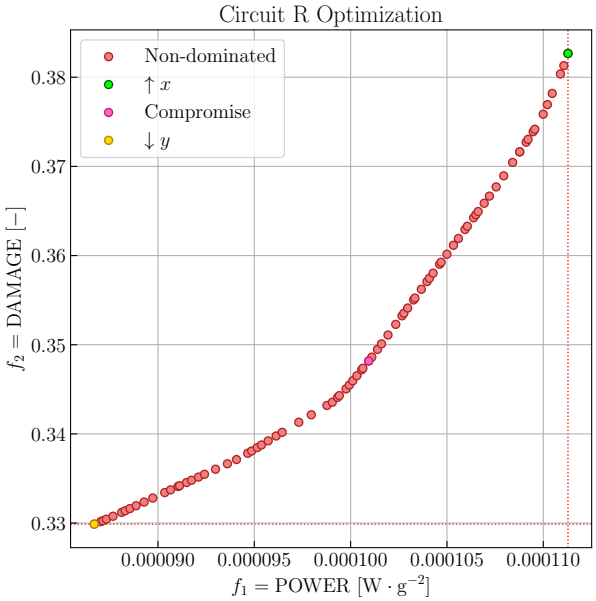

Figure 4.11: Non-dominated optimal solutions in robust power and fatigue analysis with resistive circuit.

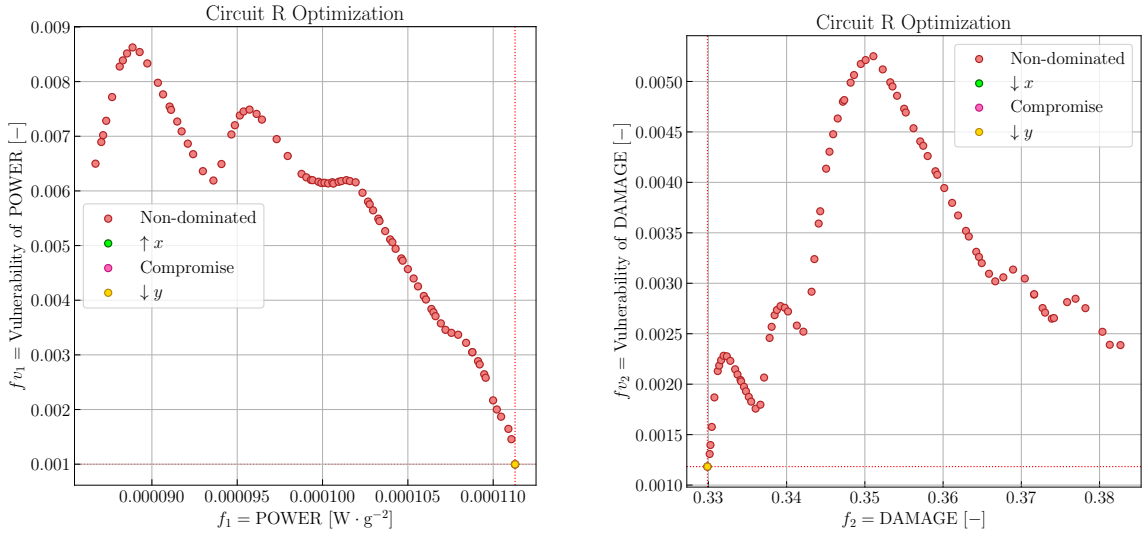

(a) Harvested energy

(b) Fatigue

Figure 4.12: Non-dominated optimal solutions in robust power and fatigue analysis with resistive circuit for vulnerability.

tions at the beginning of the Pareto curve. Initially, they are clearly not dominated by the others. However, in a multi-objective analysis of higher dimensions than three, selecting non-dominated points is not trivial.

Similarly, the vulnerability analyses for each objective function show irregular-

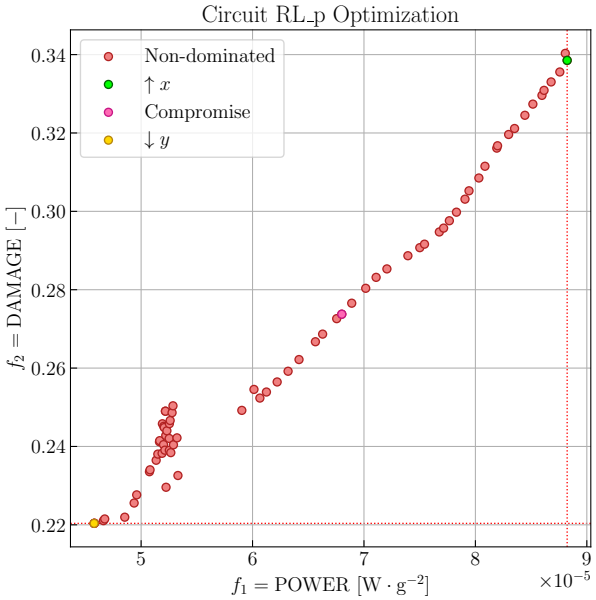

Figure 4.13: Non-dominated optimal solutions in robust power and fatigue analysis with resonant circuit.

ities in the curves, as seen in Fig. 4.14. In the power analysis, the points of maximum and minimum are close, whereas in the damage graph, there is still a possibility of selection between minimum damage and minimum variability. However, the low vulnerability values limit the choice of solutions based solely on robustness, resulting in an analysis focused on the main objectives.

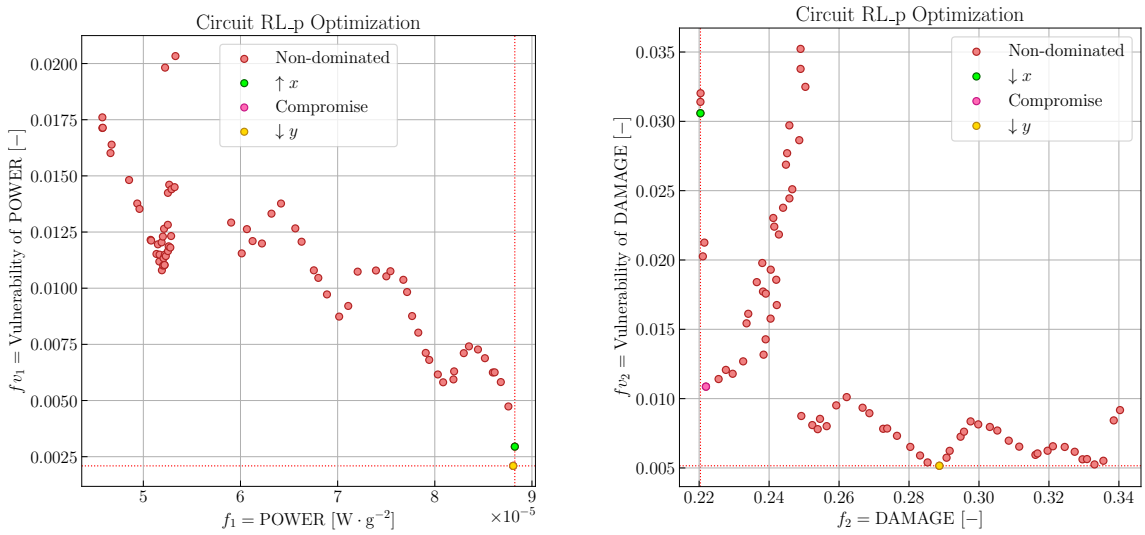

(a) Harvested energy

(b) Fatigue

Figure 4.14: Non-dominated optimal solutions in robust power and fatigue analysis with resonant circuit for vulnerability.

Chapter V

Topology optimization

In this chapter, the topological influence of the piezoelectric layer will be incorporated into the optimization problem, analyzing the advantages of using PZT elements at strategic points.

5.1 Multi-objective parametric optimization

A cantilever beam structure was chosen to assess the compromise between the two objectives along with the inclusion of topology in the optimization problem. As shown in Fig. 5.1, the piezoelectric patch was inserted at the base of the structure, connected to the shunt circuit with impedance $\boldsymbol{Z}(\omega)$, modeled by the FSDT plate theory. Both a resistive and a parallel resonant circuit were analyzed and compared.

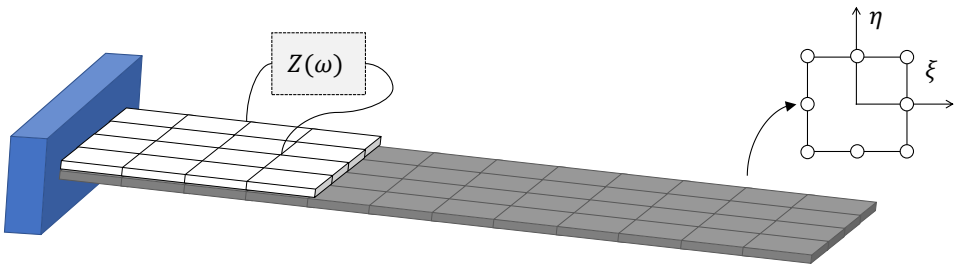

Figure 5.1: Schematic model of the beam structure and the shunt circuit.

Combining the amount of harvested energy with the fatigue damage indicator, and incorporating the circuit parameters along with geometric parameters of the patch, we have the multi-objective optimization problem described in:

$$\begin{aligned} \min_{\boldsymbol{R},\boldsymbol{L},\delta_\mathrm{t},\delta_\mathrm{l}} \quad & \boldsymbol{F}_\mathrm{o} = \begin{bmatrix} -\Upsilon & \mathbb{E}\left[D_\mathrm{sines}\right] \end{bmatrix}^\mathsf{T} \\ \text{s.t.} \quad & R_\mathrm{min} \leq \boldsymbol{R} \leq R_\mathrm{max} \\ & L_\mathrm{min} \leq \boldsymbol{L} \leq L_\mathrm{max} \\ & \delta_\mathrm{min} < \delta_\mathrm{t}, \delta_\mathrm{l} \leq \delta_\mathrm{max} \end{aligned} , \tag{5.1}$$

where the geometric parameters δ_t and δ_l correspond to the percentage of thickness and length of the piezoelectric layer relative to the base structure.

The proposed simulation concerns a beam with a length of 750 mm, width of 60 mm, and thickness of 5 mm, made of aluminum with a modulus of elasticity $E = 70$ GPa, Poisson's ratio $\nu = 0.33$, density $\rho = 2700\,\mathrm{kg/m^3}$, tensile strength $R_\mathrm{m} = 343$ MPa, and shear stress $\tau_1 = 92$ MPa. The limits of the design variables are $[0, 1]$ kΩ for resistance R, $[0, 10]$ H for inductance L, and $[10\%, 40\%]$ for the ratios δ_t and δ_l. The optimal results located on the Pareto frontier are shown in Fig. 5.2. This figure illustrates the results for both resistive and resonant cases. Points a and b represent the best compromise between harvested power and damage. The corresponding optimal design variables are summarized in Table 5.1.

Solution	R	L	δ_t	δ_l	f_1	f_2
a	$1000\,\Omega$	–	0.35	0.30	$12\,\mathrm{mW \cdot g^{-1}}$	0.73
b	$622\,\Omega$	10 H	0.37	0.30	$5\,\mathrm{mW \cdot g^{-1}}$	0.73

Table 5.1: Optimal non-dominated parameters (a: resistive case, b: resonant case).

For this specific modeled structure, the positions of the boundaries show that the resistive circuit presents the best compromise between the objectives. For the same level of damage, it produces a higher harvested power. One possible explanation for this behavior could be the main characteristic of the resonant circuit, which attenuates vibrations by introducing an electrical resonance and acting as a mechanical absorber, in contrast to the resistive circuit.

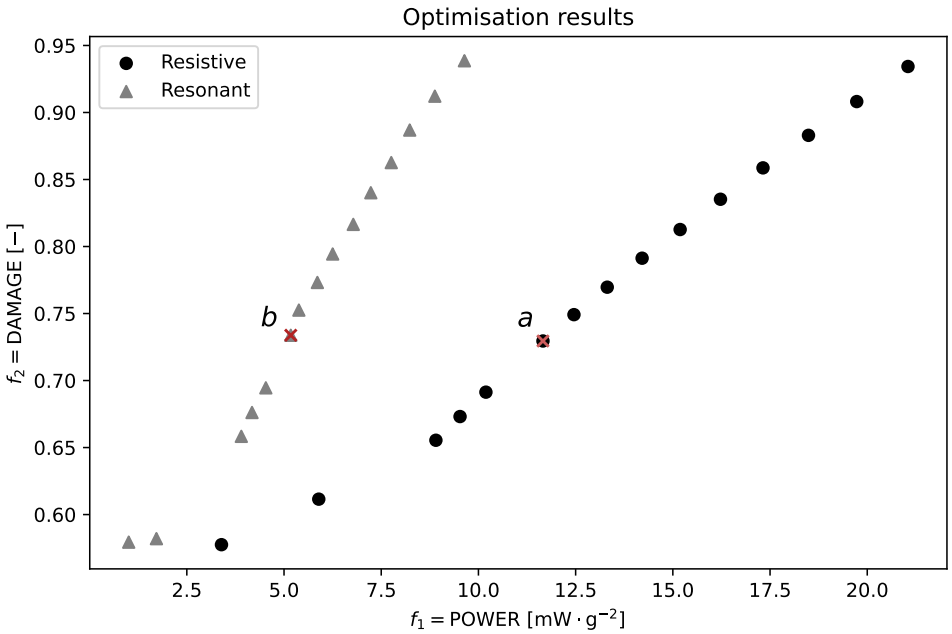

Figure 5.2: Optimal design variables (a: resistive case, b: resonant case).

5.2 Modal Strain Energy

As observed in previous studies on energy harvesting, the incorporation of patches is determined by the manufacturing process of the piezoelectric ceramic, which is the main factor in choosing the location of the PZT layer. Consequently, an intelligent approach to patch integration involves strategically positioning them in regions that exhibit high levels of modal strain energy, according to:

$$\boldsymbol{\Xi}_i = \boldsymbol{\Theta}_i^{\mathsf{T}} \boldsymbol{K} \boldsymbol{\Theta}_i \ , \tag{5.2}$$

where $\boldsymbol{\Theta}_i$ is the modal displacement of the i-th mode (ZHAO et al., 2020). Considering the plate structure, the modal strain energy is calculated for each mode. The criterion for piezoelectric placement follows the percentage of strain energy, where the placement is made in the region covering 60% of the total modal strain energy, resulting in the configuration of a single patch covering the elements near the support region for both structures. The result of the piezoelectric layer is depicted in Fig. 5.3:

The same optimization problem as in Eq. 4.6 was solved, but with a reduced amount of piezoelectric layer. Following the same population and generation parameters, the results for the resistive circuit are shown in Fig. 5.4, with the points of maximum power

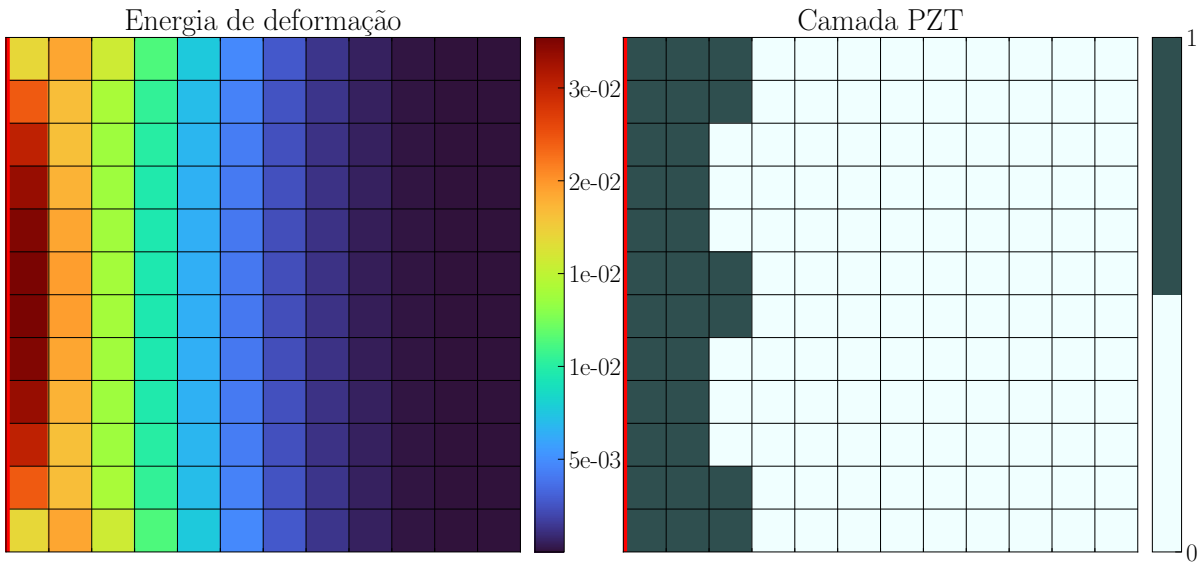

Figure 5.3: Modal strain energy of the first mode and the distribution of the piezoelectric layer.

($R = 1843.48\ \Omega$), minimum fatigue ($R = 3289.59\ \Omega$), and the compromise between the two objectives ($R = 4070.17\ \Omega$). Despite obtaining a regular curve, there is a concentration of results in certain regions, indicating that a smaller amount of piezoelectric layer results in a more significant influence of circuit parameters on the linearity of the results.

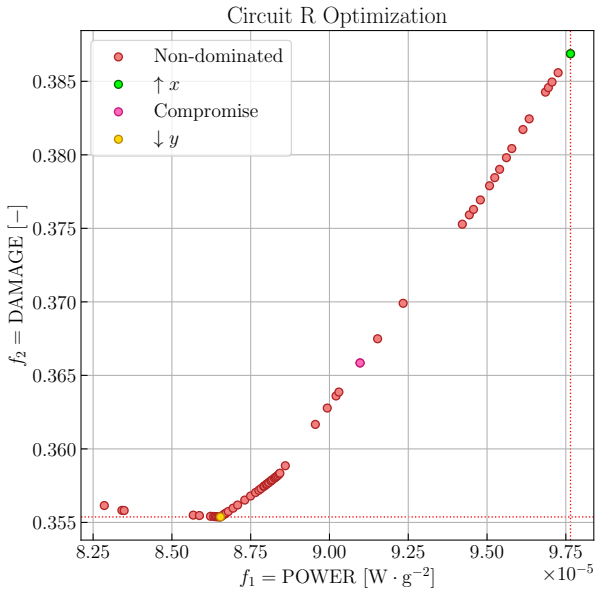

Figure 5.4: Non-dominated optimal solutions in robust power and fatigue analysis with resistive circuit in partial treatment.

In the resonant circuit, however, the curve of results for the main objectives has

an irregular shape, with a concentration of results at maximum power and a dispersion of the remaining results. However, the selection of the desired results can still be made, with maximum power ($R = 1501.67\ \Omega$, $L = 9.99$ H), minimum fatigue ($R = 2189.66\ \Omega$, $L = 0.25$ H), and compromise between the two objectives ($R = 71.76\ \Omega$, $L = 8.44$ H).

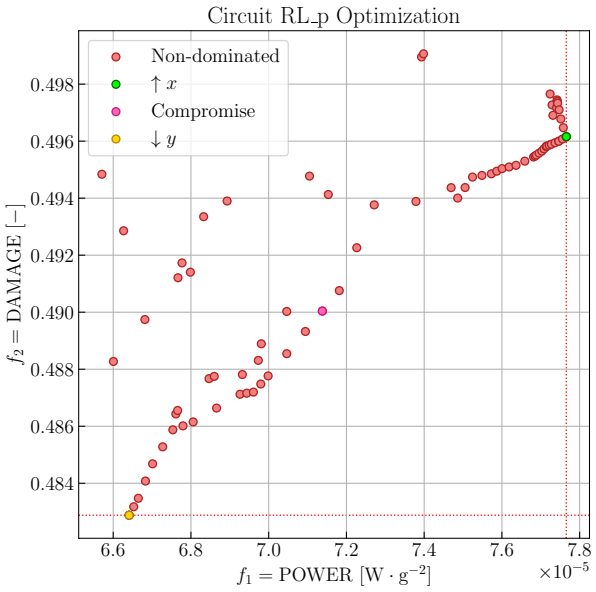

Figure 5.5: Non-dominated optimal solutions in robust power and fatigue analysis with resonant circuit in partial treatment.

Indeed, both in the resistive and resonant circuits, comparing the results with the previous analysis of the complete PZT layer, it is noticeable that there are lower power values and higher fatigue damage. A superficial interpretation suggests that there was no gain in applying the partial treatment, as both objectives are inferior to those previously presented. However, it is essential to consider that the amount of piezoelectric material in the structure is a crucial factor for certain applications due to the increase in mass, manufacturing limitations, and practical constraints. Therefore, achieving results with the partial treatment close to those of the complete layer, even with approximately 21% of the material used, represents a significant design gain.

5.3 Location of piezoelectric patches

A second approach is carried out, now considering the placement of piezoelectric patches on the structure. The number of rectangular patches is defined parametrically

before the optimization, and the design variables added to the optimization problem follow the definition in Fig. 5.6:

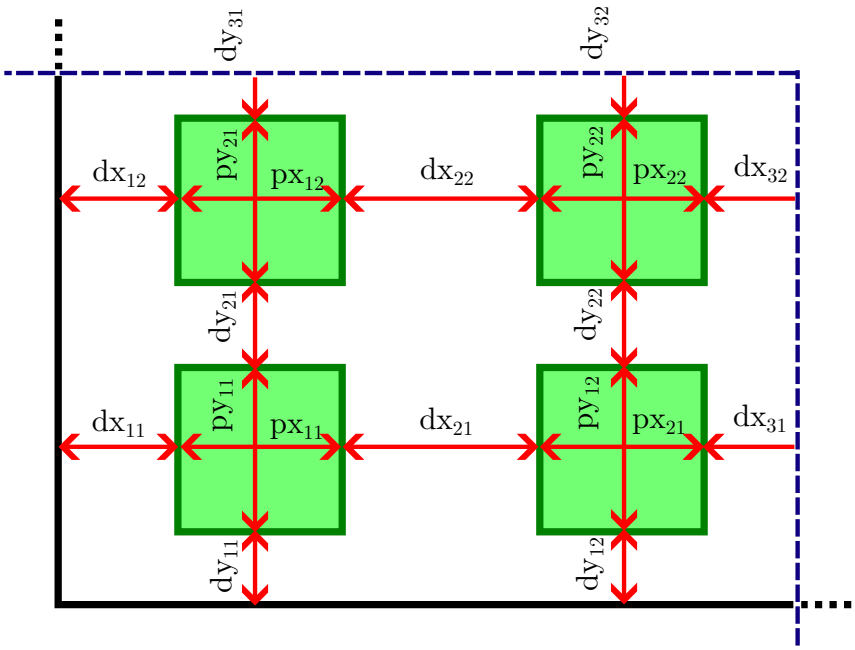

Figure 5.6: Patch distribution methodology.

The new constraints added to the optimization problem describe the distance between the patches (dx and dy) and the length of the patches in each direction (px and py). These variables correspond to the number of elements in the finite element model, thus $p, d \in \mathbb{Z}$. The subscript in d_{ij} and p_{ij} corresponds to the location in the i-th row in the primary direction and in the j-th row in the secondary direction. In the general case, the additional constraints are:

$$\begin{cases} 0 \leq dx_{ij} \leq dx_{\max} & i \in \{1, \ldots, n_{\mathrm{x}}\} \; ; \; j \in \{1, \ldots, n_{\mathrm{y}}\} \\ 0 \leq dy_{ij} \leq dy_{\max} & i \in \{1, \ldots, n_{\mathrm{y}}\} \; ; \; j \in \{1, \ldots, n_{\mathrm{x}}\} \\ 1 \leq px_{ij} \leq px_{\max} & i \in \{1, \ldots, n_{\mathrm{x}}\} \; ; \; j \in \{1, \ldots, n_{\mathrm{y}}\} \\ 1 \leq py_{ij} \leq py_{\max} & i \in \{1, \ldots, n_{\mathrm{y}}\} \; ; \; j \in \{1, \ldots, n_{\mathrm{x}}\} \end{cases}, \tag{5.3}$$

with n_{y} as the number of patches in the x and y directions, respectively. The maximum number of each parameter is carefully calculated based on the chosen number of patches and a maximum coverage percentage of the piezoelectric layer. This methodology can also be applied to a beam structure, where a one-dimensional version is applied and the constraints in the y direction are not considered. The complete optimization problem for the location of the patches is represented by:

$$
\begin{aligned}
\min_{\boldsymbol{R},\boldsymbol{L},\boldsymbol{dx},\boldsymbol{dy},\boldsymbol{px},\boldsymbol{py}} \quad & \boldsymbol{F}_{\mathrm{o}}^{\mathrm{R}} = \begin{bmatrix} -\Upsilon & \mathcal{V}_{\Upsilon} & \mathbb{E}\left[D_{\mathrm{sines}}\right] & \mathcal{V}_{\mathbb{E}[D_{\mathrm{sines}}]} \end{bmatrix}^{\mathsf{T}} \\
\text{s.t.} \quad & R_{\min} \leq \boldsymbol{R} \leq R_{\max} \\
& L_{\min} \leq \boldsymbol{L} \leq L_{\max} \\
& 0 \leq \boldsymbol{dx} \leq dx_{\max} \\
& 0 \leq \boldsymbol{dy} \leq dy_{\max} \\
& 1 \leq \boldsymbol{px} \leq px_{\max} \\
& 1 \leq \boldsymbol{py} \leq py_{\max}
\end{aligned} \quad . \tag{5.4}
$$

The insertion of geometric parameters of the piezoelectric layer, along with the robust analysis of the electromechanical system, results in a problem with a higher degree of complexity in calculating optimal solutions. This can be observed in the results of Fig. 5.7 for the resistive circuit. The Pareto curve is not as well-defined as previously, with the presence of several dispersed points throughout the graph and some with the same variable results. It is also evident that the primary benefit of the analysis was the increase in energy, but at the cost of a high level of fatigue damage. In the points of interest, we have maximum power ($R = 8923.11\ \Omega$), minimum fatigue index ($R = 75307.59\ \Omega$), and the compromise between the two results ($R = 70250.50\ \Omega$).

Similarly, the results from Fig. 5.8 for the resonant circuit show a gain in the collected energy, but with a smaller increase in structural fatigue damage. In this optimization problem, the resonant circuit proves to be more advantageous for the desired objectives. The selected points of interest are maximum power ($R = 3624.72\ \Omega$, $L = 9.87$ H), minimum fatigue damage ($R = 32011.89\ \Omega$, $L = 5.32$ H), and the compromise between objectives ($R = 35.84\ \Omega$, $L = 8.72$ H).

With the selected points, it is possible to obtain the distribution of the PZT layer along the structure for each of the points, as shown in Fig. 5.9 for the resistive circuit and Fig. 5.10 for the resonant circuit. It is observed that the concentration of patches near the base results in greater energy harvesting, while patches in the central regions closer to the free edge result in less fatigue damage. Consequently, the compromise result

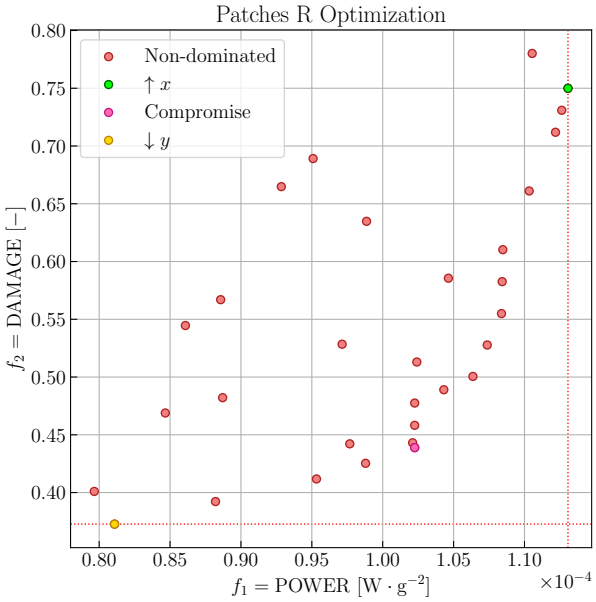

Figure 5.7: Non-dominated optimal solutions in robust power and fatigue analysis with resistive circuit in patch distribution.

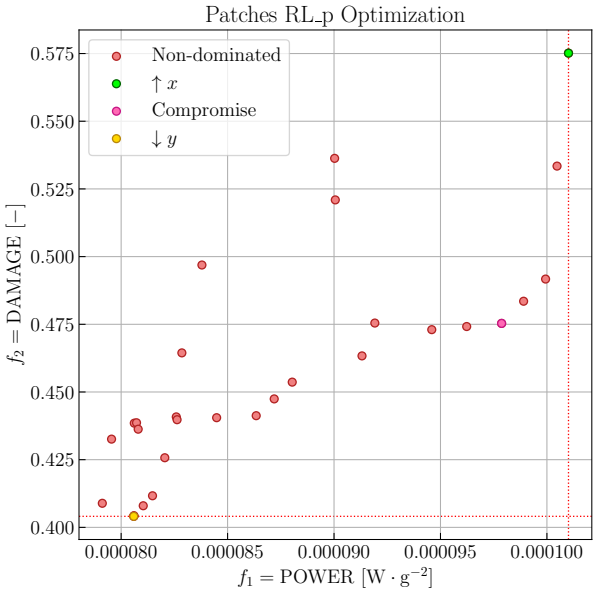

Figure 5.8: Non-dominated optimal solutions in power and fatigue analysis robust with resonant circuit in patch distribution.

exhibits a transitional characteristic between the two extreme outcomes.

The quantity of patches, defined parametrically before solving the optimization problem, has a significant influence on the results. Additionally, this parameter requires a sufficiently large number of elements in both directions to obtain coherent results. Another

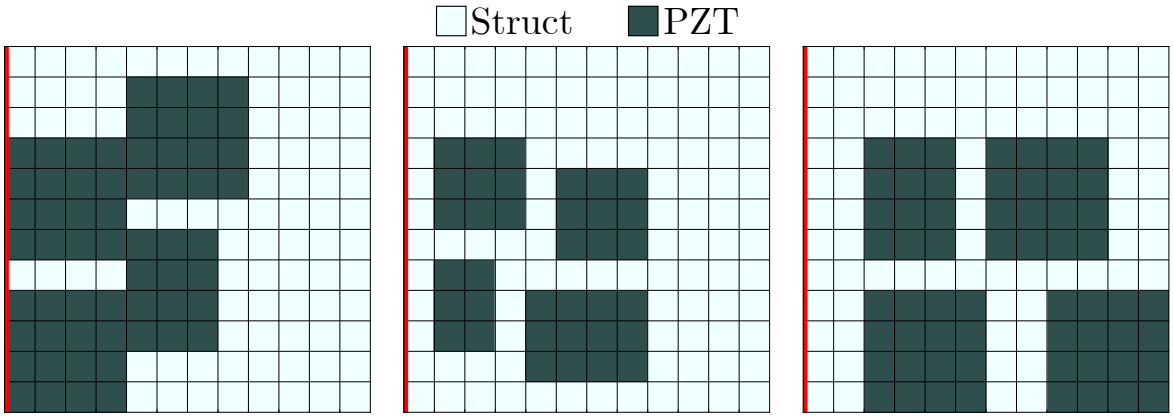

(a) Maximum power (b) Compromise (c) Minimum damage

Figure 5.9: Patch placement optimization with resistive circuit.

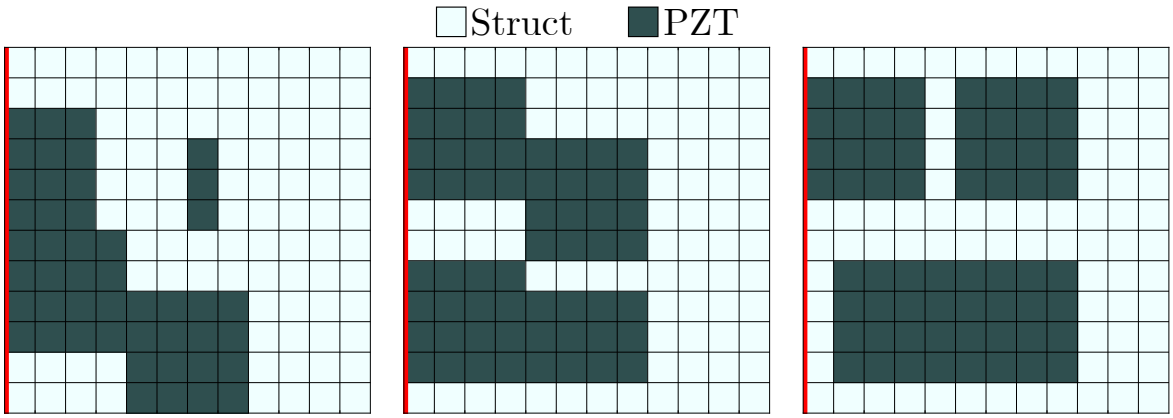

(a) Maximum power (b) Compromise (c) Minimum damage

Figure 5.10: Patch placement optimization with resonant circuit.

limiting factor in this methodology is that the reference coordinates for the patch locations are always one of the structure's bases, resulting in configurations without symmetry axes.

5.4 Piezoelectric Layer Density

In topology optimization problems, especially in static problems, the use of the finite element method has the advantage of allowing the mechanical influence of each element to be weighted in the overall calculation of responses. However, at the same time, the number of finite elements in the mesh limits the detail of the results, requiring a preliminary analysis of the applications of the final design.

In the electromechanical problem, the idea of topological optimization is similar

to static topological analyses, but with a focus on the influence of the PZT layer. This methodology is used to define a nonlinear distribution of the piezoelectric layer throughout the structure. For this, the influence of the piezoelectric material of each element is considered by the binary presence or absence of the layer ($\rho \in \mathbb{Z}_2$) and its contribution to the global mechanical and electrical matrices for the total number of elements e in the structure:

$$\boldsymbol{M}^{\{e\}} = \boldsymbol{M}^{\{e\}}_{\text{st}} + \rho_e \boldsymbol{M}^{\{e\}}_{\text{pzt}} \ , \tag{5.5}$$

$$\boldsymbol{K}^{\{e\}}_{\text{u}\phi} = \rho_e \boldsymbol{K}^{\{e\}}_{\text{u}\phi,\text{pzt}} \ , \tag{5.6}$$

$$\boldsymbol{K}^{\{e\}}_{\text{uu}} = \boldsymbol{K}^{\{e\}}_{\text{uu,st}} + \rho_e \boldsymbol{K}^{\{e\}}_{\text{uu,pzt}} \ , \tag{5.7}$$

$$\boldsymbol{K}^{\{e\}}_{\phi\phi} = \rho_e \boldsymbol{K}^{\{e\}}_{\phi\phi,\text{pzt}} \ . \tag{5.8}$$

In addition to the base optimization problem, the constraint $\sum \rho_e V_e - f_\text{V} \sum V_e \leq 0$ is added for each element e, with f_V being equal to the maximum coverage percentage and $\rho_e \in \{0, 1\}$. The constraints can be represented in vector forms, where $\boldsymbol{\rho}_\text{PZT}$ is the coverage density vector and N is the number of elements in the structure:

$$\begin{aligned} \min_{\boldsymbol{R},\boldsymbol{L},\boldsymbol{\rho}_\text{PZT}} \quad & \boldsymbol{F}^\text{R}_\text{o} = \begin{bmatrix} -\Upsilon & \mathcal{V}_\Upsilon & \mathbb{E}\left[D_\text{sines}\right] & \mathcal{V}_{\mathbb{E}[D_\text{sines}]} \end{bmatrix}^\intercal \\ \text{s.t.} \quad & R_\text{min} \leq \boldsymbol{R} \leq R_\text{max} \\ & L_\text{min} \leq \boldsymbol{L} \leq L_\text{max} \\ & \text{sum}(\boldsymbol{\rho}_\text{PZT})/N - f_\text{V} \leq 0 \\ & \boldsymbol{\rho}_\text{PZT} \in \{0, 1\} \end{aligned} \ . \tag{5.9}$$

Still within the scope of integrating the topology of the piezoelectric layer into the optimization problem, we see in Fig. 5.11 the dispersion of non-dominated results in the case of the resistive circuit. Nevertheless, there is a defined sequence of results on a Pareto frontier. Therefore, we define the points of interest as maximum power ($R = 5221.64\ \Omega$), minimum fatigue damage ($R = 66996.57\Omega$), and the compromise between the objectives ($R = 70367.44\ \Omega$).

Finally, solving the optimization problem for the resonant circuit presented

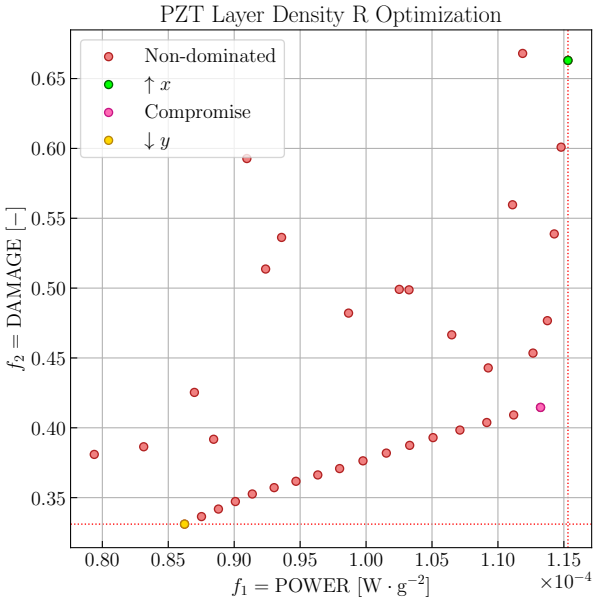

Figure 5.11: Non-dominated optimal solutions in robust power and fatigue analysis with resistive circuit in PZT layer density.

in Fig. 5.12 allows us to select points of interest, with higher collected energy ($R = 1487.23\ \Omega$, $L = 9.99$ H), lower fatigue damage ($R = 31266.96\ \Omega$, $L = 2.43$ H), and the compromise between the two objectives ($R = 58.09\ \Omega$, $L = 9.04$ H).

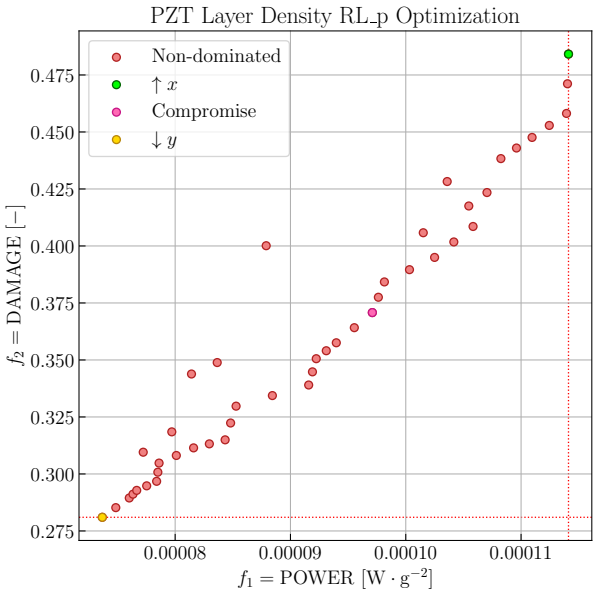

Figure 5.12: Non-dominated optimal solutions on robust power and fatigue analysis with resonant circuit at PZT layer density.

In the piezoelectric layer density problem, a wider range of results is observed,

with maximum and minimum values surpassing previous analyses. The power reaches values of 1.15×10^{-4} W $\cdot$ g^{-2}, while the damage reaches 0.276 in its minimum values. This explicitly demonstrates that considering topology in the optimization problem, where the definition of the piezoelectric layer location is more freely determined, allows for increased efficiency of the structure considering the chosen objectives.

When viewing the results of interest in Figs. 5.13 and 5.14, we initially notice the irregular shapes of the piezoelectric material distribution. Upon closer inspection, there is a pattern of concentration for both circuits towards maximum energy harvesting, which consists of a concentration of the layer at the fixed base of the structure. For the configuration of minimum damage, the results show a shift of the concentration towards the more central region of the plate, with small clusters at the upper and lower ends. Finally, in the compromise case, we see a combination of the two aforementioned cases.

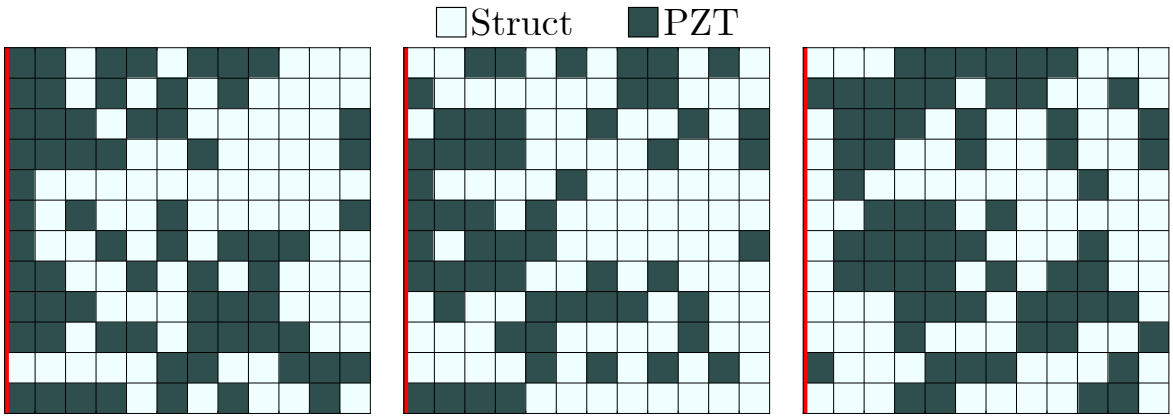

(a) Maximum power (b) Compromise (c) Minimum damage

Figure 5.13: Optimization of PZT layer density with resistive circuit.

One limitation of this methodology is the distribution of piezoelectric material without considering the quantity of neighboring elements that also have the PZT portion. This is evident from the presence of isolated elements in the presented results. Additionally, different layer distributions with similar resistance and impedance values can generate results close to the objective functions. This makes it difficult for optimization algorithms to differentiate and select these specific cases.

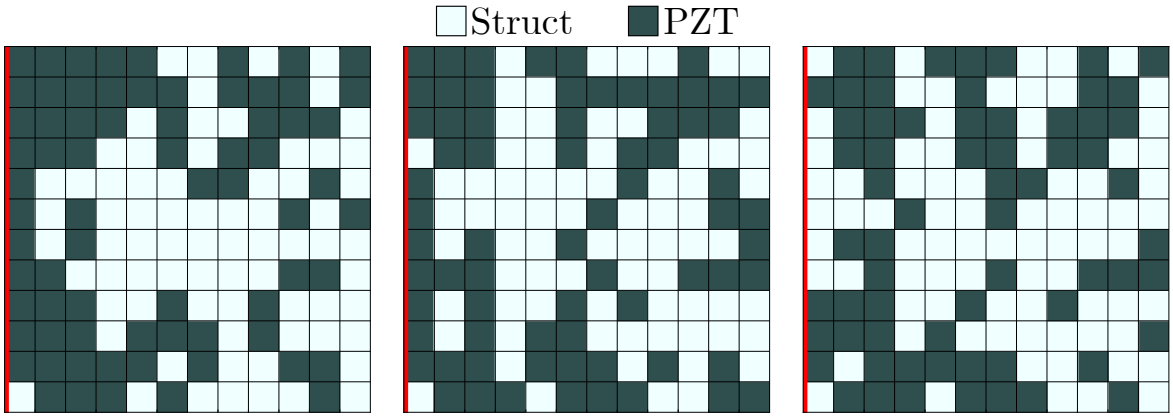

(a) Maximum power (b) Compromise (c) Minimum damage

Figure 5.14: Optimization of PZT layer density with resonant circuit.

5.5 Comparison with fine mesh

After the conclusions from the previous analyses, a final comparison was conducted, now using a beam and a plate structure with the same characteristics as before (Fig. 5.15), except for the number of elements (a finer mesh of 18×14 elements for the plate and 18×4 for the beam), deterministic calculation without robustness, and considering only a resistive shunt circuit. For this purpose, similarly, a neural network was trained with a larger amount of input data, in a narrower resistance range of $[10^2, 10^4]$. The Pareto curves containing the non-dominated results are shown in Figure 5.16.

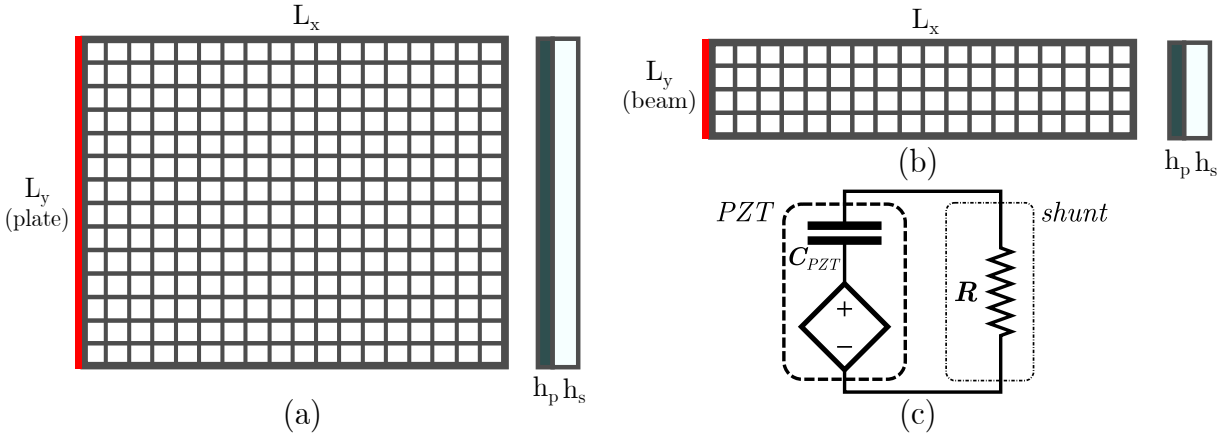

Figure 5.15: Components of the structure (a) Plate (b) Beam (c) Resistive circuit.

In both structures, the distribution of patches along with the strain energy exhibits the worst non-dominated results. In the beam, the strain energy consists of only one

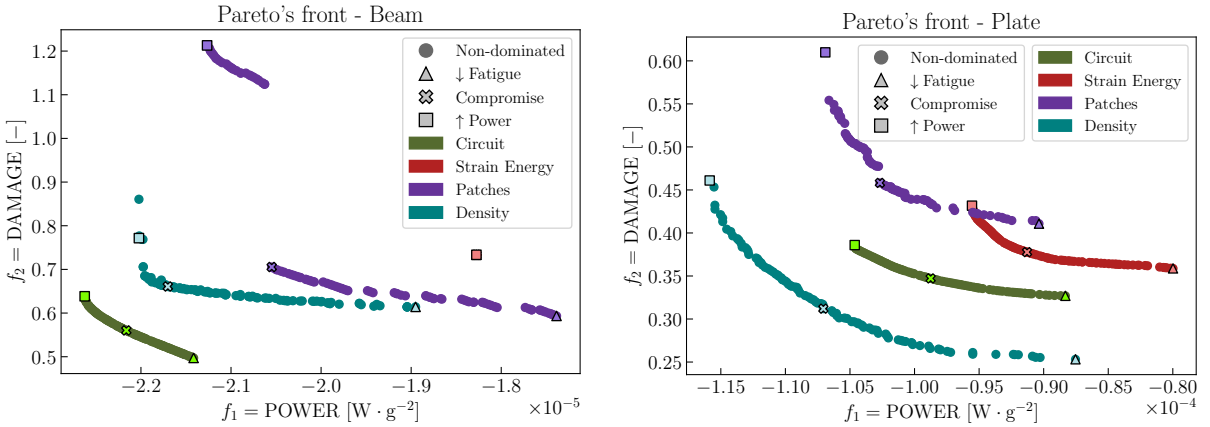

(a) Beam (b) Plate

Figure 5.16: Results for the three circuit cases.

point, indicating the maximum resistance for all non-dominated solutions. Additionally, solutions with higher collected energy have a fatigue indicator greater than 1, implying a failure of this structure. Regarding the plate, although other fronts dominate the patches, it can be noted that it can collect more energy in the extremely superior solutions than the reference case of the circuit. As for the density case, the results only outperform the others in the plate structure. It is important to highlight its better performance compared to the reference circuit optimization, even with less piezoelectric material and therefore less weight added to the structure. Finally, the resulting distribution of the piezoelectric layer is presented in Fig. 5.17, for the patch and layer density cases of each structure.

The compromise solutions for the patch case show a more scattered concentration for the beam and a more centralized location for the plate. Along the solution curve, we observe a transition from positioning closer to the fixed support to an area in the middle-right. These solutions result in an intermediate configuration to minimize fatigue and maximize harvested energy.

Regarding the density case of the piezoelectric layer, although there are some random shapes of the PZT layer, there is a clear scattered concentration in small regions along the length of the beam, following the same logic as the patch case. For the plate, the solution has a large region closer to the fixed support that assimilates the region with the highest modal energy. In the rest of the structure, some voids appear in the central area along with small regions at the free edge.

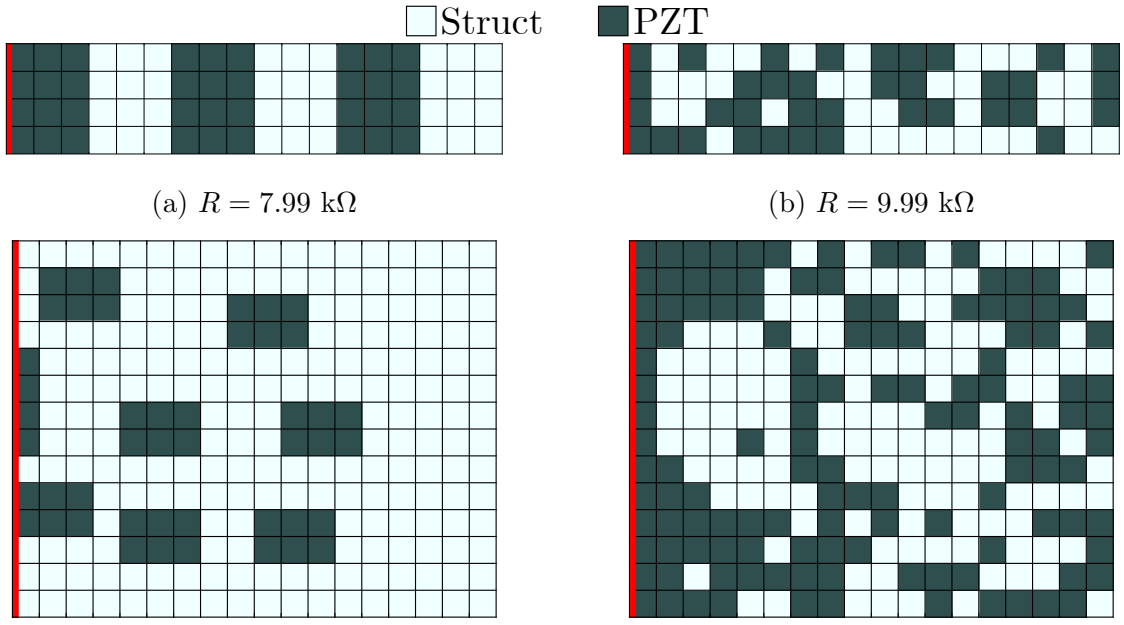

(a) $R = 7.99$ kΩ (b) $R = 9.99$ kΩ

(c) $R = 3.22$ kΩ (d) $R = 2.44$ kΩ

Figure 5.17: Beam distribution (a) patches, (b) density; Plate distribution (c) patches, (d) density.

To quantify the gain of the objectives, we use two necessary factors for the following analyses. The first is the percentage coverage of the piezoelectric layer $\mathcal{C}_{\%}$ in:

$$\mathcal{C}_{\%} = \frac{N_{\text{PZT}}}{N} \ , \tag{5.10}$$

which is defined by the ratio between the number of piezoelectric elements N_{PZT} and the total number of finite elements in the structure N. This factor allows us to analyze the amount of gain in a given objective by the amount of piezoelectric material added to the structure. This value ranges from $(0, 1]$, with 1 representing full coverage of the structure with PZT material, as in the case of optimization of the circuit only.

The second factor used to quantify the results is the Relative Efficiency RE_{η}, as:

$$RE_{\eta} = \frac{\Upsilon}{\mathbb{E}\left[D_{\text{sines}}\right]} \ , \tag{5.11}$$

which this value does not have a defined range, but it allows for the comparison between two distinct results. Its interpretation is based on the amount of energy harvested per accumulated fatigue damage factor. The higher the relative efficiency values, the more

energy the chosen configuration will be able to collect with a better compromise concerning the fatigue damage present in the structure.

Selecting the results of the best compromise between the two objectives from each of the 4 presented cases, we can summarize them in Tab. 5.2, where the percentage coverage of the piezoelectric layer, the results of the best compromise for each objective, the value of the ratio between the objective and the percentage coverage, and the relative efficiency are presented.

		$\mathcal{C}_{\%}$	Υ	$\mathbb{E}[D_{\text{sines}}]$	$\Upsilon/\mathcal{C}_{\%}$	$\mathbb{E}[D_{\text{sines}}]/\mathcal{C}_{\%}$	RE_{η} ($\uparrow$)
Beam	Circuit	1,00	2,22	0,56	2,22	0,56	3,96
	Density	0,50	2,18	0,66	4,36	1,32	3,30
	Patches	0,50	2,05	0,70	4,10	1,40	2,93
	Strain Energy	0,22	1,82	0,73	8,19	3,29	2,49
Plate	Density	0,50	1,07	0,31	2,14	0,62	3,45
	Circuit	1,00	0,99	0,35	0,99	0,35	2,80
	Strain Energy	0,21	0,91	0,38	4,41	1,84	2,39
	Patches	0,18	1,03	0,45	5,64	2,47	2,29

Table 5.2: Summary of the objectives results sorted by Relative Efficiency.

It is first verified that the value of energy harvesting per percentage of coverage, for both the beam and the plate, is higher than the case of complete coverage of the structure by the piezoelectric layer, where optimization is performed only on the circuit. There are also much higher harvesting values for the beam in the case of modal deformation energy, being the best case when analyzing only the first objective. For the plate, the distribution of patches shows the highest energy collection per piezoelectric element added to the structure.

However, as the analysis also involves the amount of accumulated fatigue damage, a trade-off between high levels of harvested energy and high levels of damage is observed. This can be explained by the mechanical factor added to the structure when inserting a larger amount of piezoelectric elements, due to the consequent increase in stiffness. Thus, a complete layer of PZT material results in greater stiffness and consequently

less damage per amount of PZT layer.

Finally, the relative efficiency factor shows that, in the case of the beam, a complete layer of PZT material has the highest value for both objectives factor. Next is the case of density, followed by patches and modal deformation energy. In the plate structure, the density case of the PZT layer comes first, followed by the complete layer in second place. It can be concluded that in the case of the beam, due to the limitation of the structure's width, the optimization process cannot vary the locality of the piezoelectric elements, thus limiting the efficiency values. In the plate, however, a greater dispersion of the PZT elements is observed, which allows the optimization algorithm to search for the best result.

Chapter VI

Conclusion and perspectives

Conclusion

This work aimed to investigate, analyze, and propose an optimal-robust methodology for designing piezoelectric shunt circuits for vibration attenuation and energy harvesting from vibration in structures subjected to dynamic loading. For this purpose, numerical methods were used to obtain responses to external loads and create a dataset of solutions, which was used to train a metamodel by artificial neural networks, necessary for evaluating the objective functions of multi-objective optimization problems. Solving this problem allows the definition of optimal parameters for maximum energy harvesting, taking into account the minimum accumulated damage in the structure.

The results firstly showed that the variability of design variables has a low influence on the objective functions, indicating that the system is inherently robust. Furthermore, another conclusion drawn was the complexity of the results when optimizing the topology of the piezoelectric layer along with the parameters of the shunt circuit. Secondly, the calculation of optimal values in the optimization problems resulted in an increase in fatigue life and higher collected energy power, allowing for a choice between the trade-off between these two objectives.

These results have significant implications, particularly in demonstrating the possibility of increasing collected energy by altering the topological configurations of the piezoelectric material. The energy gain, without implying a loss of structural life, results in a model resilient to operating conditions. Another significant factor is the use of neural networks in conjunction with electrical parameters, topological parameters, statistical

results of multiaxial fatigue, and power generated by the system. The metamodeling of dynamic systems has already found extensive application over the years, but advances in new architectures and methodologies enable the use of increasingly complex structures in a facilitated manner, as demonstrated in the present work.

Another important result was the user's ability to choose the most suitable case for their needs. In multi-objective optimizations, selecting the best results is not trivial, as seen in the cases presented here. We observe that some cases are more suitable where the amount of harvested energy is the main factor to be decided, while other cases are more advisable for lower accumulation of fatigue damage. However, a key result of the research was the proof of the relative efficiency of using the density method compared to traditional methods and those presented here, which, under the same boundary conditions, can achieve a better trade-off between energy harvesting and fatigue damage.

From a theoretical standpoint, the application of the proposed methodology for structural pre-conception appears feasible, assisting the designer in defining the best configurations for the study at hand. However, considering the technical limitations of utilization, such as the fabrication of piezoelectric elements in irregular shapes and the connection of these elements in a single shunt circuit, it is evident that its application becomes challenging.

List of publications

During the period of development of this Thesis, some articles were published and disseminated at national and international conferences in the area, in addition to articles in journals, including:

- SENA, J. P.; DE LIMA, A. M. G.; BOUHADDI, N.; KACEM, N. Topology Optimization of Smart Structures to Enhance the Performances of Vibration Control and Energy Harvesting. **Smart Materials and Structures**, 2024. DOI: `10.1088/1361-665X/ad69ea`

- BARBOSA, A.; SENA, J. P.; KACEM, N.; BOUHADDI, N. An artificial intelligence approach to design periodic nonlinear oscillator chains under external excitation with stable damped solitons. **Mechanical Systems and Signal Processing**, 2023. DOI: `10.1016/j.ymssp.2023.110879`

- SENA, J. P.; KACEM, N.; DE LIMA, A. M. G.; BOUHADDI, N. Optimization of a smart structure to enhance the reliability and vibrations mitigation/harvesting performances. **6e Congrès Tunisien de Mécanique (CoTuMe 2023)**, Monastir, 2023.

- NUNES, E. P.; DE LIMA, A. M. G.; SENA, J. P. Use of a recurrence based fractional derivative model in the analysis of the influence of geometrical parameters in the transient response of viscoelastic beams. **XLII Ibero-Latin-American Congress on Computational Methods in Engineering (CILAMCE-2021)**, Rio de Janeiro, 2021.

- SENA, J. P.; DINIZ, G.; DE LIMA, A. M.; NUNES, E. P.; ARAÚJO DELGADO FILHO, M. Design optimization for base excitation problem of a cantilevered beam coupled with shunt circuit on fatigue analysis. **26th International Congress of Mechanical Engineering (COBEM-2021)**, 2021. DOI: 10.26678/ABCM.COBEM2021.COB2021-1632

- GARCIA, G. F.; NUNES, E. P.; SENA, J. P.; DE LIMA, A. M. G. Numerical analysis of a beam with and without viscoelastic treatment subject to cyclic loading in the time domain. **XLI Ibero-Latin-American Congress on Computational Methods in Engineering (CILAMCE-2020)**, Foz do Iguaçu, 2020.

- NUNES, E. P.; GARCIA, G. F.; SENA, J. P.; DE LIMA, A. M. G. Use of an improved fractional derivative model for transient analyses of viscoelastic systems. **XLI Ibero-Latin-American Congress on Computational Methods in Engineering (CILAMCE-2020)**, Foz do Iguaçu, 2020.

- SENA, J. P.; GARCIA, G. F.; DE LIMA, A. M. G.; NUNES, E. P. Fatigue life estimation in a beam subject to random loads using probabilistic methods in the frequency domain. **XLI Ibero-Latin-American Congress on Computational Methods in Engineering (CILAMCE-2020)**, Foz do Iguaçu, 2020.

Perspectives

Some points are interesting to explore in more detail, suggested as further research. One of them is the association of other types of shunt circuits, such as series

resonant circuits, capacitive circuits, and multimodal circuits. The influence of each of these types can help in better harnessing vibration energy. Another suggestion would be to create a more generic neural network that allows for a freer design of the structure during optimization. This factor enables a wide application in real-world problems without the need to create a new dataset for every change in design conditions. Finally, in addition, comparing different boundary conditions would allow the methodology to be explored in different types of structures, encompassing other types of mechanical structure applications.

Specific suggestions for future work:

- Definition of a general metamodel with a deep neural network to obtain the dynamic responses of electromechanical structures, for different types of meshes and physical/geometric characteristics;
- Application of the optimal-robust methodology in multimodal shunt circuits to explore the attenuation of simultaneous vibrating modes, in addition to increasing the energy harvesting range;
- Inclusion of topological constraints in the optimization process to meet practical application limitations, such as clustering and convolutional filters;
- Comparison between different types of boundary conditions, such as supports and applied forces;
- Development of an experiment bench for practical validation of theoretical results;
- Association of a network of circuits shunt with different polarizations in the piezoelectric elements of the structure.

References

ABS. **Rules for Building and Classing Steel Vessels 2010**. Houston, TX: American Bureau of ShippingABS, 2010.

AOUALI, Kaouthar; KACEM, Najib; BOUHADDI, Noureddine. Functionalization of Internal Resonance in Magnetically Coupled Resonators for Highly Efficient and Wideband Hybrid Vibration Energy Harvesting. **Sensors**, MDPI AG, v. 22, n. 19, p. 7657, Oct. 2022. ISSN 1424-8220. DOI: 10.3390/s22197657.

AOUALI, Kaouthar et al. On the Optimization of a Multimodal Electromagnetic Vibration Energy Harvester Using Mode Localization and Nonlinear Dynamics. **Actuators**, MDPI AG, v. 10, n. 2, p. 25, Jan. 2021. ISSN 2076-0825. DOI: 10.3390/act10020025.

BAILEY, John et al. Evidence relating to object-oriented software design: A survey. In: FIRST International Symposium on Empirical Software Engineering and Measurement (ESEM 2007). [S.l.]: IEEE, Sept. 2007. DOI: 10.1109/esem.2007.58.

BALAJI, P. S.; KARTHIK SELVAKUMAR, K. Applications of Nonlinearity in Passive Vibration Control: A Review. **Journal of Vibration Engineering &; Technologies**, Springer Science and Business Media LLC, v. 9, n. 2, p. 183–213, June 2020. ISSN 2523-3939. DOI: 10.1007/s42417-020-00216-3.

BAUCHAU, Olivier Andre. **Structural analysis with applications to aerospace structures**: with applications to aerospace structures. [S.l.]: Springer, 2009. P. 943. ISBN 9789048125166.

BENDAT, Piersol. **Random Data 4E**. [S.l.]: John Wiley & Sons, 21 Jan. 2010. 636 pp. ISBN 0470248777.

BEYER, Hans-Georg; SENDHOFF, Bernhard. Robust optimization – A comprehensive survey. **Computer Methods in Applied Mechanics and Engineering**, Elsevier BV, v. 196, 33–34, p. 3190–3218, July 2007. ISSN 0045-7825. DOI: 10.1016/j.cma.2007.03.003.

BORESI, Arthur. **Elasticity in engineering mechanics**. Hoboken, N.J: Wiley, 2011. ISBN 9780470402559.

BORESI, Arthur P.; CHONG, Kenneth P.; LEE, James D. **Elasticity in Engineering Mechanics**. [S.l.]: WILEY, 1 Dec. 2010. 638 pp. ISBN 0470402555.

BOYLESTAD, Robert. **Introdução à anaálise de circuitos**. São Paulo: Pearson Education do Brasil, 2004. ISBN 9788587918185.

CHEE, Clinton Yat Kuan. **Static shape control of laminated composite plate smart structure using piezoelectric actuators**. [S.l.]: University of Sydney. Aeronautical Engineering, 2000.

CHEN, Nian-Zhong; WANG, Ge; GUEDES SOARES, C. Palmgren–Miner's rule and fracture mechanics-based inspection planning. **Engineering Fracture Mechanics**, Elsevier BV, v. 78, n. 18, p. 3166–3182, Dec. 2011. ISSN 0013-7944. DOI: 10.1016/j.engfracmech.2011.08.002.

DADRAS ESLAMLOU, Armin; HUANG, Shiping. Artificial-Neural-Network-Based Surrogate Models for Structural Health Monitoring of Civil Structures: A Literature Review. **Buildings**, MDPI AG, v. 12, n. 12, p. 2067, Nov. 2022. ISSN 2075-5309. DOI: 10.3390/buildings12122067.

DAQAQ, Mohammed F. et al. On the Role of Nonlinearities in Vibratory Energy Harvesting: A Critical Review and Discussion. **Applied Mechanics Reviews**, ASME International, v. 66, n. 4, May 2014. ISSN 2379-0407. DOI: 10.1115/1.4026278.

DE MARQUI, Carlos et al. Modeling and Analysis of Piezoelectric Energy Harvesting From Aeroelastic Vibrations Using the Doublet-Lattice Method. **Journal of Vibration and Acoustics**, ASME International, v. 133, n. 1, Dec. 2010. ISSN 1528-8927. DOI: 10.1115/1.4002785.

DEB, K. et al. A fast and elitist multiobjective genetic algorithm: NSGA-II. **IEEE Transactions on Evolutionary Computation**, Institute of Electrical and Electronics Engineers (IEEE), v. 6, n. 2, p. 182–197, Apr. 2002. ISSN 1089-778X. DOI: 10.1109/4235.996017.

DOWLING, Norman. **Mechanical behavior of materials: engineering methods for deformation, fracture, and fatigue**. Upper Saddle River, N.J: Pearson/Prentice Hall, 2007. ISBN 0131863126.

DREZET, C.; KACEM, N.; BOUHADDI, N. Design of a nonlinear energy harvester based on high static low dynamic stiffness for low frequency random vibrations. **Sensors and Actuators A: Physical**, Elsevier BV, v. 283, p. 54–64, Nov. 2018. ISSN 0924-4247. DOI: 10.1016/j.sna.2018.09.046.

EFUNDA. **Piezo material data**. [S.l.: s.n.], 2021. http://www.efunda.com/materials/piezo/material_data/matdata_index.cfm. Acessed 10 jun 2021.

ENDO, T. et al. Damage evaluation of metals for random or varying loading - three aspects of rain flow method. In: 371–380. v. 1-2.

ERTURK. **Piezoelectric Energy Harvestin**. [S.l.]: John Wiley & Sons, Apr. 2011. 414 pp. ISBN 047068254X. Available from: <https://www.ebook.de/de/product/14803912/erturk_piezoelectric_energy_harvestin.html>.

ESCHENAUER, Hans; OSYCZKA, Andrzej. **Multicriteria design optimization**: procedures and applications. [S.l.]: Springer-Verlag, 1990. P. 482. ISBN 0387506047.

FARIA, A. W. Modelagem por elementos finitos de placas compostas dotadas de sensores e atuadores piezoelétricos: implementação computacional e avaliação numérica. In.

FLEMING, A. J.; BEHRENS, S.; MOHEIMANI, S. O. Reza. Optimization and implementation of multimode piezoelectric shunt damping systems. **IEEE/ASME Transactions on Mechatronics**, Institute of Electrical and Electronics Engineers (IEEE), v. 7, n. 1, p. 87–94, 2002. DOI: 10.1109/3516.990891.

FLORIAN, Aleš. An efficient sampling scheme: Updated Latin Hypercube Sampling. **Probabilistic Engineering Mechanics**, Elsevier BV, v. 7, n. 2, p. 123–130, 1992. DOI: 10.1016/0266-8920(92)90015-a.

GERGES, Y. Méthodes de réduction de modèles en vibroacoustique non-linéaire. In.

GRIPP, J.A.B.; RADE, D.A. Vibration and noise control using shunted piezoelectric transducers: A review. **Mechanical Systems and Signal Processing**, Elsevier BV, v. 112, p. 359–383, Nov. 2018. ISSN 0888-3270. DOI: 10.1016/j.ymssp.2018.04.041.

GUZMÁN, Daniel Giraldo; SILVA, Emilio C N; RUBIO, Wilfredo Montealegre. Topology optimization of piezoelectric sensor and actuator layers for active vibration control. **Smart Materials and Structures**, IOP Publishing, v. 29, n. 8, p. 085009, June 2020. ISSN 1361-665X. DOI: 10.1088/1361-665x/ab9061.

HAGOOD, N. W.; FLOTOW, A. von. Damping of structural vibrations with piezoelectric materials and passive electrical networks. **Journal of Sound and Vibration**, Elsevier BV, v. 146, n. 2, p. 243–268, 1991. DOI: 10.1016/0022-460x(91)90762-9.

HOMAYOUNI-AMLASHI, Abbas et al. 2D topology optimization MATLAB codes for piezoelectric actuators and energy harvesters. **Structural and Multidisciplinary Optimization**, Springer Science and Business Media LLC, v. 63, n. 2, p. 983–1014, Oct. 2020. ISSN 1615-1488. DOI: 10.1007/s00158-020-02726-w.

KANG, Zhan; WANG, Xiaoming. Topology optimization of bending actuators with multilayer piezoelectric material. **Smart Materials and Structures**, IOP

Publishing, v. 19, n. 7, p. 075018, June 2010. ISSN 1361-665X. DOI: 10.1088/0964-1726/19/7/075018.

KANG, Zhan; WANG, Xiaoming; LUO, Zhen. Topology Optimization for Static Shape Control of Piezoelectric Plates With Penalization on Intermediate Actuation Voltage. **Journal of Mechanical Design**, ASME International, v. 134, n. 5, Apr. 2012. ISSN 1528-9001. DOI: 10.1115/1.4006527.

KÖBIS, Elisabeth. On Robust Optimization: Relations Between Scalar Robust Optimization and Unconstrained Multicriteria Optimization. **Journal of Optimization Theory and Applications**, Springer Science and Business Media LLC, v. 167, n. 3, p. 969–984, Sept. 2013. ISSN 1573-2878. DOI: 10.1007/s10957-013-0421-6.

KÖGL, Martin; SILVA, Emílio C N. Topology optimization of smart structures: design of piezoelectric plate and shell actuators. **Smart Materials and Structures**, IOP Publishing, v. 14, n. 2, p. 387–399, Mar. 2005. ISSN 1361-665X. DOI: 10.1088/0964-1726/14/2/013.

LAMBERT, S.; KHALIJ, Leila; PAGNACCO, E. **Contribution à l'analyse de l'endommagement par fatigue et au dimensionnement de structures soumises à des vibrations aléatoires**. Dec. 2007. PhD thesis.

LAMBERT, S.; PAGNACCO, E.; KHALIJ, L. A probabilistic model for the fatigue reliability of structures under random loadings with phase shift effects. **International Journal of Fatigue**, Elsevier BV, v. 32, n. 2, p. 463–474, 2010. DOI: 10.1016/j.ijfatigue.2009.09.007.

LESIEUTRE, G. A. Vibration Damping and Control Using Shunted Piezoelectric Materials. **The Shock and Vibration Digest**, SAGE Publications, v. 30, n. 3, p. 187–195, May 1998. ISSN 0583-1024. DOI: 10.1177/058310249803000301.

LI, Bin; FREITAS, Manuel de. A Procedure for Fast Evaluation of High-Cycle Fatigue Under Multiaxial Random Loading. **Journal of Mechanical Design**, ASME International, v. 124, n. 3, p. 558–563, 2002. DOI: 10.1115/1.1485291.

LI, Daochun et al. Energy harvesting by means of flow-induced vibrations on aerospace vehicles. **Progress in Aerospace Sciences**, Elsevier BV, v. 86, p. 28–62, Oct. 2016. ISSN 0376-0421. DOI: 10.1016/j.paerosci.2016.08.001.

LIMA, Antônio Marcos Gonçalves de. **Modélisation et Optimisation robuste de systèmes mécaniques en présence d amortissement viscoélastique**. June 2007. PhD thesis – Universidade Federal de Uberlândia, Uberlândia.

LIPSKI, Adam. Rapid determination of the Wöhler's curve for aluminum alloy 2024-T3 by means of the thermographic method. In: AIP Conference Proceedings. [S.l.]: Author(s), 2016. DOI: 10.1063/1.4965936.

MACIEL, Gabriel P. R.; BARBOSA, Roberto Spinola. TÉCNICAS PARA REDUÇÃO DA ORDEM DE SISTEMAS DINÂMICOS NA BASE MODAL. In: ANAIS do XXIII Simpósio Internacional de Engenharia Automotiva. [S.l.]: Editora Edgard Blücher, Sept. 2015. (SIMEA 2015). DOI: 10.5151/engpro-simea2015-pap189.

MAHMOUDI, S; KACEM, N; BOUHADDI, N. Enhancement of the performance of a hybrid nonlinear vibration energy harvester based on piezoelectric and electromagnetic transductions. **Smart Materials and Structures**, IOP Publishing, v. 23, n. 7, p. 075024, June 2014. ISSN 1361-665X. DOI: 10.1088/0964-1726/23/7/075024.

MARAKAKIS, Konstantinos et al. New Optimal Design of Multimode Shunt-Damping Circuits for Enhanced Vibration Control. **Signals**, MDPI AG, v. 3, n. 4, p. 830–856, Nov. 2022. ISSN 2624-6120. DOI: 10.3390/signals3040050.

MARCZYK, Jacek. Stochastic multidisciplinary improvement - Beyond optimization. In: 8TH Symposium on Multidisciplinary Analysis and Optimization. [S.l.]: American Institute of Aeronautics and Astronautics, Sept. 2000. DOI: 10.2514/6.2000-4929.

MILNE, I.; KARIHALOO, B. L. **Comprehensive Structural Integrity**: 10 - Volume set. [S.l.]: Elsevier Science, 2003. P. 7750. ISBN 9780080437491.

MOHAMMADI-AMIN, M.; GHADIRI, B. An Aeroelastic Metamodel Based on Experimental Data for Flutter Prediction of Swept Rectangular Wings. **Journal of Applied Fluid Mechanics**, Academic World Research, v. 6, n. 01, Jan. 2013. ISSN 1735-3645. DOI: 10.36884/jafm.6.01.19503.

MOHEIMANI, S. O. Reza; FLEMING, Andrew J. **Piezoelectric Transducers for Vibration Control and Damping**. [S.l.]: SPRINGER NATURE, June 2006. 271 pp. ISBN 1846283310. Available from: <https://www.ebook.de/de/product/5194633/s_o_reza_moheimani_andrew_j_fleming_piezoelectric_transducers_for_vibration_control_and_damping.html>.

MOREIRA, Fernando Ricardo. **Otimização robusta multiobjetivo para o projeto de sistemas em Engenharia**. 2015. PhD thesis – Universidade Federal de Uberlândia, Uberlândia.

MOTTA MELLO, Luis Augusto et al. Design of quasi-static piezoelectric plate based transducers by using topology optimization. **Smart Materials and Structures**, IOP Publishing, v. 23, n. 2, p. 025035, Jan. 2014. ISSN 1361-665X. DOI: 10.1088/0964-1726/23/2/025035.

NAKASONE, P.H.; SILVA, E.C.N. Dynamic Design of Piezoelectric Laminated Sensors and Actuators using Topology Optimization. **Journal of Intelligent Material Systems and Structures**, SAGE Publications, v. 21, n. 16, p. 1627–1652, Nov. 2010. ISSN 1530-8138. DOI: 10.1177/1045389x10386130.

NOH, Jin Yee; YOON, Gil Ho. Topology optimization of piezoelectric energy harvesting devices considering static and harmonic dynamic loads. **Advances in Engineering Software**, Elsevier BV, v. 53, p. 45–60, Nov. 2012. ISSN 0965-9978. DOI: 10.1016/j.advengsoft.2012.07.008.

PALMGREN, A. G. Die Lebensdauer von Kugellagern. **Zeitschrift des Vereines Deutscher Ingenieure**, v. 14, p. 339–341, 1924.

PETERSEN, Kai et al. Systematic Mapping Studies in Software Engineering. In: ELECTRONIC Workshops in Computing. [S.l.]: BCS Learning & Development, June 2008. DOI: 10.14236/ewic/ease2008.8.

PREUMONT, A. On the peak factor of stationary Gaussian processes. **Journal of Sound and Vibration**, Elsevier BV, v. 100, n. 1, p. 15–34, 1985. DOI: 10.1016/0022-460x(85)90339-6.

RAZE, Ghislain et al. Multimodal vibration damping using a simplified current blocking shunt circuit. **Journal of Intelligent Material Systems and Structures**, SAGE Publications, v. 31, n. 14, p. 1731–1747, June 2020. ISSN 1530-8138. DOI: 10.1177/1045389x20930103.

REDDY, J. N. **Mechanics of laminated composite plates: theory and analysis**. Boca Raton: CRC Press, 1997. ISBN 0849331013.

_____. **Theory and Analysis of Elastic Plates and Shells**. [S.l.]: CRC, 2006. P. 568. ISBN 9780849384158.

RIBEIRO, Lorrane Pereira; LIMA, Antônio Marcos Gonçalves de. Projeto ótimo de circuitos shunt para o controle de vibrações de estruturas compostas. In: ANAIS do Congresso Nacional de Matemática Aplicada à Indústria. [S.l.]: Editora Edgard Blücher, 2015. DOI: 10.5151/mathpro-cnmai-0056.

ROSA, Ulisses Lima; LIMA, Antônio Marcos Gonçalves de. Fatigue analysis of dynamic systems subjected to cyclic loading in the frequency domain. In: PROCEEDINGS of the 23rd ABCM International Congress of Mechanical Engineering. [S.l.]: ABCM Brazilian Society of Mechanical Sciences and Engineering, 2015. DOI: 10.20906/cps/cob-2015-1620.

RUBINSTEIN, Reuven. **Simulation and the monte carlo method**. New York: Wiley, 1981. ISBN 0471089176.

SAJEDI, Seyed Omid; LIANG, Xiao. Vibration-based semantic damage segmentation for large-scale structural health monitoring. **Computer-Aided Civil and Infrastructure Engineering**, Wiley, v. 35, n. 6, p. 579–596, Dec. 2019. ISSN 1467-8667. DOI: 10.1111/mice.12523.

SANTANA, Danuza Cristina. **Modelagem numérica e otimização de shunts piezelétricos aplicados ao controle passivo de vibrações**. 2007. PhD thesis – Universidade Federal de Uberlândia, Uberlândia.

SARAVANOS, D. A.; HEYLIGER, P. R. Coupled Layerwise Analysis of Composite Beams with Embedded Piezoelectric Sensors and Actuators. **Journal of Intelligent Material Systems and Structures**, SAGE Publications, v. 6, n. 3, p. 350–363, 1995. DOI: 10.1177/1045389x9500600306.

SCHOEFTNER, Juergen; BUCHBERGER, Gerda. A contribution on the optimal design of a vibrating cantilever in a power harvesting application – Optimization of piezoelectric layer distributions in combination with advanced harvesting circuits. **Engineering Structures**, Elsevier BV, v. 53, p. 92–101, Aug. 2013. ISSN 0141-0296. DOI: 10.1016/j.engstruct.2013.03.022.

SENA, João Pedro et al. ATUALIZAÇÃO DE MODELOS NUMÉRICOS A PARTIR DE DADOS EXPERIMENTAIS PARA MONITORAMENTO ESTRUTURAL: MAPEAMENTO SISTEMÁTICO. **REEC - Revista Eletrônica de Engenharia Civil**, Universidade Federal de Goias, v. 18, n. 2, p. 60–71, Dec. 2022. ISSN 2179-0612. DOI: 10.5216/reec.v18i2.63758.

SHANNON, C. E. A Mathematical Theory of Communication. **Bell System Technical Journal**, Institute of Electrical and Electronics Engineers (IEEE), v. 27, n. 3, p. 379–423, July 1948. ISSN 0005-8580. DOI: 10.1002/j.1538-7305.1948.tb01338.x.

SILVA, Emílio Carlos Nelli; KIKUCHI, Noboru. Design of piezoelectric transducers using topology optimization. **Smart Materials and Structures**, IOP Publishing, v. 8, n. 3, p. 350–364, Jan. 1999. ISSN 1361-665X. DOI: 10.1088/0964-1726/8/3/307.

SILVA, Victor Costa da. Concepção robusta de circuitos elétricos Shunt multimodais para o controle passivo de vibrações de estruturas compostas. In.

SIMON, Dan. **Evolutionary Optimization Algorithms**. [S.l.]: Wiley & Sons, Incorporated, John, 2013. P. 772. ISBN 9780470937419.

SINES, G. Behavior of metals under complex static and alternating stresses. **Metal fatigue**, McGraw-Hill, New York, v. 1, p. 145–169, 1959.

SOIZE, Christian. **Stochastic Models of Uncertainties in Computational Mechanics**. [S.l.]: American Society of Civil Engineers, Nov. 2012. ISBN 9780784476864. DOI: 10.1061/9780784412237.

SRINIVAS, N.; DEB, Kalyanmoy. Muiltiobjective Optimization Using Nondominated Sorting in Genetic Algorithms. **Evolutionary Computation**, MIT Press - Journals, v. 2, n. 3, p. 221–248, Sept. 1994. ISSN 1530-9304. DOI: 10.1162/evco.1994.2.3.221.

VANDERPLAATS, Garret N. **Numerical Optimization Techniques for Engineering Design: With Applications (MCGRAW HILL SERIES IN MECHANICAL ENGINEERING)**. [S.l.]: McGraw-Hill College, 1984. P. 333. ISBN 9780070669642.

VERMA, Shanu; PANT, Millie; SNASEL, Vaclav. A Comprehensive Review on NSGA-II for Multi-Objective Combinatorial Optimization Problems. **IEEE Access**, Institute of Electrical and Electronics Engineers (IEEE), v. 9, p. 57757–57791, 2021. ISSN 2169-3536. DOI: 10.1109/access.2021.3070634.

VIANA, Felipe Antonio C.; VALDER STEFFEN, Jr. Multimodal vibration damping through piezoelectric patches and optimal resonant shunt circuits. **J. of the Braz. Soc. of Mech. Sci. and Eng.**, Springer Science and Business Media LLC, v. 28, n. 3, p. 293–310, 2006. DOI: 10.1590/s1678-58782006000300007.

WANG, S Y; TAI, K; QUEK, S T. Topology optimization of piezoelectric sensors/actuators for torsional vibration control of composite plates. **Smart Materials and Structures**, IOP Publishing, v. 15, n. 2, p. 253–269, Jan. 2006. ISSN 1361-665X. DOI: 10.1088/0964-1726/15/2/004.

WEBER, Bastien. Fatigue multiaxiale des structures industrielles sous chargement quelconque, Jan. 1999.

WU, Shu yau. Method for multiple-mode shunt damping of structural vibration using a single PZT transducer. In_____. **Smart Structures and Materials 1998: Passive Damping and Isolation**. [S.l.]: SPIE, 1998. DOI: 10.1117/12.310680.

WYSOCKI, Timo von et al. Generating Component Designs for an Improved NVH Performance by Using an Artificial Neural Network as an Optimization Metamodel. **Designs**, MDPI AG, v. 5, n. 2, p. 36, June 2021. ISSN 2411-9660. DOI: 10.3390/designs5020036.

ZAMBOLINI-VICENTE, Bruno Gabriel Gustavo Leonardo. **Projeto robusto de Circuitos Shunt para o controle passivo de vibrações de estruturas compostas**. 2000. MA thesis – Universidade Federal de Uberlândia, Uberlândia.

ZHANG, Bin et al. Analysis and optimization of self-powered parallel synchronized switch harvesting on inductor circuit for piezoelectric energy harvesting. **Smart Materials and Structures**, IOP Publishing, v. 31, n. 9, p. 095040, Aug. 2022. ISSN 1361-665X. DOI: 10.1088/1361-665x/ac83fe.

ZHANG, Xiaopeng; KANG, Zhan. Topology optimization of piezoelectric layers in plates with active vibration control. **Journal of Intelligent Material Systems and Structures**, SAGE Publications, v. 25, n. 6, p. 697–712, Aug. 2013. ISSN 1530-8138. DOI: 10.1177/1045389x13500577.

_____. Dynamic topology optimization of piezoelectric structures with active control for reducing transient response. **Computer Methods in Applied Mechanics and Engineering**, Elsevier BV, v. 281, p. 200–219, Nov. 2014. ISSN 0045-7825. DOI: 10.1016/j.cma.2014.08.011.

ZHANG, Xiaopeng; KANG, Zhan; LI, Ming. Topology optimization of electrode coverage of piezoelectric thin-walled structures with CGVF control for minimizing sound radiation. **Structural and Multidisciplinary Optimization**, Springer Science and Business Media LLC, v. 50, n. 5, p. 799–814, May 2014. ISSN 1615-1488. DOI: 10.1007/s00158-014-1082-2.

ZHAO, Jianhua et al. Damage localization based on modal strain energy index and evidence theory. Ed. by W. Qin, L. Wang and V. Yepes. **E3S Web of Conferences**, EDP Sciences, v. 165, p. 06053, 2020. ISSN 2267-1242. DOI: 10.1051/e3sconf/202016506053.

ZHENG, Bin; CHANG, Ching-Jui; GEA, Hae Chang. Topology optimization of energy harvesting devices using piezoelectric materials. en. **Struct. Multidiscip.**

Optim., Springer Science and Business Media LLC, v. 38, n. 1, p. 17–23, Mar. 2009.